NATIONAL TECHNICAL UNIVERSITY OF ATHENS
SCHOOL OF NAVAL ARCHITECTURE AND MARINE ENGINEERING
DIVISION OF SHIP AND MARINE HYDRODYNAMICS

A Boundary Element Method for the hydrodynamic analysis of floating bodies in variable bathymetry regions

---

Diploma Thesis

November 2017

Author : Leonidas Thermos

Supervisor : K. A. Belibassakis, Professor, NTUA

Committee : G. K. Politis, Professor, NTUA

G. A. Athanassoulis, Professor, NTUA

Acknowledgements

The present Diploma Thesis is completing a five-year period of studies and research at the School of Naval Architecture and Marine Engineering of National Technical University of Athens. So, it is a chance to express my sincere gratitude to a number of people whose contribution where valuable for the accomplishment of this work and of my studies and to make a valuation of the years that passed.

First of all, I would like to thank my supervisor Professor K. Belibassakis for his continuous guidance and support during the preparation of this thesis. His deep and wide knowledge in the field of marine hydrodynamics provided me with the required background to overcome the difficulties encountered during this study. Most of all his continuous presence and his intention to help, were a very important piece to finish my work.

Also, I am very grateful to Mr Yiannis Georgiou for the support during the course of Ship Dynamics, his very useful advice and his helpful contribution.

Last but not least, I would like to thank my parents for their understanding and financial support, making my work easier, my friends for their understanding and most of all my brother John, for his continuous support and his guidance, that without it, it would be very difficult to finish my studies. This thesis is completing a part of my life, that except from the knowledge i gained, it helped me to observe an other part of the society, as it is a school. Education in the School of Naval Architecture & Marine Engineering of NTUA and interaction with people, guided me in times of wilderness, strengthened my personality and gave me an other perspective for the world.

Contents

Abstract

Floating structures, operating in a nearshore coastal environment of variable bathymetry, and their hydrodynamic behavior constitute an important subject in marine and offshore structure design and performance. The study of wave energy converters, exploiting the wave energy potential and converting it into electrical energy, is of particular interest in ocean and coastal engineering. In the present thesis a Boundary Element Method is presented and discussed, for treating problems concerning waves-floating body-seabed interactions in a variable bathymetry environment and arbitrary body geometry. As a result the hydrodynamic behavior of the body is calculated. Specifically, in Chapter 1 a state-of-the-art review concerning offshore and coastal floating structures and wave energy converters of the kind of point absorbers is presented. Also, a brief review of the boundary element method is given. In Chapter 2, an absorbing layer technique, in conjunction with a boundary element method is presented, and optimized in the case of two-dimensional wavemaker problem, for which an analytical solution is available (both for the flap-type and the piston-type wavemakers). Comparing the numerical against the analytical solution useful conclusions are derived for the optimum selection of absorbing layer parameters. A similar procedure is followed in Chapter 3, where a 3D hybrid boundary element - absorbing layer method is presented, treating the problem of a floating cylinder, oscillating in finite depth. The method is based on 4-node quadrilateral elements and piecewise constant dipole distribution, and details concerning the integration formulae are provided in Appendix A. Again, in the case of vertical cylinder the analytic solution is used to validate the numerical method in constant depth. Then, in Chapter 4, the latter method is extended to the hydrodynamic analysis of floating body in variable bathymetry. The present 3D hybrid boundary element - absorbing layer method is used for the solution of the radiation problems (for all 6 dofs) and the diffraction problem, which is formulated using the solution concerning the propagating wave over the variable bathymetry. The latter is obtained by application of the coupled-mode model by Athanassoulis & Belibassakis (1999), which is presented in Appendix B. The present thesis ends with conclusions and suggestions for future work.

Περίληψη

Οι πλωτές κατασκευές, που λειτουργούν σε ένα θαλάσσιο περιβάλλον με μεταβλητή βαθυμετρία, και η υδροδυναμική συμπεριφορά τους αποτελούν ένα σημαντικό θέμα στον θαλάσσιο και υπεράκτιο σχεδιασμό. Η μελέτη των μετατροπέων κυματικής ενέργειας, που αξιοποιούν την κυματική ενέργεια και την μετατρέπουν σε ηλεκτρική, παρουσιάζει ιδιαίτερο ενδιαφέρον για την ωκεάνια και παράκτια μηχανική. Στην παρούσα διπλωματική εργασία, παρουσιάζεται και σχολιάζεται μία μέθοδος συνοριακών στοιχείων, για την αντιμετώπιση προβλημάτων που σχετίζονται με την αλληλεπίδραση των κυμάτων, του πλωτού σώματος και του πυθμένα σε περιβάλλον με γενική βαθυμετρία για οποιαδήποτε γεωμετρία σώματος. Σαν αποτέλεσμα υπολογίζεται η υδροδυναμική συμπεριφορά του σώματος. Συγκεκριμένα, στο πρώτο κεφάλαιο παρουσιάζεται μία περιγραφή σχετικά με τις παράκτιες και τις υπεράκτιες πλωτές κατασκευές και με τους μετατροπείς κυματικής ενέργειας του τύπου σημειακής απορρόφησης. Επίσης, δίνεται μία σύντομη ανασκόπηση της μεθόδου συνοριακών στοιχείων. Στο κεφάλαιο 2, μία τεχνική στρώματος απορρόφησης, σε συνδυασμό με την μέθοδο συνοριακών στοιχείων παρουσιάζεται και βελτιστοποιείται στην περίπτωση του δισδιάστατου προβλήματος κυματιστήρα, για το οποίο υπάρχει αναλυτική λύση(και για τύπου flap και για τον τύπου piston κυματιστήρα). Συγκρίνοντας την αριθμητική με την αναλυτική λύση παράγονται χρήσιμα συμπεράσματα για τον βέλτιστο συνδυασμό παραμέτρων του στρώματος απορρόφησης. Μία παρόμοια διαδικασία ακολουθείται στο κεφάλαιο 3, όπου παρουσιάζεται μία τρισδιάστατη υβριδική μέθοδος συνοριακών στοιχείων με στρώμα απορρόφησης, αντιμετωπίζοντας το πρόβλημα πλωτού κυλίνδρου, ταλαντευόμενου σε σταθερό βάθος. Η μέθοδος βασίζεται σε τετράκομβα στρεβλά στοιχεία και σε σταθερή ανά στοιχείο κατανομή διπόλων, και λεπτομέρειες σχετικά με την φόρμουλα ολοκλήρωσης παρέχονται στο παράρτημα Α. Ξανά, στην περίπτωση κατακόρυφου κυλίνδρου, η αναλυτική λύση χρησιμοποιείται για να πιστοποιήσουμε την αριθμητική μέθοδο σε σταθερό βάθος. Έπειτα, στο κεφάλαιο 4, η τελευταία μέθοδος επεκτείνεται στην υδροδυναμική ανάλυση πλωτού σώματος με γενική βαθυμετρία. Η παρούσα τρισδιάστατη υβριδική μέθοδος συνοριακών στοιχείων με στρώμα απορρόφησης χρησιμοποιείται για την επίλυση των προβλημάτων ακτινοβολίας και για το πρόβλημα περίθλασης, το οποίο μοντελοποιείται χρησιμοποιώντας την λύση σχετικά με τον προσπίπτοντα κυματισμό σε γενική βαθυμετρία. Η τελευταία λαμβάνεται με εφαρμογή της μεθόδου συζευγμένων μορφών από Αθανασούλης και Μπελιμπασάκης (1999), η οποία παρουσιάζεται στο παράρτημα Β. Η παρούσα εργασία κλείνει με συμπεράσματα και προτάσεις για μελλοντική έρευνα.

Chapter 1
INTRODUCTION

In the present introductory chapter, we begin with a brief review, concerning research on offshore and coastal structures, focusing especially on wave energy converters of the type of point absorbers operating in variable bathymetry regions and the boundary element method. Concerning the wave energy converters, these systems, as we have been ideally suited for converting directly environmental (sea wave) energy to useful electrical energy via one generator. In the second part of this chapter we will present a brief historic review about the boundary element method, which is the basic method for solving the variable bathymetry problem in our thesis.

1.1 Floating structures

We will present a brief review concerning the types of the floating structures, beginning with the large-scale floating structures and closing with coastal wave energy devices. Firstly, we refer to large-scale floating structures and then to other water-exploiting devices.

1.1.1 Types of Floating Structures

Large-scale floating structures are broadly classified as either pontoons or semisubmersibles. Pontoons are essentially floating slabs that are characterised by their low depth-to-width ratios and are usually deployed in a benign sea state condition such as in waters adjacent to the coast, inside a cove or a lagoon, or where breakwaters and other protective installations can be constructed to protect the structure from large waves and swells. In order to restrain lateral movements, they may be anchored to the sea bed through the use of mooring lines comprising chains, ropes, sinkers, anchors or tethers. Where greater restraint is necessary, the pier/quay wall method or the dolphin-frame guide mooring system may be adopted. Pontoons are generally cost effective with low manufacturing costs and are relatively easy to repair and maintain. The main components of a pontoon are the floating body, the mooring facility, the access bridge/gangway/ linkway or floating road and the breakwater. Semi-submersibles have a

structural form that is thicker than their pontoon counterparts and have been deployed in deep sea environments since as early as the 1970s. They are partly raised above the sea level using column tubes or watertight ballast structural compartments at the base to compensate for the effects of larger wave-lengths and -heights. Floating oil drilling platforms and semisubmersible type floating wind farms are typical examples of this category of floating structures. While semi-submersibles are often towed, some models are hybrids between a pure static floating structure and a marine vessel with their own propulsion system for short-range transport. When deployed to the required location, these floating structures are then attached to the seabed using mooring cables or tethers.

1.1.2 Floating Offshore Wind Turbine

A floating wind turbine (Fig.1.1) is mounted on a floating structure that supports the pilar and the turbine to generate electricity in deep water or depths where bottom-mounted towers are not feasible. Locating wind farms out at sea can reduce visual pollution while providing better accommodation for fishing and shipping lanes. In addition, the wind is typically more consistent and stronger over the sea, due to the absence of topographic features that disrupt wind flow. More details can be found in Feasibility of Floating Platform Systems for Wind Turbines (Musial et al 2003).

1.1.3 Floating Oil Storage Base

The large floating oil reservoirs (Fig.1.2) must continue to be safely moored to dolphins in the extreme wind and wave conditions at the site and remain safe and serviceable during earthquakes. Given that the construction of a floating oil storage base has been based on a completely new technology to moor huge oil reservoirs to dolphins by rubber fenders, the Ministry of Transport, Japan had to develop a new Design Standard for the Floating Oil Storage Base. The standard covers the construction, maintenance, repair and improvement of a floating oil storage facility comprising floating oil reservoirs, working dolphins, mooring dolphins, deepwater terminals, oil fences and ancillary facilities. A special design code was also developed for floating oil reservoirs that are moored to dolphins by the use of high performance large rubber fenders. Although this kind of rubber fender is commonly used at mooring dolphins of deep water terminals, it was the first attempt to use the material for permanent mooring even in extreme natural conditions. Several characteristics of rubber fenders shall be examined herein.

Figure 1.1: Floating Offshore Wind Turbine (http://www.sunwindenergy.com)

Figure 1.2: Floating oil storage base. (http://eng.mortemor.com)

1.1.4 Large Marine Concrete Structures.

The Mega-Float project is a pontoon-type Very Large Floating Structure that was designed for deployment in protected waters such as in a large bay. It consists of a floating structure, a mooring system, and access infrastructure. While construction of a breakwater was contemplated, the existing breakwater around the site was found to be sufficient. Unlike conventional ships where the response is dominated by rigid-body motions, the response of the

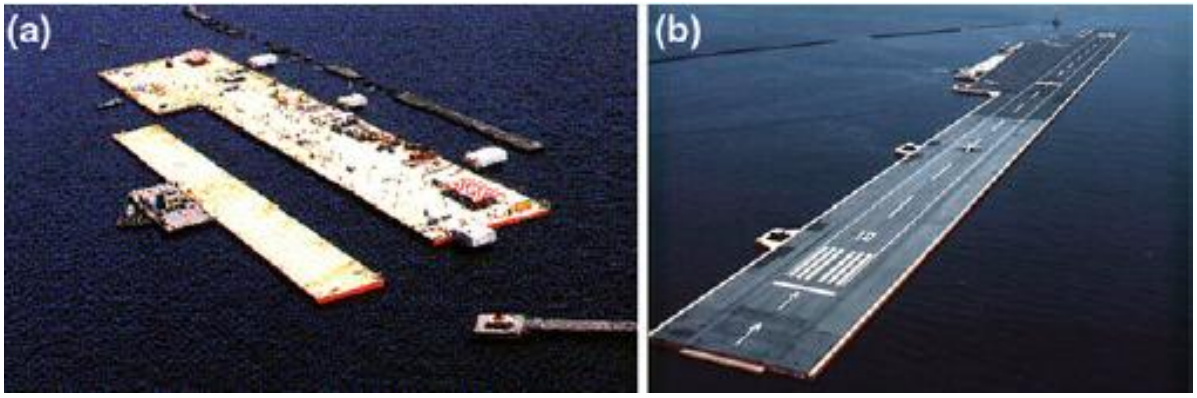

Figure 1.3: Mega-float experimental models. A) Phase I model. B) Phase II model (http://oplat-usa.com)

Mega-Float is dominated by hydroelastic responses because of its thin mat-like configuration. Mega-Float is a pontoon-type VLFS which is cost-effective, competitive and suitable for development in protected waters such as in a large bay. It consists of a floating structure, a mooring system and access infrastructure. If necessary, breakwater construction is considered. The Mega-Float research project was performed in two phases (Isobe 1999). In Phase I (1995–1997), the fundamental design(Fig.1.3(a)), construction and operational technologies were developed, while in Phase II (1998–2001), a corroborative study on the use of the Mega-Float (Fig.1.3(b)) as an airport was performed. VLFSs are so large in the horizontal plane that dynamical elastic deformations are dominant as compared to rigid motions under wave action. Interactions between hydrodynamic pressure and elastic deformation are therefore essential for their dynamic responses of VLFSs. Many kinds of numerical methods have been developed to perform the hydroelastic analysis of pontoon-type VLFSs. Takeoffs and landings of small aircrafts were successfully demonstrated in the Phase II experiment.

1.1.5 Others

1.1.5.1 Oscillatory Water Column (OWC)

An Oscillating Water Column is a steel or concrete structure with a chamber presenting at least two openings, one in communication with the sea and the other with the atmosphere. Under the action of waves the free surface inside the chamber oscillates and displaces the air above the free surface. The air is thus forced to flow through a turbine. The turbine is usually a bi-directional ‘wells’ turbine, which makes use of airflow in both directions, on the compression and decompression of the air to extract the ocean power (ISSC (2006); EPRI (2005); AEA (2006); Al-Habaibeh (2009)). For an OWC an optimum power take-off 7 can be achieved if the wave periods are close to the natural period of the water column. Therefore the design must be tuned to the site-specific wave climate.

Figure 1.4: OWC: (a) the Limpet and (b) the Pico Power Plant (Sinha 2015).

These devices too as in the case of overtopping devices can be floating or fixed to the shore. Fixed structures are located on the shoreline or near shore, standing on the sea bottom (with foundations like gravity based structures or fixed to the rocky cliff) while floating structure are placed offshore with a partially submerged chamber with air trapped above a column of water (EPRI (2005)).

Shore line devices have the advantage of an easier installation and maintenance, and do not require deep-water moorings and long underwater electrical cables. However, less energetic wave climate at the shoreline is seen to be the main problem. Falcão (2010) suggested that this disadvantage can be partly compensated by natural wave energy concentration due to refraction and/or diffraction.

OWC is one of the wave energy devices which have been studied extensively. The Limpet OWC (Fig. 1.4 (a)) is one that is working on this technology. This is a grid-connected, shoreline-based OWC, with a rated power of 500 kW. The Limpet used a unique construction method, where construction of the concrete column structure occurred behind a rock wall, which was then removed using explosives. Unfortunately, several complications arose due to the presence of debris near and underneath the structure, and the overall performance of the device was found to be highly dependent on the shape and depth of the seafloor around the device. The OWC drives a pair of Wells turbines, and provides around 22 kW of power (annual average), peaking near 150 kW.

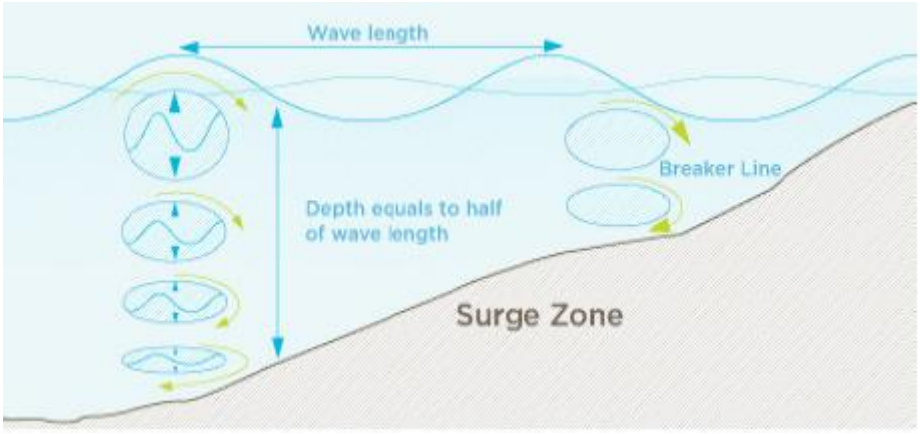

Figure 1.5: Water particle trajectories on a slopping beach (Sinha 2015).

Another WEC which is also classified as OWC is the Pico Power Plant. This is an OWC power plant rated at 400 kW, was installed on the shoreline of the island of Pico, in the Azores, Portugal. The plant (Fig. 1.4 (b)) uses a concrete structure, mounted on the seabed/shoreline, counting with Wells turbines used as power take-off. Built in 1995-1999, various problems caused to stop the operation of the device. Testing resumed again in 2005 and the plant was connected to the local power grid. Unfortunately, the presence of mechanical resonance in the structure prevented the plant from operating at optimum power levels, limiting 8 it to power production to 20-70 kW range. Other oscillating water columns are: The Wave Energy Conversion Actuator (WECA) the Osprey OWC, the Port Kembla, the Sakata OWC, the Mighty Whale, the Orecon MRC1000, the SPERBOY and the OE Buoy.

1.1.5.2 Oscillatory Wave Surge Converter (OWSC)

According to AEA (2006) an OWSC is also a wave surge/focusing device, but extracts the energy that exists in waves caused by the movement of water particles within them. This principle is then applied for water depths less than the half of the wave length, where the particle trajectory has large displacement on the longitudinal direction (see Fig. 1.5).

One example of this type of technology is the OYSTER. The Oyster is a wave energy converter that interacts efficiently with the dominant surge forces encountered in the near shore wave climate at depths of 10 to 15 m. The Oyster concept consists of a large buoyant bottom-hinged oscillator that completely penetrates the water column from the ocean surface to the seabed. The surging action of waves on the oscillator drives hydraulic pistons which pressurize fresh water causing it to be pumped to shore through high pressure pipelines. The onshore hydroelectric plant converts the hydraulic pressure into electrical power via a Pelton wheel,

which runs an electrical generator. The low pressure return-water passes back to the device in a closed loop via a second pipeline. Another device which operates as an OWSC is the WaveRoller.

1.1.5.3 Pressure Differential

This is a submerged device typically located nearshore and attached to the seabed. The motion of the waves causes the sea level to rise and fall above the device therefore, inducing a pressure differential in the device. The alternating pressure can then pump fluid through a system to generate useful energy (AEA (2006)).

One example of this technology is the CETO. The CETO units are fully submerged and permanently anchored to the sea floor meaning that there is no visual impact as the units are out of sight. This also assists in making them safe from the extreme forces that can be present during storms. They are self-tuning to tide, sea state and wave pattern, making them able to perform in a wide variety of wave heights and in any direction. CETO units are manufactured from steel, rubber and hypalon materials, all proven for over 20 years in a marine-environment (Carnegie (2010)). Another device operating by the same principle is the WaveMaster (Powertech Labs Inc. (2009)).

There are different kinds of WECs which cannot fit in the previous classifications of WECs. The anaconda is one of these devices. This is all-rubber WEC which operates in a completely new way. When the anaconda is operating, the wave squeezes the tube (at the bow) and starts a bulge running. But as it runs the wave runs after it, squeezing more and more, so the bulge gets bigger and bigger. The bulge runs in front of the wave where the slope of the water (pressure gradient) is highest. In effect the bulge is surfing on the front of the wave concentrating the wave power over a wide frontage, at the end of the tube, which can be used to drive a turbine to generate electricity (Anaconda (2010)). Other WECs are: the BioWave (BioWave (2010)), The Netherlands, WaveRotor (EcoFyes (2010)) and the TETRON (Carbon trust (2010)).

1.2 Wave energy converters

Renewable energy such as: solar and wind energy have been extensively studied during the last few years. However, one energy source which has remained relatively untapped to date is ocean wave energy. Ocean wave energy has several advantages over other forms of renewable energy since waves are more constant, more predictable and have higher energy densities enabling devices to extract more power from smaller volumes at reduced costs and lower visual

impact (Brekken (2009)). Wave energy converters are devices as these that referred above, exploiting wave energy to generate electrical energy, operating in nearshore and coastal areas. WECs are studied below and many evidences about their classification are quoted.

1.2.1 Classification According to Distance from Shoreline

A classification according to distance from shoreline can be established as: shoreline, near shore and offshore WECs according to CRES (2006). Shoreline WECs are fixed or embedded to the shoreline, having the advantage of easier installation and maintenance. In addition, shoreline devices do not require deep-water moorings or long lengths of underwater electrical

cable. However, they would experience a much less powerful wave regime. Furthermore, the deployment of such schemes could be limited by the requirements for shoreline geology, tidal range, preservation of coastal scenery etc. The most advanced class of shoreline devices is the oscillating water column. Versions of these devices are: the Limpet, the European Pilot Plant on the island of Pico in the Azores and the Wavegen.

Near shore WECs are deployed at moderate water depths around 20- 30 m, at distances up to around 500 m from the shore. They have nearly the same advantages as shoreline devices and at the same time are exposed to higher wave power levels (CRES (2006)). The example of near shore wave energy device is WaveRoller (WaveRoller (2010)).

Another type is offshore WECs, which exploits more powerful wave regimes available in deep water with water depths deeper than 40 m before energy dissipation mechanisms have had a significant effect (CRES (2006)). In order to extract the maximum amount of energy from the waves, the devices need to be at or near the surface (i.e. floating), so they usually require flexible moorings and electrical transmission cables.

Early overseas designs to harness ocean wave energy concentrated on small, modular devices, yielding high power output when deployed in arrays. In comparison to the previous multi-megawatt designs, these small size devices were rated at a few tens of kilowatts each. More recent designs for offshore devices have also concentrated on small, modular devices. Some of the most promising ones are: the McCabe Wave Pump (CRES 2006) and the Pelamis.

1.2.2 Classification According to Type of Technology

Wave energy technology is rapidly growing and varies widely in application of conversion devices. Energy conversion devices can be divided in six principal groups: attenuators,

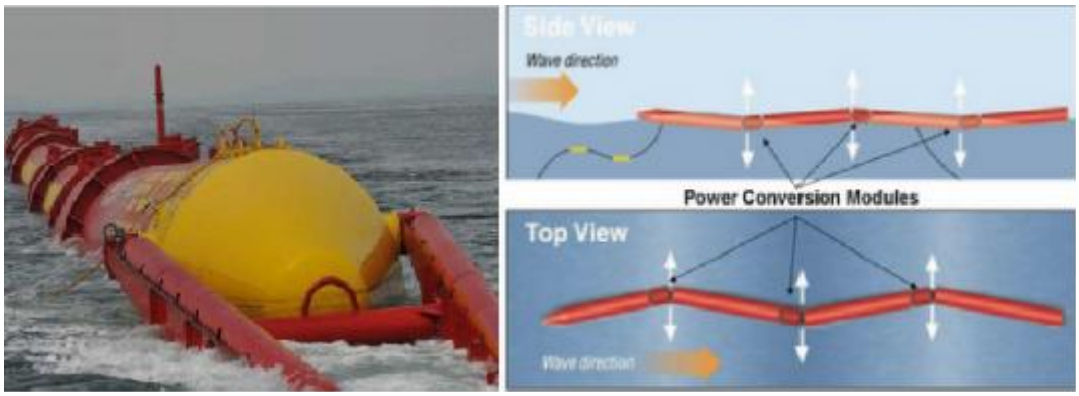

Figure 1.6: Attenuator-the Pelamis (Sinha 2015).

Figure 1.7: Overtopping: the Wave Dragon (Kofoed et al. 2006).

overtopping, oscillating water column (OWC), oscillating wave surge converters (OWSC), point absorbers and pressure differential devices. An Ocean wave energy converter which is a line absorber is called an attenuator if it is aligned parallel to the prevailing direction of wave propagation, which effectively rides the waves (Falnes (2007) and FEMP (2009)). When the attenuator rides the waves, differing heights of waves along the length of the device causes flexing where the segments connect. This flexing in the segments of the device produces forces and moments which are captured in the form of hydraulic pressure, which in turn is converted into energy. An advantage of the attenuator is that it has less area perpendicular to the waves, and hence it experiences lower forces (AEA (2006)).

One of the most known attenuator is the Pelamis. The Pelamis (Fig. 1.6) is a long and narrow (snakelike) semi-submerged structure which points into the waves. The Pelamis is composed of long cylindrical pontoons connected by three hinged joints. This device can exploit relative yaw and pitch motions between sections to capture ocean energy (Ringwood (2008)). Those motions are used to pressurize a hydraulic piston arrangement and then turn into a hydraulic turbine/generator to produce electricity (EPRI (2005); Al Habaibeh et al. (2009)). Other

examples of WECs which are classified as attenuators can also be found in the literature, like the McCabe wave pump, the Ocean Wave Treader and the Wave Treader (GreenOceanEnergy (2010)) and the Waveberg (Waveberg (2010)).

1.2.3 Overtopping

Another option to convert wave energy is by capturing the water that is close to the wave crest. To achieve this principle, the overtopping devices are designed with long arms and a wall placed between them. Large arms channel the waves focusing them at the centre wall over which waves topple into a storage reservoir, which is at a level higher than the average free-surface level of the surrounding sea. The reservoir creates a head of water and this potential energy is converted into electric energy by a conventional low-head hydraulic water turbine. Amongst many different types of water turbines, the lowhead "Kaplan" turbine is the most common choice.

The advantage of the overtopping principle is that turbine technology has already been in use in the hydropower industry for long time and is well understood (Powertech (2009)). However, the disadvantage is the strong non-linear hydrodynamics of overtopping devices and therefore the hydrodynamic problem of the overtopping principle cannot be addressed by linear water wave theory (Falcão (2010)).

One of the novel technologies using this principle is the Wave Dragon . The Wave Dragon is an offshore converter developed in Denmark, whose slack moored floating structure consists of two wave reflectors focusing the incoming waves towards a doubly curved ramp, a set of low-head hydraulic turbines (multiple modified Kaplan-Turbines) and a raised reservoir (Kofoed et al. (2006)). The low head hydraulic turbines convert this low-pressure head into electricity using direct-drive low-speed permanent magnet generators (EPRI (2005)).

Another device which harnesses ocean waves by overtopping waves is the WavePlane (Fig. 1.8). This is a V-shaped construction anchored with the tip facing the incoming waves. In front, below the surface line, the wave plane is equipped with an artificial beach that makes the capture of the wave energy more efficient. The wave plane is symmetrical in its construction. The water from the waves is caught in different heights through an inlet divided into separate levels. Further the water is let into this inlet tangentially through the turbine pipe. Through this process it is sought to maintain as much of the water's kinetic energy as possible in consideration of the manageable volume. The kinetic energy is used to generate a rotating stream of water in the turbine pipe. At the end of the turbine pipe which is at the end of the two

Figure 1.8: Overtopping: the wave plane (WavePlane 2010).

"legs in the V-shape" the turbine pipe bends back and downwards. It is able to bring the end of the drive train outside the turbine pipe. From the turbine the water is led back into the sea. By means of a gear box the turbine runs a generator, which is connected to the electrical grid (Wave energy centre (2010)). Other devices developed by this principle are: the Floating Wave Power Vessel (FWPV) (Powertech (2009)), the Tapered Channel Wave Power Device (TAPCHAN) (Powertech (2009)), the Seawave Slot-Cone Generator (SSG), the SSG offshore installation (Waveeenergy (2010)), and the WaveBlanket (Gatti (2010)).

1.2.4 Point Absorbers

Point absorber is a WEC oscillating with either one or more degrees of freedom. It can either move with respect to a fixed reference, or respect to a floating reference (Backer et al. (2007)). A point absorber which is a floating structure moves relative to its own components due to the wave action (e.g., a floating buoy inside a fixed cylinder) therefore, this relative motion is used to drive an electromechanical or hydraulic energy converter.

For a wave energy converter (WEC) device, to be a point absorber, the linear dimension has to be much smaller than the prevailing wave length. As general rule, to consider a WEC as a point absorber, its respective diameter should be preferably in the range of five to ten percent of prevailing wavelengths (Falnes and Lillebekken (2003)). Point absorbers devices, can be classified according to the degree of freedom from which they capture the ocean energy. A brief explanation of the respectively mode of capture are described below.

Figure 1.9 Point absorbers: (a) the Powerbuoy, (b) the Aquabuoy and (c) the AWS. (Sinha 2015).

a) Heaving systems

Heaving point absorber are the ones that harness ocean wave energy based on heave motion while the remaining movements are restricted by the mooring system which is fixed to the ocean bottom. During the past years, heaving point absorbers have been studied and developed to capture ocean wave energy because of the simplicity in their hydrodynamic problem and similarity with the well-known buoys. Moreover, most of these devices are similar in nature with a difference in the PTO system.

An example of a point absorber device is the Powerbuoy, developed by Ocean Power Technologies (Fig. 1.9 (a)). The construction involves a floating structure with one component relatively immobile, and a second component with movement driven by wave motion (a floating buoy inside a fixed cylinder). The relative motion is used to drive electromechanical or hydraulic energy converters. A PowerBuoy demonstration unit rated at 40 kW was installed in

2005 for testing offshore from Atlantic City, New Jersey, U.S. testing in the Pacific Ocean is also being conducted, with a unit installed in 2004 and 2005 off the coast of the Marine Corps Base in Oahu, Hawaii.

Another example is The AquaBuoy (Fig. 1.9 (b)) (Weinstein et al. (2004)) being developed by the AquaEnergy Group, Ltd. is a point absorber that is the third generation of two Swedish designs that utilize the wave energy to pressurize a fluid that is then used to drive a turbine generator. The vertical movement of the buoy drives a broad, neutrally buoyant disk acting as a water piston contained in a long tube beneath the buoy. The water piston motion in turn elongates and relaxes a hose containing seawater, and the change 10 in hose volume acts as a pump to pressurize the seawater. The AquaBuoy design has been tested using a full-scale

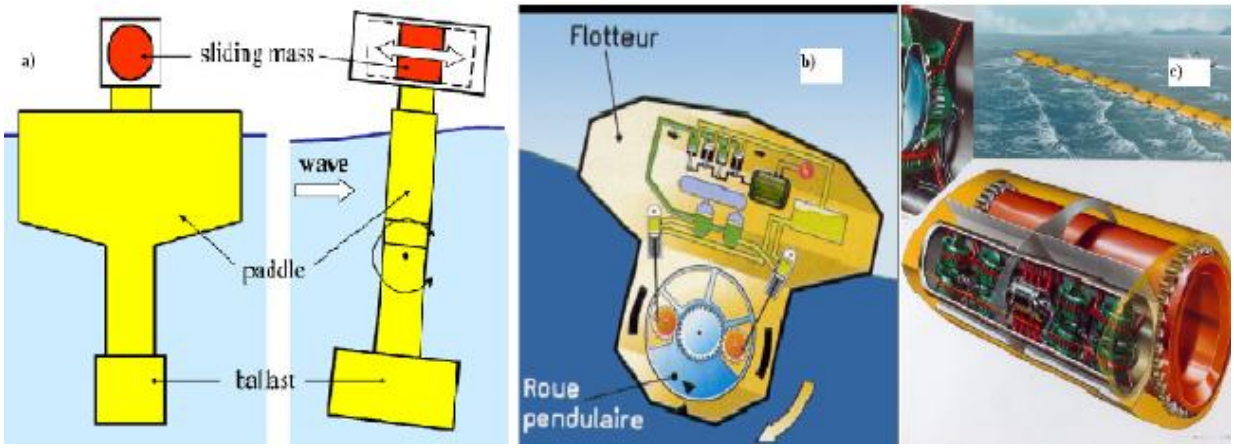

Figure 1.10: Point Absorber: (a) The PS FrogMk5, (b) the Searev and (c) the nodding Duck. (Sinha 2015).

prototype, and a 1 MW pilot offshore demonstration power plant is being developed offshore at Makah Bay, Washington.

Other point absorbers that have been tested at prototype scale include the Archimedes Wave Swing (AWS) (Fig. 1.9 (c)) (Prado (2008)). This device is quite different relative to the ones described above. The AWS is a submerged structure unlike the Aquabuoy and the Powerbuoy which are floating on the ocean surface. The technology of the AWS consists of an air-filled cylinder that moves up and down as waves pass over. This motion relative to a second cylinder fixed to the ocean floor is used to drive a linear electrical generator. A 2 MW capacity device has been tested offshore of Portugal (Gardner (2005)). Other point absorber devices are the Swedish heaving buoy, with linear electrical generator, the Norwegian heaving buoy and the IPS buoy (Edinburgh University).

b) Pitching systems

Pitching systems are other oscillating-body systems in which the energy conversion is based on relative rotation (mostly pitch) rather than translation. Examples of this point absorber type are: The PS FrogMk5 (McCabe (2006)) which consists of a large buoyant paddle with an integral ballasted handle hanging below it (Fig. 1.10 (a)). Waves act on the blade of the paddle and the ballast beneath provides the necessary reaction. When the WEC is pitching, power is extracted by partially resisting the sliding of a power-takeoff mass which moves in guides above sea level.

Another example is the nodding Duck created by Stephen Salter, from the University of Edinburgh and the Searev (Babarit et al. (2005)) wave energy converter, developed at Ecole Centrale de Nantes, France, is a floating device enclosing a heavy horizontal-axis wheel

serving as an internal gravity reference (Fig. 1.10 (b)). The centre of gravity of the wheel being off-centred, this component behaves mechanically like a pendulum. The rotational motion of this pendular wheel relative to the hull activates a hydraulic PTO which, in turn, sets an electrical generator into motion. Major advantages of this arrangement are that: (a) 11 all the moving parts (mechanical, hydraulic, electrical components) are sheltered from the action of the sea inside a closed hull, and (b) the choice of a wheel working as a pendulum involves neither end-stops nor any security system limiting the stroke.

1.3 Boundary Element Method

Boundary element methods were developed through the effort to deal with problems of aerodynamics. The rapid evolution of computers and information technology in 1970 leads to the development of Finite Element Methods (FEM) and Boundary Element Methods (BEM). A synoptic description and comparison of the most popular methods for the numerical solution of Boundary Value Problems (BVP) follows. Almost every physical phenomenon can be described using differential equations and proper boundary conditions. A BVP, only in very simple and not so interesting cases, can be solved analytically, i.e. solutions is possible to be found, that satisfy both the governing equation and the boundary conditions. Thus, two different philosophies begun from the same threshold, the approximate solution of BVPs. The Finite Element Method is based on the theory of Ritz (1909) and the basic idea was that the solution should satisfy exactly the boundary conditions and the effort is concentrated to the best, approximate, satisfaction of the differential equation. On the other hand, Boundary Element Method have been developed in the foundations of Trefftz's (1926) theory. In the latter case, differential equation is satisfied exactly and the boundary conditions are approximated with the minimum error. In FEM the domain is divided into elementary subdomains where the equation is satisfied. In that way the solution is not enforced to satisfy exactly both the differential equation and the boundary conditions. The unknown parameters of the solution, consist to its values at the intersection points (nodes) of the elementary subdomains, are evaluated under the demand of minimization of the error due the approximation of the differential equation. The achievement of that method is that the solution has the minimum divergence from the exact solution which satisfies the governing equation globally at the domain, however there are points in the domain where the equation is violated. On the contrary, BEM does not require a subdivision of the domain and an approximation of the solution of the differential equation. Solution is composed of fundamental solutions/singularities also known as Green functions, each of them satisfies the equation and through the appropriate representation theorem (based on Greens theorem, see e.g. Kress 1989) the total does too. The singularities are distributed on the boundaries where the boundary

conditions should be valid. The demand of boundary conditions' satisfaction with maximum accuracy leads to the solution of a Boundary Integral Equation (BIE). The boundary is divided in boundary elements where we can approximate the boundary conditions using e.g. a collocation scheme.

Comparing the two numerical methods we can see that BEM seems to be superior at many points:

• In BEM only a surface (or linear for 2D) and not space (or surface for 2D) integration is involved and thus the dimension of the problem is of one order lower in comparison with FEM and finally the number of unknowns is significantly smaller in the first case.

• Another advantage is that the solutions in BEM satisfies a priory the differential equation (or almost everywhere, because we have to except the singularity points) and thus the method is able to encounter problems with infinite domain, which is practically impossible for FEM for obvious reasons.

• Furthermore in BEM, spatial subdivision is not required, which is in many cases a difficult problem of numerical analysis (see Beer et all 2008 and Kress 1991)

• Finally, as a result of the first advantage and the fact that usually in low order BEMs (panel methods) the required integral calculations can be evaluated analytically, the computational cost and the time of computation are significantly lower. This last advantage of BEMs indicate that they are ideal for 3D and strongly unsteady problems.

However, BEM is not panacea and has some drawbacks. The requirement of simple fundamental solution is the most serious one. If the fundamental solution is not simple, the computational cost rises. Furthermore, the evaluation of singular integrals that appears in BEMs presents difficulties. However, extended study has been done concerning the singularities of fundamental functions which consists of integral kernels form boundary integral equations e.g. we mention Muskhelishvili (1953), Mikhlin (1965), Polyanin & Manzhirov (2008). Finally, we mention that the state of the art in computational methods is concentrating in the development of higher order BEM (see e.g. Cottrel et al, 2009, Lee and Kerwin, 2003, Belibassakis et al, 2013) as well as sophisticated hybrid BEM-FEM models. These models applies every method in the region that it works more efficient (e.g. concerning Computational Fluid Dynamics, CFD, in the thin boundary layer region FEM is applied for the solution of Direct Navier Stokes, DNS, and outside of the boundary layer, or when the unsteadiness is strong, BEM is applied, due to the great amount of calculations) in this way the advantages of both methods are exploited see e.g. Beer et al (2008).

Chapter 2

PML-BEM FOR THE 2D WAVE MAKER PROBLEM

2. BEM for flapper wave maker (2D problem)

The Boundary Element Method (BEM) is the most common method to solve boundary value problem for the Laplace equation, modelling irrotational flows, in conjunction with appropriate boundary conditions completing the formulation, as e.g.,

- $\Phi = g_1$, Dirichlet boundary data
- $\frac{\partial \Phi}{\partial n} = g_2$, Neumann boundary data
- $\frac{\partial \Phi}{\partial n} + \alpha \Phi = g_3$, Mixed type (Robin) boundary data

see, e.g., Katz & Plotkin (1991), Beer et al (2008). In this chapter we shall study in more detail the linearized problem of a wavemaker, which has an analytical solution. The latter solution for a flap-type and a piston-type wavemaker will be used as a prototype in order to test the accuracy of a low-order BEM, which will be used in conjunction with an absorbing layer technique in order to truncate the computational domain and enforce the radiation condition. Subsequently the performance of the absorbing layer controlling the accuracy of the BEM numerical scheme will be optimized by comparison to the analytical solution, and the conclusions will be used for the extension of the method to 3D (in subsequent chapter).

2.1 Evaluation of the wave potential in semi infinite strip

In this section we consider harmonic water wave propagation in a semi-infinite two-dimensional strip of constant depth *h*, extending from a horizontal bottom surface to the free surface; see Fig.2.1. In the case of waves of small amplitude and slope the linearized problem is governed by the Laplace equation. Introducing a Cartesian coordinate system with origin at

some point on the mean water level (z=0) the mathematical formulation consists of the field equation

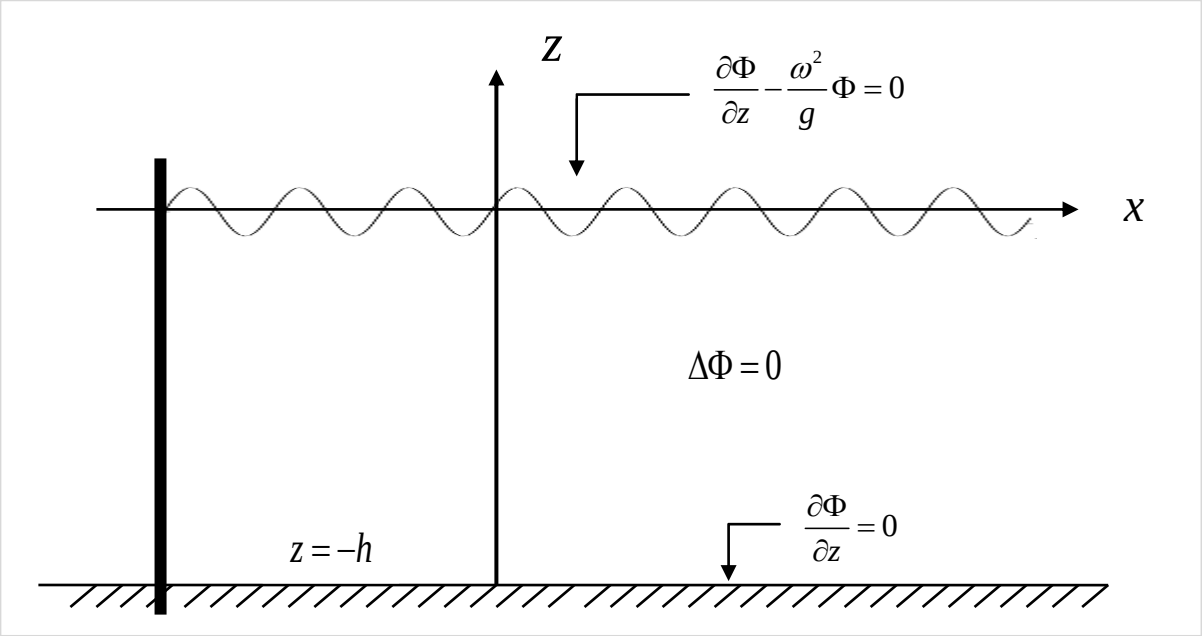

Figure 2.1 Wave potential in semi-infinite strip. Wavemaker problem.

$$\frac{\partial^2\Phi}{\partial x^2}+\frac{\partial^2\Phi}{\partial z^2}=0, \quad \text{in} \quad -h<z<0, \quad a<x<\infty \ , \tag{2.1}$$

the free surface boundary condition

$$\frac{\partial\Phi}{\partial z}-\mu\Phi=0\,, \ z=0 \tag{2.2}$$

and the bottom boundary condition,

$$\frac{\partial\Phi}{\partial n}\equiv\frac{\partial\Phi}{\partial z}=0\,, \quad z=-h, \tag{2.3}$$

where $\mu=\omega^2/g$ is the frequency parameter, ω is the angular frequency of the waves and g the acceleration of gravity.

A representation of solutions of Eqs.(2.1)-(2.3) is obtained using separation of variables, which reformulates the problem to a system of ordinary differential equations. The latter are used in conjunction with the boundary conditions leading to the solution(s). So we end up to an

equation that connects the wave frequency ω with the wavenumber *k*, that is also dependent on the depth *h* of the strip. The process of separation of variables is based on seeking solutions in the form $\varphi(x,z) = X(x)\cdot Z(z)$, which substituted in the Laplace equation gives us

$$X(x)\cdot Z(z)\cdot\left[\frac{\ddot{X}(x)}{X(x)}+\frac{\ddot{Z}(z)}{Z(z)}\right]=0 \Rightarrow \ddot{X}(x)+k_n^2 X(x)=0 \quad \& \quad \ddot{Z}(z)-k_n^2 Z(z)=0\ , \tag{2.4}$$

The boundary conditions (2.2) and (2.3) can only be satisfied from the function *Z*(*z*) and thus, we obtain the following Sturm Liouville problem for the vertical eigenvalues

$$\left\{\begin{array}{c}\ddot{Z}(z)-k_n^2 Z(z)\\ \dot{Z}(z)-\mu Z(z), z=0\\ \dot{Z}(z)=0, z=-h\end{array}\right\} \Rightarrow\ Z_0(z)=\frac{\cosh\left[k_0(z+h)\right]}{\cosh(k_0 h)},\ n=0,\quad Z_n(z)=\frac{\cos\left[k_n(z+h)\right]}{\cos(k_n h)},\ n\geq 1, \tag{2.5}$$

$$\omega^2 = k_0 g\tanh(k_0 h) \qquad \textit{and} \qquad \omega^2 = -k_n g\tan(k_n h),\ n\geq 1 \tag{2.6}$$

Also, we obtain for

$$X_0(x)=\exp(\pm i k_0 x), n=0 \qquad \textit{and} \qquad X_n(x)=\exp(\pm k_n x), n\geq 0, \tag{2.7}$$

Equation (2.6) is the generalized dispersion equation, and the specific equation for n=0 provides a relation between frequency and wavenumber. The roots of the dispersion equation are presented graphically in Figs. 2 and 3. From the latter results, we easily obtain that that $k_n \to n\pi/h,$ for $n\to\infty.$

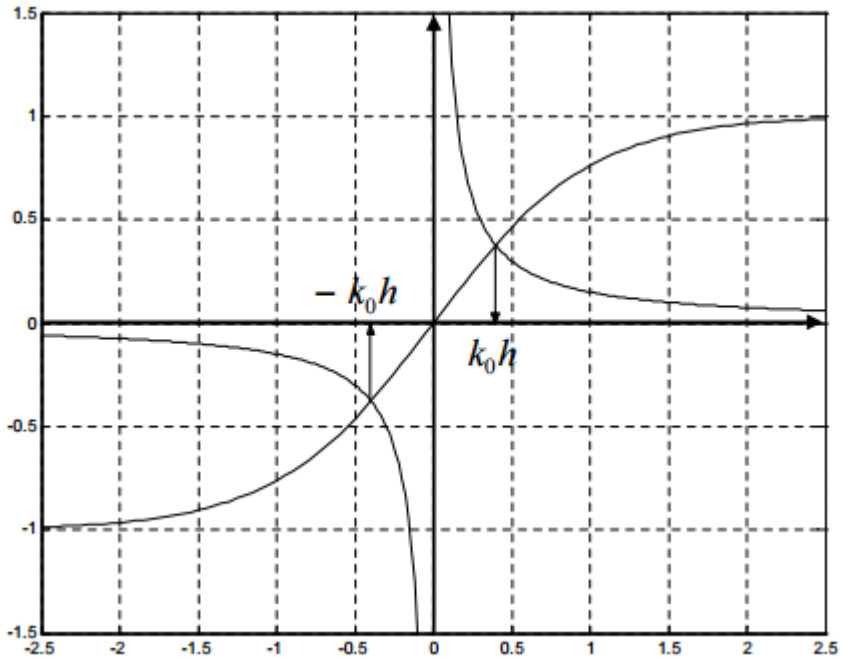

Figure 2.2: Graphical solution for the dispersion equation ($\omega^2 = k_0 g \tanh(k_0 h), n = 0$)

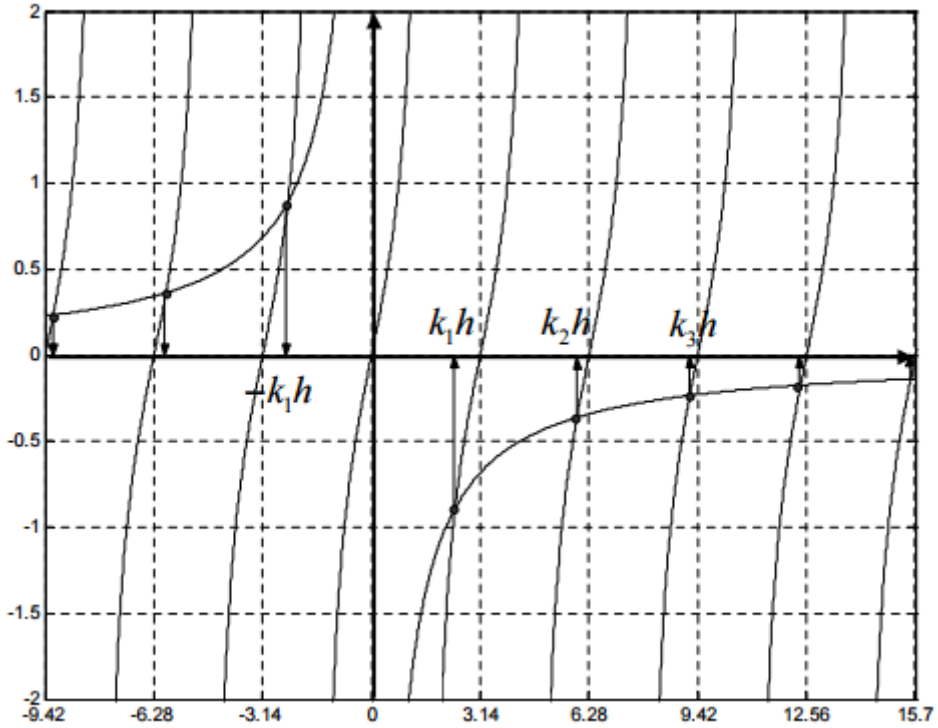

Figure 2.3: Graphical solution for the dispersion equation ($\omega^2 = -k_n g \tan(k_n h), n \geq 1$)

All above constitute a regular Sturm-Liouville system and the numbers k_n are known as eigenvalues of this system (Coddington & Levinson 1972). The solution of the eigenvalue problem has some very interesting properties, which are listed below:

1. $k_n \in \mathbb{R} \quad and \quad n \in \mathbb{N}$

2. In every k_n corresponds only one linearly independent eigenfunction $Z_n(z)$

3. The eigenfunctions are mutually orthogonal:

$$\langle Z_n, Z_m \rangle := \int_{z=-h}^{z=0} Z_n(z) \cdot Z_m(z)\, dz = \delta_{nm} \|Z_n\|^2, \quad \delta_{nm} = \begin{cases} 0, & if\ n \neq m \\ 1, & if\ n = m \end{cases} \tag{2.8}$$

4. The eigenfunctions form an orthonormal system

$$\tilde{Z}_n(z) = \frac{z_n(z)}{\|z_n\|} \Rightarrow \langle \tilde{Z}_n, \tilde{Z}_m \rangle = \delta_{nm} \tag{2.9}$$

where δ_{nm} is Kroneckers delta.

5. The eigenfunctions constitute base on the space $L_2(-h,0)$ and generalize the Fourier systems, which means that every function in the interval $-h < z < 0$ is represented in the generaised Fourier series

$$f(z) = \sum_{n=0}^{\infty} \frac{\langle f, Z_n \rangle}{\|Z_n\|^2} Z_n(z) = \sum_{n=0}^{\infty} \langle f, \tilde{Z}_n \rangle \tilde{Z}_n(z), \tag{2.10}$$

6. The completeness of the Sturm-Liouville systems permits the rpresentation of Dirac's delta function i the form:

$$\delta(z - z_0) = \sum_{n=0}^{\infty} \tilde{Z}_n(z) \tilde{Z}_n(z_0) \tag{2.11}$$

Using Eqs (2.5) and (2.7) we obtain the general representation of the solutions for the potential in the semi-infinite strip, as follows

$$\varphi(x,z) = \left(A_0^+ e^{ik_0 x} + A_0^- e^{-ik_0 x}\right) Z_0(z) + \sum_{n=1}^{\infty} A_n e^{-k_n x} Z_n(z), \tag{2.12}$$

$$\eta(x) = -\frac{i\omega}{g} \varphi(x, z=0) = -\frac{i\omega}{g} \left(A_0^+ e^{ik_0 x} + A_0^- e^{-ik_0 x}\right) + \sum_{n=1}^{\infty} A_n e^{-k_n x}, \tag{2.13}$$

In the above equation the first part illustrates the right-propagating mode and the second the reflected mode, while the rest terms (n>0) are evanescent modes, which are exponentially decaying at infinity, $x \to \infty$.

The above equations are general representations in the right-semi infinite strip, and constitute solutions of the problem for every possible value of the coefficients $\{A_n, n = 0,1,2,.....\}$. In the next subsection these coefficients will be analytically calculated for the proble of flap-type and piston-type wavemekers, positioned and operating on the vertical boundary x=0 (without loss of generality)

`

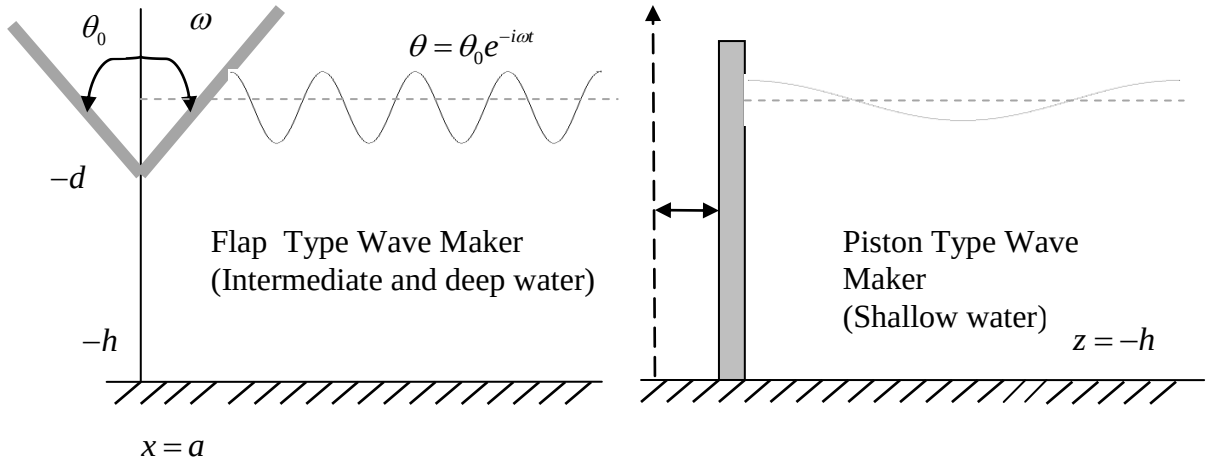

Figure 2.4: Flap and Piston type wave makers

2.2 Solution for a flap and a piston wave maker potential

In Fig .2.4 the two types of wave makers are sketched. The flap-type wavemaker rotates a flap about a pivot point at $z = -d$ and generates waves with frequency ω which is equal to the rotation frequency. The piston-type wavemaker is oscillating horizontally. The flap approximates better water waves in intermediate and deep water depth conditions and the piston type is better for waves in swallow water conditions.

The flap-type wavemaker rotating around the pivot point at $-d$ and, for small rotational amplitudes, generates horizontal flow velocities equal to $\omega(z+d)$, for $z>-d$. Below this point there is a rigid wall and thus, horizontal velocity is zero, for $z<-d$. In the case of the piston-type wavemaker, the horixontal flow velocity is constant all over the water column.

Consequently, the boundary conditions at $x = a$ are :

For the flap type wave maker:

$$\frac{\partial \varphi}{\partial x} = -\frac{\partial \varphi}{\partial n} = -i\omega(z+d), \quad -d < z < 0 \tag{2.14}$$

$$\frac{\partial \varphi}{\partial x} = 0, \quad -h < z < -d \tag{2.15}$$

For the piston type wave maker:

$$\frac{\partial \varphi}{\partial x} = -i\omega, \quad -h < z < 0 \tag{2.16}$$

Subsequently, exploiting the properties of vertical eigenfunctions (eigensolutions of the Sturm-Liouville problem) the problem is analytically solved by determining the coefficients of the series (2.14),(2.15),(2.16) to satisfy the above boundary conditions, and the results are as follows

Flap-type wave maker:

$$\varphi_{,x}(x=0,z) = A_0 ik_0 e^{ik_0 x} Z_0(z) - \sum_{n=1}^{\infty} A_n k_n e^{-k_n x} Z_n(z) = f(z) = \sum_{n=0}^{\infty} \frac{\langle f, Z_n \rangle}{\|Z_n\|^2} Z_n(z) \tag{2.17}$$

and thus,

$$A_0 ik_0 = \frac{\langle f, Z_0 \rangle}{\|Z_0\|^2} \Rightarrow A_0 = -\frac{i\omega}{ik_0} \frac{G_0}{\cosh k_0 h} \frac{1}{N_0}, \text{ where } N_0 = \|Z_0\|^2 = \frac{1}{2} \frac{\cosh(k_0 h)\sinh(k_0 h) + k_0 h}{k_0 \cosh^2(k_0 h)} \text{ and}$$

$$G_0 = \int_{z=-d}^{z=0} (z+d)\cosh\left[k_0(z+h)\right] dz \Rightarrow$$

$$G_0 = \int_{u=-d+h}^{u=h} (u+d-h)\cosh(k_0 u) du = \frac{(d-h)}{k_0}\left[\sinh(k_0 h) - \sinh\left[k_0(h-d)\right]\right] +$$

$$+ \frac{1}{k_0}\left(h\sinh(k_0 h) - (h-d)\sinh\left[k_0(h-d)\right]\right) - \frac{1}{k_0^2}\left(\cosh(k_0 h) - \cosh\left[k_0(h-d)\right]\right) \tag{2.18}$$

and

$$-A_n k_n = \frac{\langle f, Z_n \rangle}{\|Z_n\|^2} \Rightarrow A_n = -\frac{i\omega}{k_n} \frac{G_n}{\cos(k_n h)} \frac{1}{N_n}, \; N_n = \|Z_n\|^2 = \frac{1}{2} \frac{\cos(k_n h)\sin(k_n h) + k_n h}{k_n \cos^2(k_n h)}$$

$$G_n = \int_{z=-d}^{z=0} (z+d)\cos\left[k_n(z+h)\right] dz \;\; \Rightarrow$$

$$G_n = \frac{(d-h)}{k_n}\left(\sin(k_n h) - \sin\left[k_n(h-d)\right]\right) + \frac{1}{k_n}\left(h\sin(k_n h) - (h-d)\sin\left(k_n(h-d)\right)\right)$$

$$+ \frac{1}{k_n^2}\left(\cos(k_n h) - \cos\left[k_n(h-d)\right]\right) \tag{2.19}$$

For the piston type wave maker:

$$\varphi_{,x}\left(x=0,z\right)=A_0 ik_0 e^{ik_0 x}Z_0\left(z\right)-\sum_{n=1}^{\infty}A_n k_n e^{-k_n x}Z_n\left(z\right)=f\left(z\right)=\sum_{n=0}^{\infty}\frac{\langle f,Z_n\rangle}{\left\|Z_n\right\|^2}Z_n\left(z\right) \qquad (2.20)$$

$$A_0 ik_0=\frac{\langle f,Z_0\rangle}{\left\|Z_0\right\|^2}\Rightarrow A_0=-\frac{i\omega}{ik_0}\frac{G_0}{\cosh k_0 h}\frac{1}{N_0},\qquad N_0=\left\|Z_0\right\|^2=\frac{1}{2}\frac{\cosh\left(k_0 h\right)\sinh\left(k_0 h\right)+k_0 h}{k_0\cosh^2\left(k_0 h\right)}$$

$$G_0=\int_{z=-h}^{z=0}\cosh[k_0\left(z+h\right)dz,\ u=z+h \qquad (2.21)$$

$$G_0=\int_{u=0}^{u=h}\cosh\left(k_0 u\right)du=\frac{1}{k_0}\left[\sinh\left(k_0 h\right)\right]$$

$$-A_n k_n=\frac{\langle f,Z_n\rangle}{\left\|Z_n\right\|^2}\Rightarrow A_n=-\frac{i\omega}{k_n}\frac{G_n}{\cos\left(k_n h\right)}\frac{1}{N_n},\ N_n=\left\|Z_n\right\|^2=\frac{1}{2}\frac{\cos\left(k_n h\right)\sin\left(k_n h\right)+k_n h}{k_n\cos^2\left(k_n h\right)}$$

$$G_n=\int_{z=-h}^{z=0}\cos\left[k_n\left(z+h\right)\right]dz=\frac{1}{k_n}\left[\sin\left(k_n h\right)\right] \qquad (2.22)$$

The above analytical solutions for the potential of the flap-type and the piston-type wave maker are comparatively plotted in Fig.5 for a depth equal to $1m$. The frequency is selected equal to $2.3\,rad/\sec$, and thus theratio of wavelength to waterdepth is $h/\lambda=0.15$ corresponding to intermediate water depth.

According to Fig. 2.5, it seems that piston wave maker gives a greater value of potential for these parameters. It is an expected result, since piston wave maker oscillates moving one meter from its equilibration spot. Otherwise the flap-type wave maker oscillates rotating the flap 1 rad from the pivot point. Consequently, the piston type presents greater value of potential in comparison with the flap-type. Generally, the piston-type wave maker behaves better in swallow and intermediate water, while the flap-type operates better in deep water.

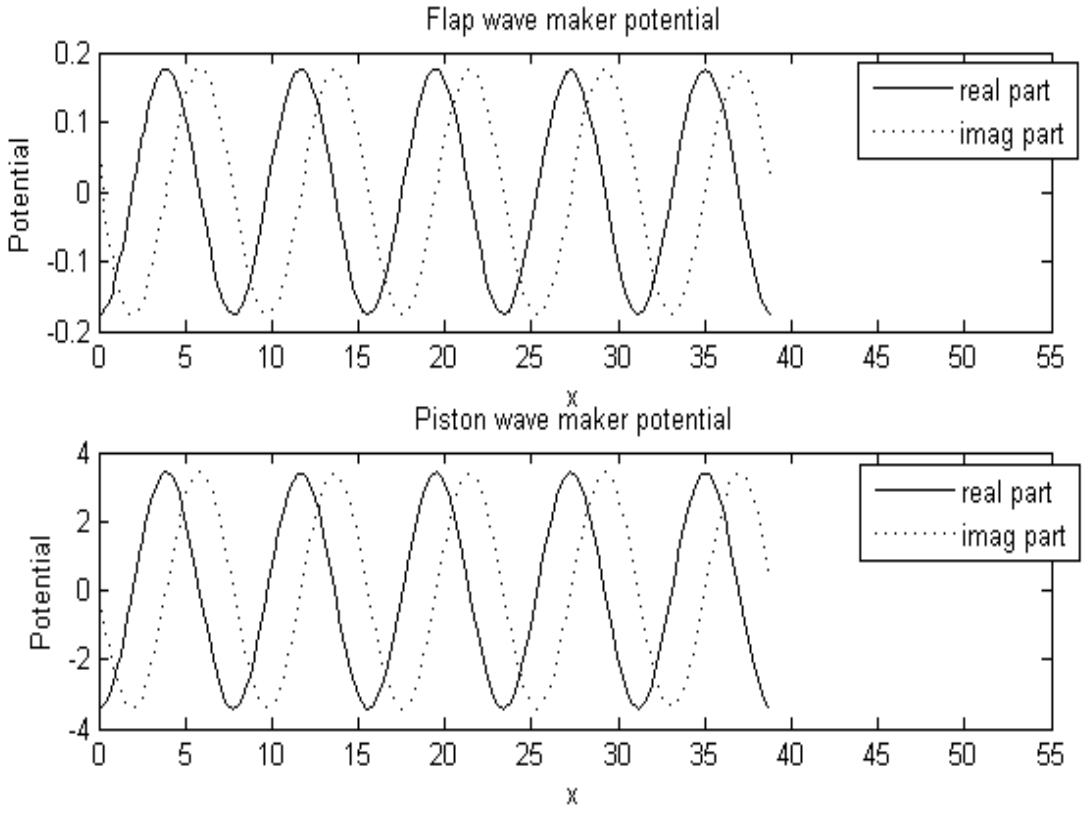

Figure 2.5: Flap-type and piston-type wave maker potential distribution on the free surface.

Following the Galvin(1964) simplified theory for plane wavemakers, we will end up that the piston type wavemaker is more appropriate in swallow water than the flap type wavemaker. In shallow water, a simple theory for the generation of waves by wavemakers was proposed by Galvin **(1964),** who reasoned that the water displaced by the wavemaker should be equal to the crest volume of the propagating wave form. For example, consider a piston wavemaker with a stroke *S* which is constant over a depth ***h.*** The volume of water displaced over a whole stroke is *Sh* (see Figure 2.6). The volume of water in a wave crest is

$$\int_0^{L/2} (H/2)\sin kx\,dx = H/k \tag{2.23}$$

Equating the two volumes

These two relationships are shown as the straight dashed lines in Figure 2.7

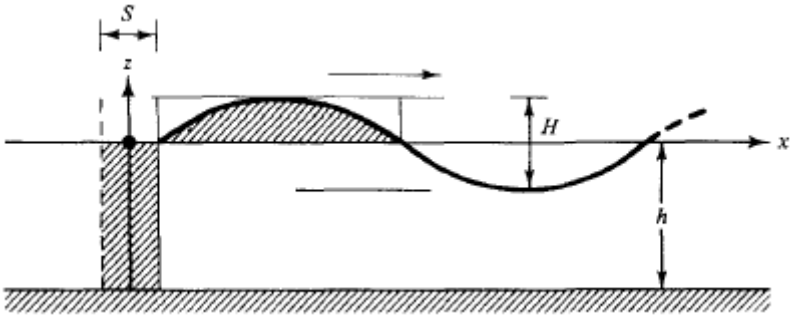

Figure 2.6: Simplified shallow water piston-type wavemaker theory of Galvin

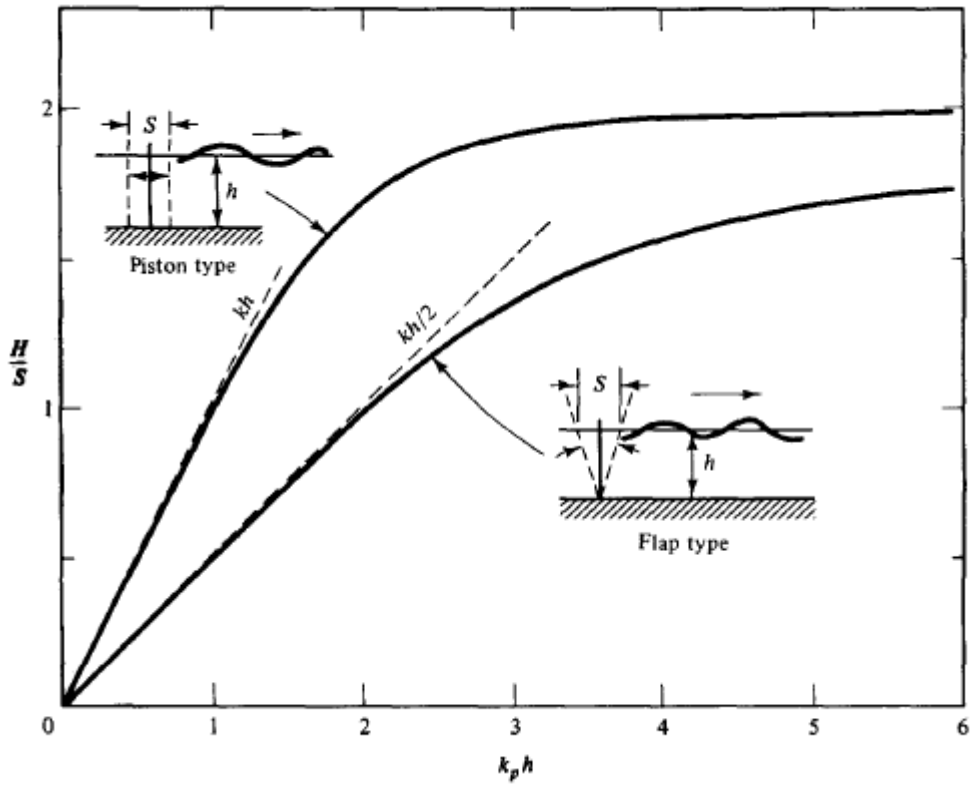

Figure 2.7: Plane wavemaker theory. Wave height to stroke ratios versus relative depths. Piston and flap type wavemaker motions

If we consider for the piston type wavemaker stroke $S=X_0=1$ and for the flap-type wavemaker stroke $S=\theta_0=1$ then the equations for wave response height to stroke ratio H/S

PISTON TYPE

$$\frac{H}{S}=\frac{H}{2\mathrm{X}_0}=2\frac{\sinh^2(kh)}{kh+\cosh(kh)\sinh(kh)}=2\frac{\tanh^2(kh)}{\frac{kh}{\cosh^2(kh)}+\tanh(kh)}=2\frac{\cosh(2kh)-1}{2kh+\sinh(2kh)} \qquad (2.24)$$

Shallow water: $kh\to 0,\quad \frac{H}{S}=\frac{H}{2\mathrm{X}_0}=2\frac{(kh)^2}{kh+kh}=kh$

Deep water: $kh \to \infty, \quad \frac{H}{S} = \frac{H}{2X_0} = 2\frac{1}{0+1} = 2$

FLAP TYPE

In the special case of $d=h$ for the flap type

$$\frac{H}{S} = \frac{H}{2h\theta_0} = \frac{\omega^2}{kgh}\frac{\frac{1-\cosh(kh)+kh\sinh(kh)}{k^2}}{\frac{kh+\cosh(kh)\sinh(kh)}{2k\cosh(kh)}} = 2\frac{\tanh(kh)}{kh}\frac{\left(1-\cosh(kh)+kh\sinh(kh)\right)}{\frac{kh}{\cosh(kh)}+\sinh(kh)} \qquad (2.25)$$

$$\frac{H}{S} = 4\frac{\tanh(kh)}{kh}\frac{\left(1-\cosh(kh)+kh\sinh(kh)\right)\cosh(kh)}{2kh+\sinh(2kh)} = 4\frac{\sinh(kh)}{kh}\frac{\left(1-\cosh(kh)+kh\sinh(kh)\right)}{2kh+\sinh(2kh)}$$

Shallow water: $kh \to 0, \quad \frac{H}{S} = 2\frac{-0.5(kh)^2+(kh)^2}{kh+kh} = \frac{kh}{2}$

Deep water: $kh \to \infty, \quad \frac{H}{S} = \frac{H}{2X_0} = 2\frac{1}{0+1} = 2$

$$Sh = \frac{H}{k} = \frac{H}{2}\left(\frac{L}{2}\right)\frac{2}{\pi} \qquad (2.26)$$

in which the $2/\pi$ factor represents the ratio of the shaded area to the area of the enclosing rectangle (i.e., an area factor). This equation can also be expressed

$$\left(\frac{\mathrm{H}}{S}\right)_{piston} = kh$$

where *H/S* is the height-to-stroke ratio.

This relationship is valid in the shallow water region, $kh < \pi/10$**.** For a flap wavemaker, hinged at the bottom, the volume of water displaced by the wavemaker would be less by a factor of **2.**

$$\left(\frac{H}{S}\right)_{flap} = \frac{kh}{2}$$

Consequently, the piston type wave maker is more efficient than the flap type wave maker in swallow water.

2.3 2D Boundary Element Method

In the semi infinity strip problem we have taken the analytic solution, but in more complicated problems we cannot take solutions like this. Consequently it is very important to find a method that would approximate the solution of a more complicate problem. Boundary element method is that we need to solve difficult problems numerically. The state of art of this method is to approximate the domain's boundary with panels (1st order BEM) and to distribute fundamental solutions of Laplace equation on the center of each panel. Consequently, the whole boundary problem is converted to an integral equation, which is open to numerical solution. In the $2\,D$ problem the Laplace's fundamental solution is $G(\mathbf{x}\,|\,\mathbf{y}) = \frac{1}{2\pi}\ln|\mathbf{x}-\mathbf{y}|^{-1}$ and is referred as source function. This solution has the property to evaluate the equation

$$\Delta_x G(\mathbf{x}\,|\,\mathbf{y}) = \frac{\partial^2 G(\mathbf{x}\,|\,\mathbf{y})}{\partial x_1^2} + \frac{\partial^2 G(\mathbf{x}\,|\,\mathbf{y})}{\partial x_2^2} = -\delta(\mathbf{x}-\mathbf{y}), \quad \mathbf{x}\in\mathbb{R}^2 \tag{2.27}$$

where $\mathbf{y} = (y_1, y_2) \in D$ is a fixed point in domain D and

$\mathbf{x} = (x_1, x_2) \in D$ is the general field point in domain D and

$\delta(\mathbf{x}-\mathbf{y}) = \delta(x_1 - y_1)\delta(x_2 - y_2)$ is the Dirac function which is defined by the equation

$$\int_\Omega \sigma(\mathbf{x})\delta(\mathbf{x}-\mathbf{y})\,dx = \sigma(\mathbf{y}), \forall\sigma\in C_0^\infty(\Omega) \tag{2.28}$$

The method has many variations, one of these is based on the Green's second theorem

$$\iiint_D (\Phi\cdot\Delta G - G\cdot\Delta\Phi)\,dV = \iint_{\partial D}\left(\Phi\cdot\frac{\partial G}{\partial\mathbf{n}} - G\cdot\frac{\partial\Phi}{\partial\mathbf{n}}\right)dS \tag{2.29}$$

Using the Green's theorem we end up that the potential in any point of the interior of the domain can be represented by surface distribution of sources or sinks with the following equation

$$\varphi(\mathbf{x}) = \int_{\partial D}\sigma(\mathbf{y})G(\mathbf{x}\,|\,\mathbf{y})\,ds(\mathbf{y}),\ \sigma(\mathbf{y}):\textit{uknown source strength} \tag{2.30}$$

The velocity for any point of the interior of the domain is given by

$$\mathbf{u} = \nabla\varphi = \nabla_x\left(\int_{\partial D}\sigma(\mathbf{y})G(\mathbf{x}\,|\,\mathbf{y})\,ds(\mathbf{y})\right) = \int_{\partial D}\sigma(\mathbf{y})\nabla_x G(\mathbf{x}\,|\,\mathbf{y})\,ds(\mathbf{y}), \tag{2.31}$$

The gradient is get inside of the integral and is applied on $G(\mathbf{x}|\mathbf{y})$, because $\sigma(\mathbf{y})$ is considered constant on each panel so it is independent of the space variable. All above are referred in the interior problem. When we are moving on the boundary, one additional term is added in the velocity's equation.

$$\mathbf{u} = \frac{\sigma(\mathbf{y})\mathbf{n}(\mathbf{x})}{2} + \int_{\partial D} \sigma(\mathbf{y}) \nabla_x G(\mathbf{x}|\mathbf{y}) ds(\mathbf{y}), \qquad (2.32)$$

$\mathbf{n}(\mathbf{x})$ is the unit normal vector to the boundary ∂D directed into the exterior of D. The normal component of velocity is given from the scalar product of

$$\mathbf{u},\mathbf{n}(\mathbf{x}) : \mathbf{u}(\mathbf{x})\mathbf{n}(\mathbf{x}) \equiv \frac{\partial \varphi}{\partial \mathbf{n}} = \frac{\sigma(\mathbf{x})}{2} + \mathbf{n}(\mathbf{x}) \int_{\partial D} \sigma(\mathbf{y}) \nabla_x G(\mathbf{x}|\mathbf{y}) ds(\mathbf{y}),\ \mathbf{x} \in \partial D \qquad (2.33)$$

So, if we define the conditions as $g_0(\mathbf{x}),\ \mathbf{x} \in D$ for the Dirichlet problem and $g_n(\mathbf{x}),\ \mathbf{x} \in \partial D$ for the Neumann problem, then the above equations become :

$$\int_{\partial D} \sigma(\mathbf{y})\, G(\mathbf{x}|\mathbf{y}) ds(\mathbf{y}) = g_0(\mathbf{x}),\ \mathbf{x} \in D \qquad (2.34)$$

$$\frac{\sigma(\mathbf{x})}{2} + \mathbf{n}(\mathbf{x}) \int_{\partial D} \sigma(\mathbf{y}) \nabla_x G(\mathbf{x}|\mathbf{y}) ds(\mathbf{y}) = g_n(\mathbf{x}),\ \mathbf{x} \in \partial D \qquad (2.35)$$

In order to evaluate these integrals, we must approximate the geometry of boundary with another simpler geometry. Here we use a low-order BEM and we approximate the boundary with panels. The disadvantage of the low order in comparison with the high order BEM methods is that we need a large number of elements to find a solution with a great accuracy. Hence, we approximate, in figure 2.8, the boundary's geometry with a polygon, whose panels have the same length.

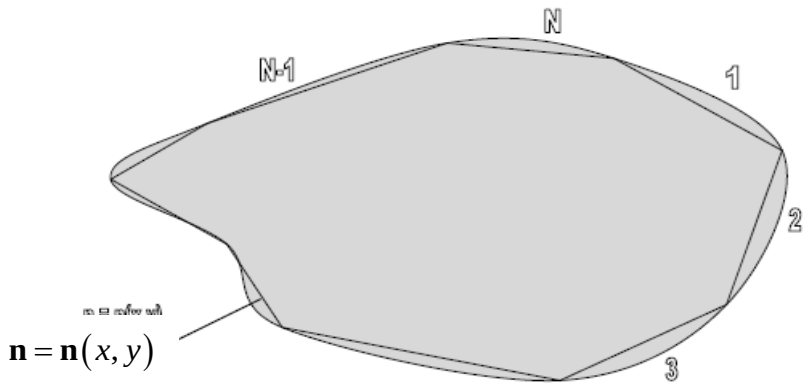

Figure 2.8: Approximation of the boundary in the case of low-order BEM by a polygon.

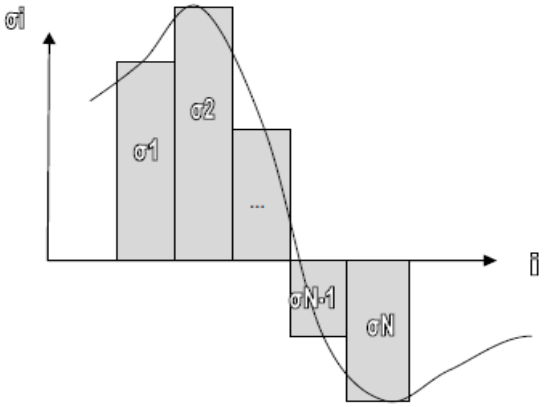

Figure 2.9: Histogram with source and doublet distributions on each panel.

As the number of panels increases, the polygon's shape converges to the domain's boundary geometry and respectively the numerical solution tends to the analytical. Evaluating the normal vector for each panel, makes possible to solve the integral equation. The idea is to assume the source distribution constant in each panel, so that the approximate distribution is illustrated as an histogram (Figure 2.9) and verges on the actual form of sources. In our example, are used source and doublet distributions but there are vortex distributions, which are useful to approximate vorticity problems. The strength of sources will be evaluated, solving a linear system and as the number of panels is being increased, the distribution is converging to the real form.

In any case the integrals above are hard to evaluate, even for simple forms of sources, even if the surface on which the sources are distributed is a straight line. Thus, we select a certain number N of points on the boundary, called nodes, and connect the nodes with straight lines, creating the panels of the method. Now the equations can be written :

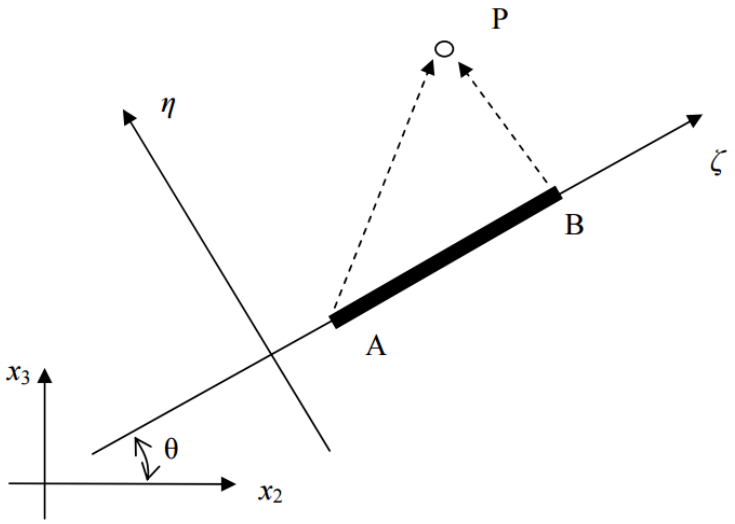

Figure 2.10: Panel local coordinate system

$$\varphi = \sum_{n=1}^{N} \int_{panel\ j} \frac{\sigma(s)\ln r}{2\pi} ds \tag{2.36}$$

We insert local coordinate system for each panel (see Figure 2.10) to evaluate the integrals, as it is shown in Fig.2.10. We have to find the induced potential and velocity of a point P with coordinates (x_2, x_3) from the source distribution of a panel which is defined between the nodes A with general coordinates $\left(x_2^{\mathrm{A}}, x_3^{\mathrm{A}}\right)$ and B with general coordinates $\left(x_2^{\mathrm{B}}, x_3^{\mathrm{B}}\right)$. The local system is consists of ζ, an axis parallel to the line AB and η, an axis perpendicular to ζ. In his system, the nodes A and B have more simple coordinates like $(\zeta_{\mathrm{A}}, 0)$ for A and $(\zeta_{\mathrm{B}}, 0)$ for B. We assume that the potential and velocity are induced by the midpoint of panel AB to the point P. Thus, the results that give us the induced units from a panel to a point are listed below:

$$\varphi(\zeta,\eta) = -\frac{\sigma}{2\pi}\left\{\begin{array}{l}(\zeta-\zeta_{\mathrm{A}})\ln\left[(\zeta-\zeta_{\mathrm{A}})^2+\eta^2\right]-(\zeta-\zeta_{\mathrm{B}})\ln\left[(\zeta-\zeta_{\mathrm{B}})^2+\eta^2\right] \\ +2\eta\left(\tan^{-1}\left(\frac{\eta}{\zeta-\zeta_{\mathrm{B}}}\right)-\tan^{-1}\left(\frac{\eta}{\zeta-\zeta_{\mathrm{A}}}\right)\right)\end{array}\right\} \tag{2.37}$$

$$u_{\zeta}(\zeta,\eta) = -\frac{\sigma}{2\pi}\ln\left(\frac{(\zeta-\zeta_{\mathrm{A}})^2+\eta^2}{(\zeta-\zeta_{\mathrm{B}})^2+\eta^2}\right) \tag{2.38}$$

$$u_{\eta}(\zeta,\eta) = -\frac{\sigma}{2\pi}\left(\tan^{-1}\left(\frac{\eta}{\zeta-\zeta_{\mathrm{B}}}\right)-\tan^{-1}\left(\frac{\eta}{\zeta-\zeta_{\mathrm{A}}}\right)\right) \tag{2.39}$$

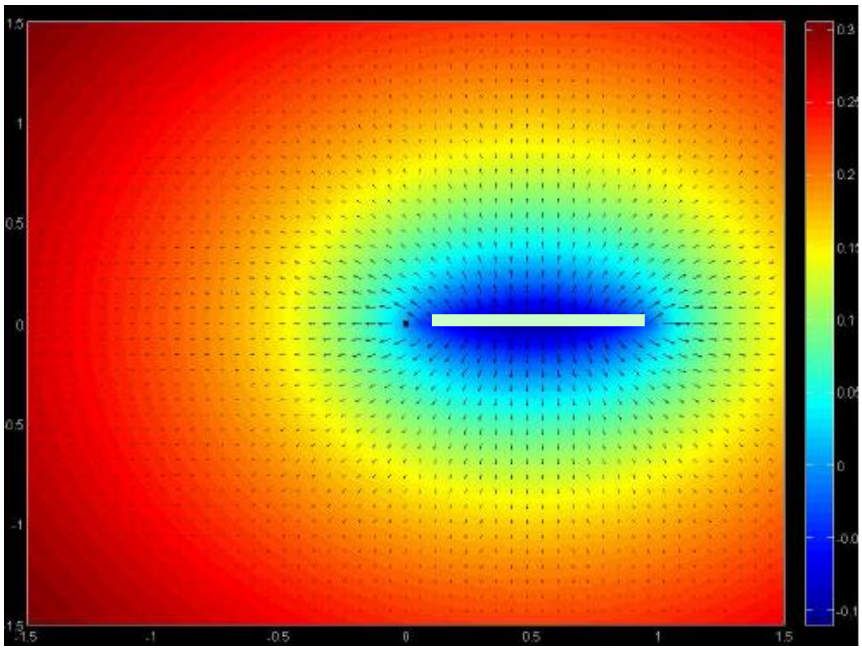

Fig. 2.11 Induced potential and flow velocities from a linear element, as calculated using Eqs.(2.33)-(2.35). A colorbar is used to indicate the values of the potential.

The final results are taken with a transformation to the general coordinates system with the equations below:

$$u_{x2}(x_2,x_3)=u_{\zeta}(\zeta,\eta)\cos(\theta)-u_{\eta}(\zeta,\eta)\sin(\theta) \tag{2.40}$$

$$u_{x3}(x_2,x_3)=u_{\zeta}(\zeta,\eta)\sin(\theta)+u_{\eta}(\zeta,\eta)\cos(\theta) \tag{2.41}$$

where $\theta=\tan^{-1}\left(\dfrac{x_3^B-x_3^A}{x_2^B-x_2^A}\right)$ (2.42)

As an example the induced potential and flow velocities from a linear element extending from A= (0,0) to B=(1,0) are shown in Fig. 2.11.

On the basis of the above, we finally end up to a linear system of equations :

$$\sum_{k=1}^{N}A_{jk}\sigma_k=g_j,\quad j=1,\ldots,N \tag{2.43}$$

where g_j is the condition we apply to the boundary. If $g(P_j)=\varphi(P_j)$, it is a Dirichlet condition. If $g(P_j)=\dfrac{\partial\varphi(P_j)}{\partial n}$ it is a Neumann condition. The A_{jk} denote the effect of the center of the $k-panel$ to the center of the $j-panel$. In order to solve this linear system, we have to reverse the equation and we take the source strength for each panel. Then, it is possible to evaluate forces and moments which are exerted.

2.4 Numerical results concerning the flapping wave maker problem

After this introduction in BEM, we present an application of this method for the semi infinity strip problem in order to compare the analytic solution with the numerical. An algorithm has developed, to apply the BEM and to find the analytic and numerical solution.

First, the domain is divided into 3 regions, as it is shown in Figure 2.12:

1. The free surface, where the absorbing layer is applied. (M_1)
2. The fixed and the moving part(d=0.3m) of the flapper. (M_2)
3. The rigid bottom. (M_3)

Then, are given the frequency and the depth as inputs and then using the dispersion equation we find the wave length and the wave number. Subsequently, the geometry is created locating nodes on the boundary. We have 3 sections, one for the free surface , one for the flap wave maker and the wall and one for the bottom. Specifically, the number of nodes is increased in the region of flap wave maker, since the flap is moving and we want better approximation.

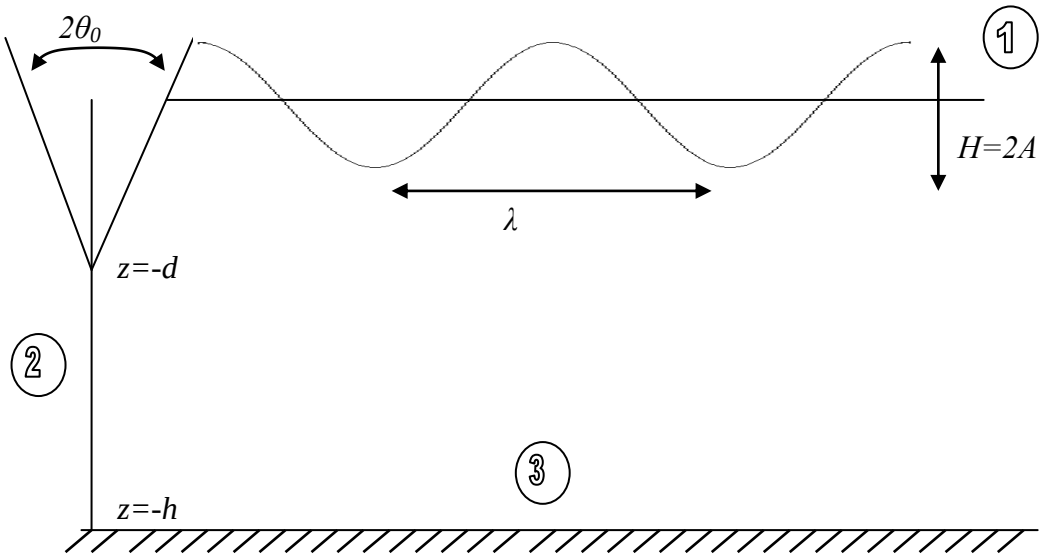

Figure 2.12: The semi infinity strip domain including the Flap wave maker.

Furthermore, we follow the process, which referred above, finding the midpoint, the horizontal and vertical components of the unit normal vector and the angle between the local and the general coordinate system. Then, a matrix is created with the right states $g\left(P_j\right)$ of the conditions. A subroutine is called to evaluate the induced potential and velocity from $i-panel$ to $j-panel$. Thus, a matrix is created with the left states of the conditions and the linear system is solved, giving the source strengths in each panel. The linear system is presented below:

$$\frac{\sigma_k}{2}+\sum_{m=1}^{M}\sigma_m\left(n_k U_{km}-\mu\varphi_{km}\right)=0,\quad k=1,M_1 \tag{2.44}$$

where

$$\mu(\omega)=\frac{\omega^2}{g}\cdot\left(1+i\tilde{c}\frac{|x-\lambda|^n}{\lambda^n}\right) \tag{2.45}$$

with $\tilde{c}=0$ for $x<\frac{r}{\lambda}$.

In addition the following boundary conditions hold on the wave maker

$$\frac{\sigma_k}{2}+\sum_{m=1}^{M}\sigma_m\left(n_k U_{km}\right)=f\left(y\right),\quad k=M_1+1,\ \sum_{i=1}^{2}M_i \tag{2.46}$$

where

$$f\left(y\right)=\begin{cases}0, & y<-d\\ i\omega\left(y+d\right), & y\geq -d\end{cases} \tag{2.47}$$

and on the bottom surface

$$\frac{\sigma_k}{2}+\sum_{m=1}^{M}\sigma_m\left(n_k U_{km}\right)=0,\quad k=\sum_{i=1}^{2}M_i+1,\ \sum_{i=1}^{3}M_i \tag{2.48}$$

Then, another subroutine is called to evaluate the analytic solution in the same nodes as in the numerical. Finally, the real and imagine parts of the exact and the approximates solution are plotted and we observe the difference between them.

2.4.1 Radiation Condition

It is very important to define the radiation condition. This condition is referred to the wave behavior far from the stimulation field. Essentially, this condition illustrates the deadening of the wave as it fends off the stimulation point. It cannot be formulated a priori as a physical restriction of the problem, but it is applied after a very careful preliminary analysis of the equations of the problem. Radiation condition forms the final analytical solution. For example, in the general solution of the semi infinity problem is showed up a term that is being increased exponentially, while the distance from the stimulation field is getting bigger. This does not make sense, so with the radiation condition this term is deleted. Thus, we cannot claim that radiation condition is a common condition. Nevertheless, we can find the radiation condition only in problems that we know the analytical solution or the semi-analytical. So, it is necessary to find a manner to approximate radiation condition in complicated problems, as we referred above. One way to overcome this obstacle is the absorbing layer, which we used in the program, in order to evaluate the solution. An important task concerning the present scheme deals with the treatment of horizontally infinite domain and the implementation of appropriate radiation-type conditions at infinity. The present work is based on the truncation of the domain and on the use of Perfectly Matched Layer (PML) model, as e.g. described by Berenger (1994) and Turkel, Yefet (1998), optimized by Collino, Monk (1998); see also Filippas, Belibassakis (2014). This deadening is generated by a term that is included to the free surface condition far from the wave's stimulation point. We can tell that is an imagine part of frequency, which reduces the solution to zero. $\mu(\omega)=\frac{1}{g}\left(\omega+i\,c\left|x-x_0\right|^n\right)^2=\frac{\omega^2}{g}\left(1+i\tilde{c}\,\frac{\left|x-x_0\right|^n}{\lambda^n}\right)^2$ .The effectiveness of the layer depends on the following dimensionless parameters:

- Dimensionless Frequency, $\tilde{\omega}=\sqrt{\frac{\omega^2\cdot h}{g}}$
- Coefficient, $\tilde{c}=\frac{c\cdot\lambda^n}{\omega}$
- The activation length(or activation distance per wave length), $x_0\left(\frac{r}{\lambda}\right)$
- The exponent, n
- The number of panels per wave length, $\frac{N}{\lambda}$

2.4.2 Absorbing layer and optimization

In order to optimize the absorbing layer, to approximate well the radiation condition, we have written a program, that compares the analytical solution with the approximate solution for various values of parameters. It takes 3 values for each parameter and are showed in the matrix below

	Shallow	Intermediate	Deep
$\tilde{\omega}$	0.3193	0.7343	1.6922
$\tilde{c}$	0,0089	7,4843	2100,6
r/λ	3	4	4.5
n	2	3	4
N/λ	10	20	30

We run the program for the flap wave maker 243 times, in order to capture all the combinations and to find the conjuction that will approximate better the radiation condition. The program for the flapper is used as a subroutine, which accepts the parameters from the main program and finds the analytical and the numerical solution. Then, the solutions are abstracted and we check the potential for the nodes, which are before the region in which the absorbing layer is activated. So, we want the absorbing layer to effect as little as possible in the region, where it does not operate. The control is fulfilled using a Chebyshev norm thus we find the biggest error for the potential real and imagine part. The values of frequency are chosen to fluctuate $1-5\,rad/\sec$, to cover the case of swallow , intermediate and deep water, as it is shown in Figure 2.13. We do that because the absorbing layer behave differently in each case . The absorbing layer does not approximate very well the radiation condition in deep water and it displays errors with the analytic solution. Consequently, when we choose frequency equal to 5 rad per second the error is greater than in the other cases.

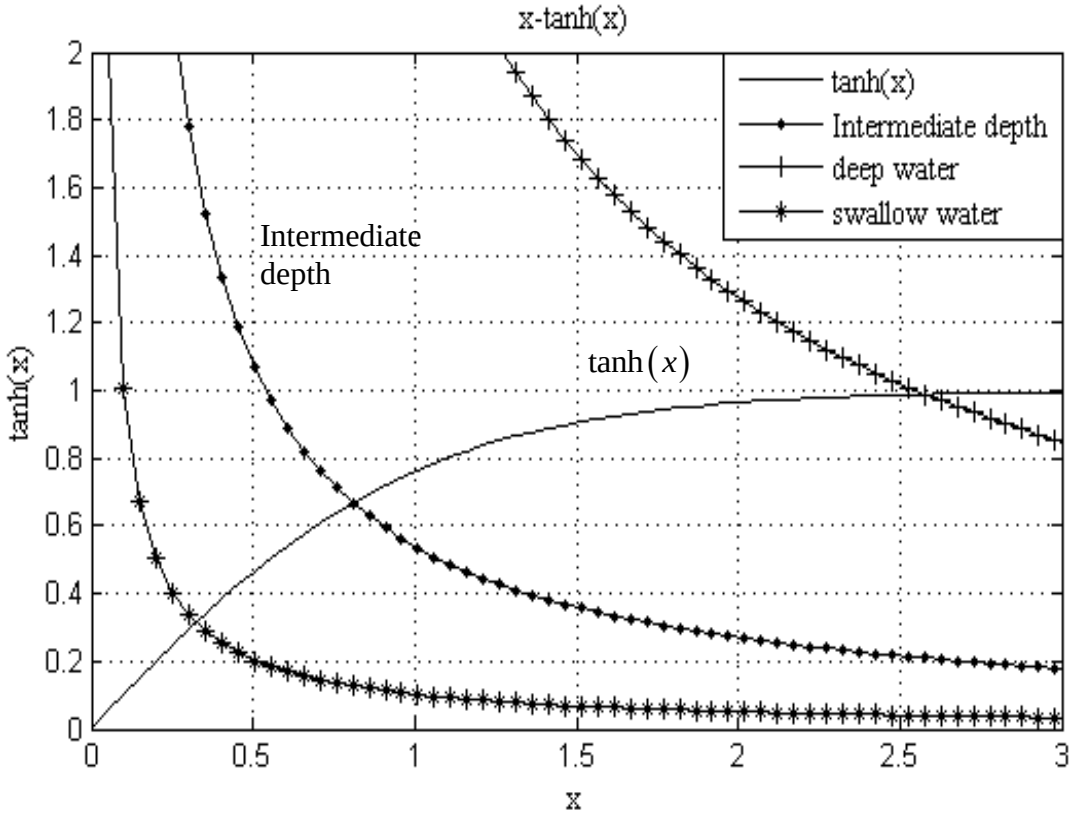

Figure 2.13: Graphical swallow, intermediate and deep water lines.

After running the program for all the combinations we choose the combination with the minimum error and essentially we have found the parameters for the absorbing layer. Below are listed some charts, showing the comparison between the analytical and the approximate solution for various values of parameters. Firstly, are plotted the solutions with bad approximations for the imagine part and great approximation for the real. Then are shown the best approximations for each value of the frequency.

Case : $\tilde{\omega} = 0.3193 \quad \tilde{c} = 2100.6 \quad n = 4 \quad r/\lambda = 3 \quad \mathrm{N}/\lambda = 30$

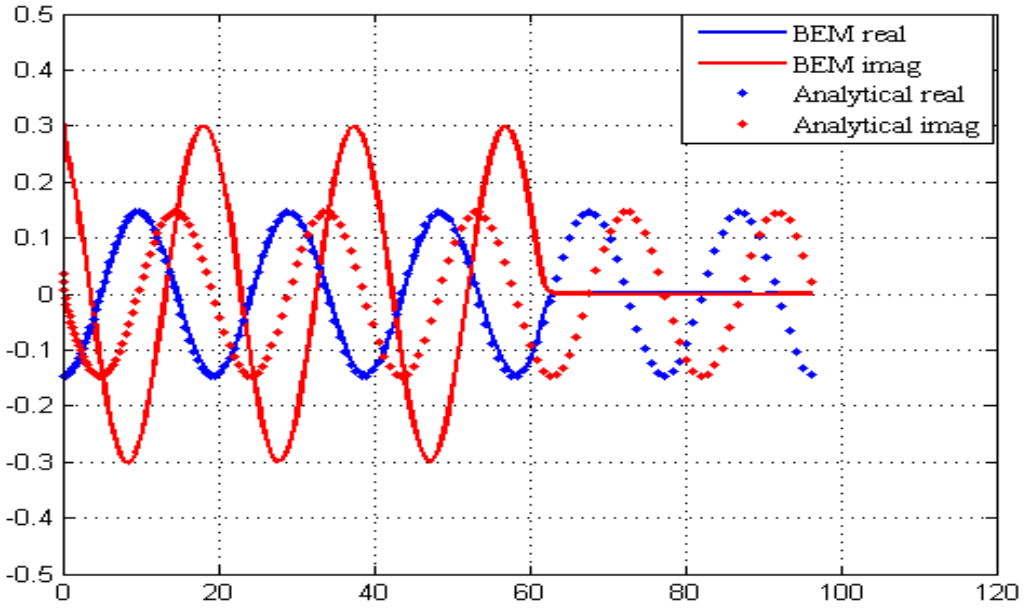

Figure 2.14:Comparison of the analytic and approximate solution for the real and imaginary part.

Case : $\tilde{\omega} = 0.7343 \quad \tilde{c} = 0.2634 \quad n = 2 \quad r/\lambda = 4 \quad \mathrm{N}/\lambda = 30$

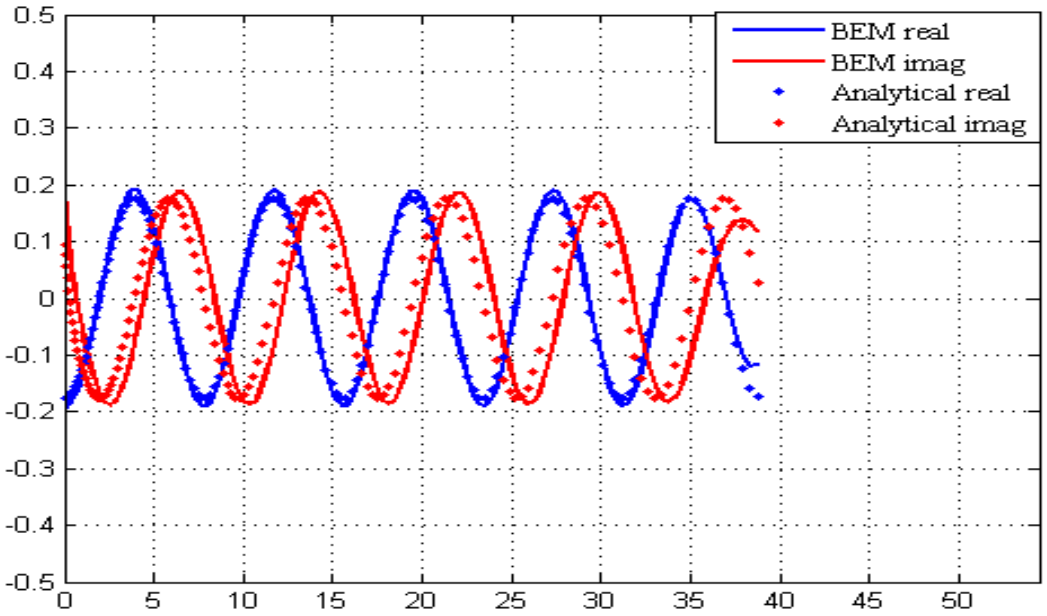

Figure 2.15:Comparison of the analytic and approximate solution for the real and imaginary part.

Case : $\tilde{\omega}=1.6922 \quad \tilde{c}=0.0292 \quad n=3 \quad r/\lambda=3 \quad \mathrm{N}/\lambda=30$

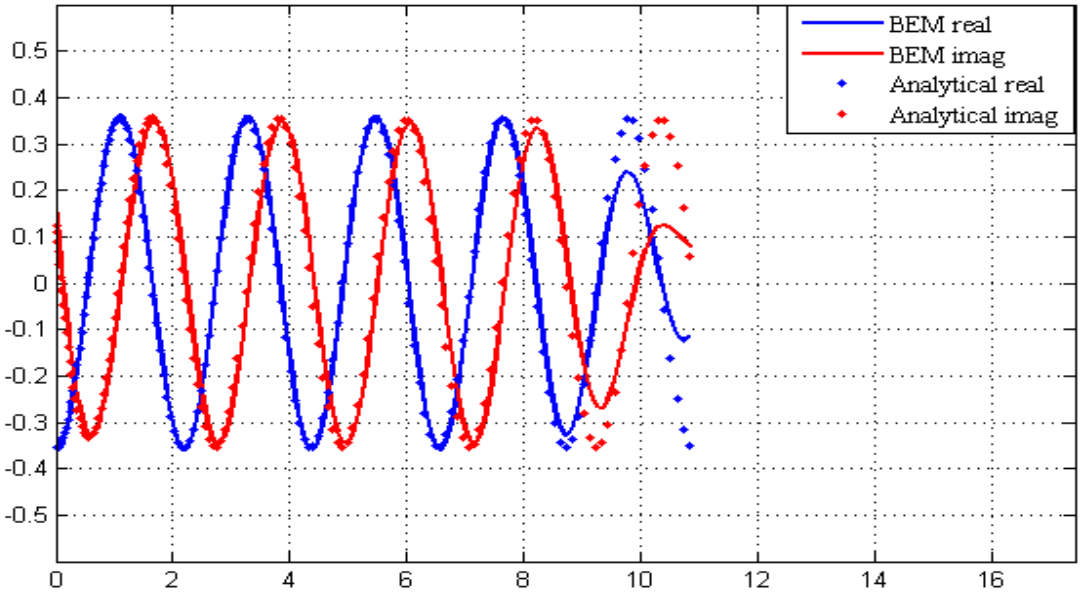

Figure 2.16:Comparison of the analytic and approximate solution for the real and imaginary part.

Case : $\tilde{\omega}=0.3193 \quad \tilde{c}=3.7422 \quad n=2 \quad r/\lambda=3 \quad \mathrm{N}/\lambda=30$

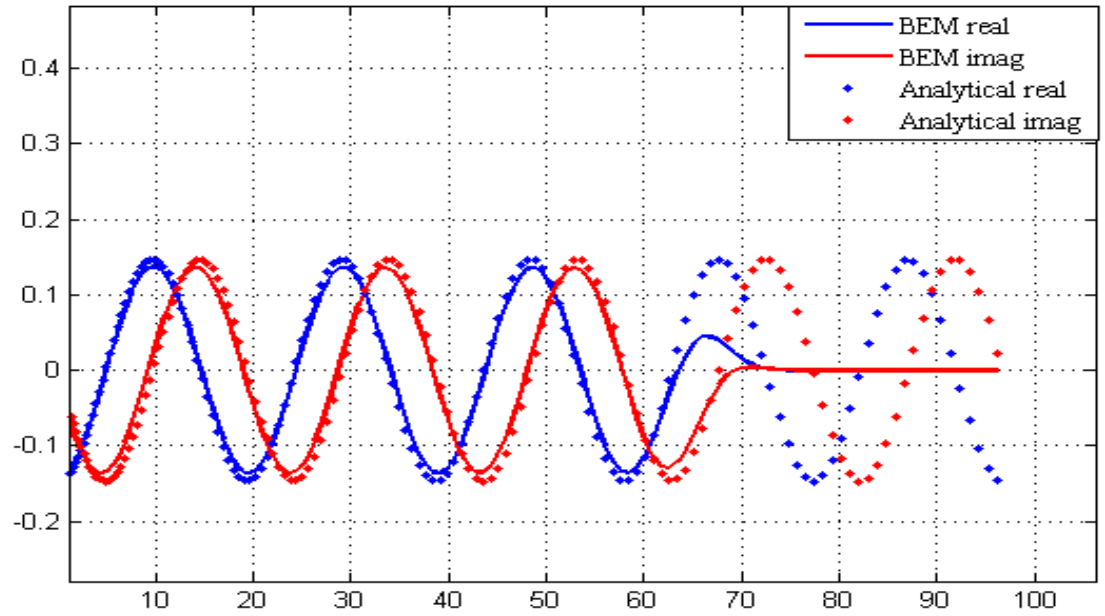

Figure 2.17:Comparison of the analytic and approximate solution for the real and imaginary part.

Case : $\tilde{\omega} = 0.7343 \quad \tilde{c} = 0.5269 \quad n = 2 \quad r/\lambda = 4 \quad N/\lambda = 30$

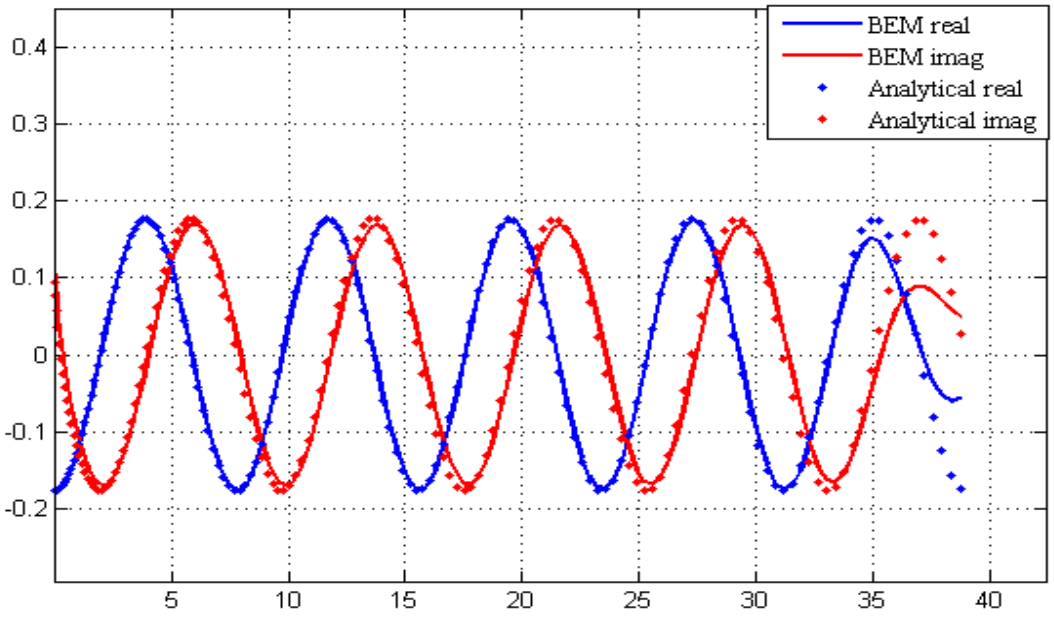

Figure 2.18:Comparison of the analytic and approximate solution for the real and imaginary part.

Case : $\tilde{\omega} = 1.6922 \quad \tilde{c} = 0.2634 \quad n = 4 \quad r/\lambda = 3 \quad N/\lambda = 30$

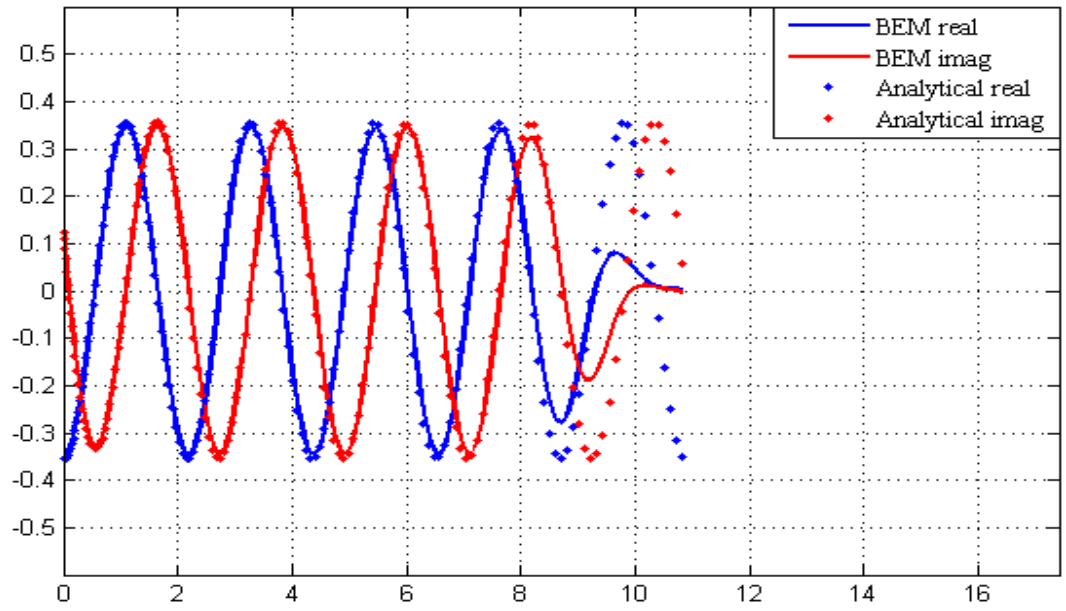

Figure 2.19: Comparison of the analytic and approximate solution for the real and imaginary part.

Furthermore, 9 diagrams are presented, in order to understand how effects each variable to the absorbing layer and to find those combinations of variables, that give the minimum error. In them we see the error as a function of the exponent n and the activation length r/λ. The number of panels per wave length was held constant and equal to 30 because the solution is approximated better as the number of panels is increased. There are three diagrams for each value of frequency and each diagram includes the solution for one of the three values of the coefficient.

1. $\omega = 1\, rad/\sec \quad and \quad coefficient = 0,01$

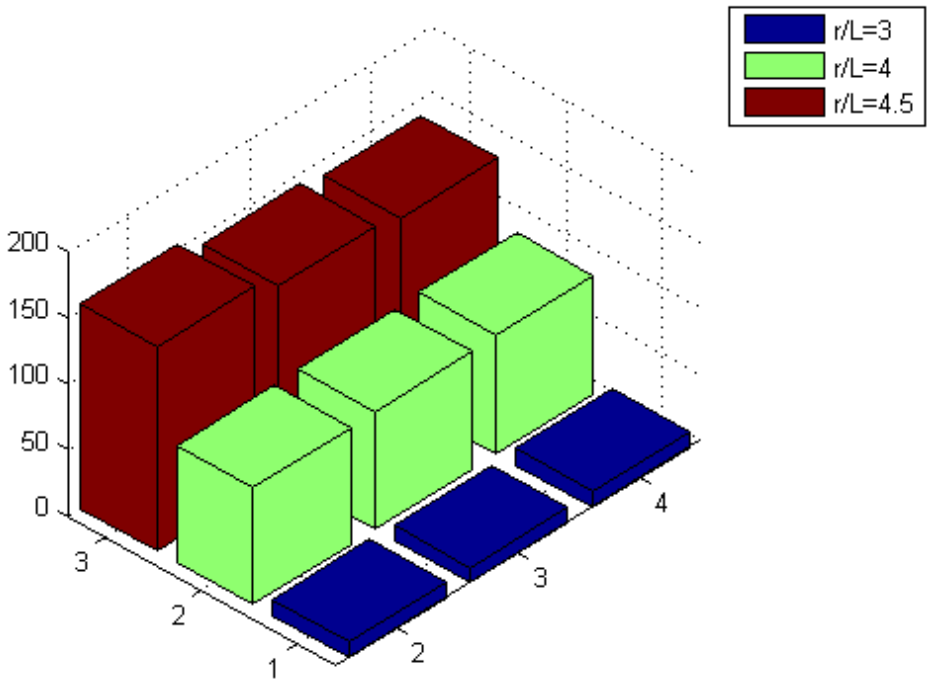

Figure 2.20: Error presentation for various values of the parameters.

2. $\omega = 1\,rad/\sec \quad and \quad coefficient = 0,015$

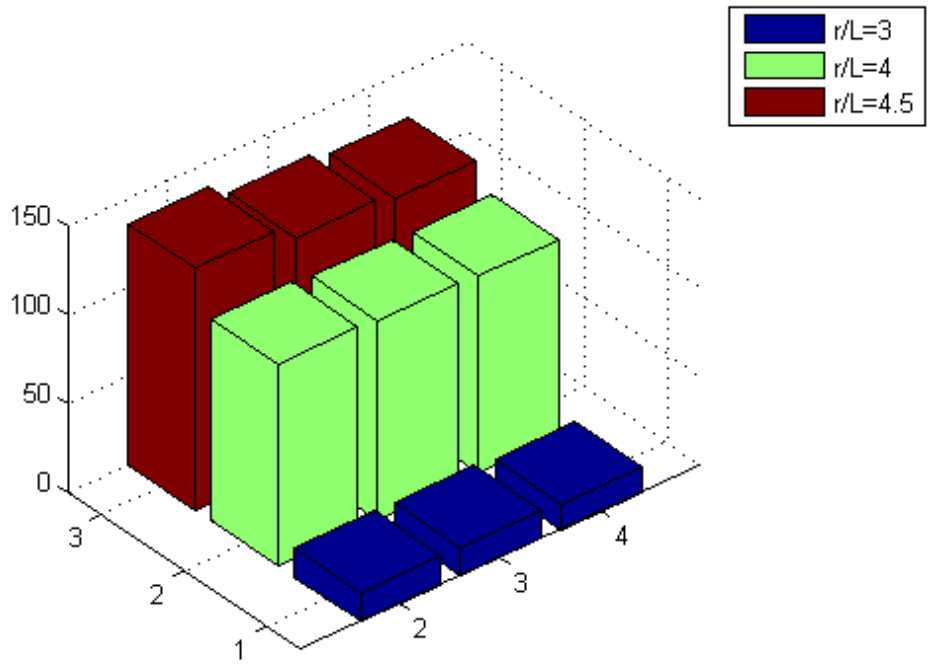

Figure 2.21: Error presentation for various values of the parameters.

3. $\omega = 1\,rad/\sec \quad and \quad coefficient = 0,02$

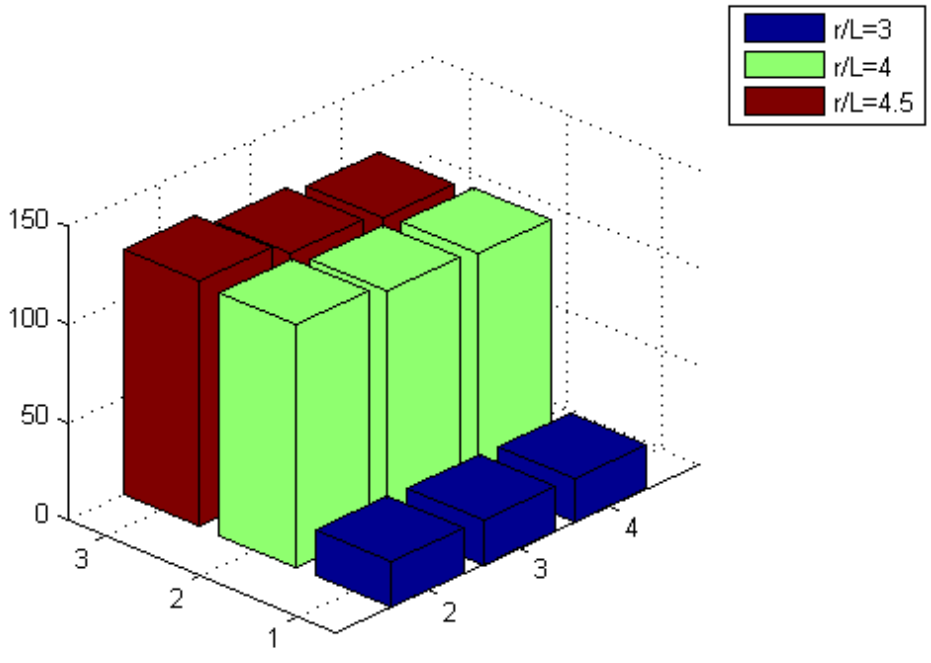

Figure 2.22: Error presentation for various values of the parameters

4. $\omega = 2.3\, rad/\sec \quad and \quad coefficient = 0,01$

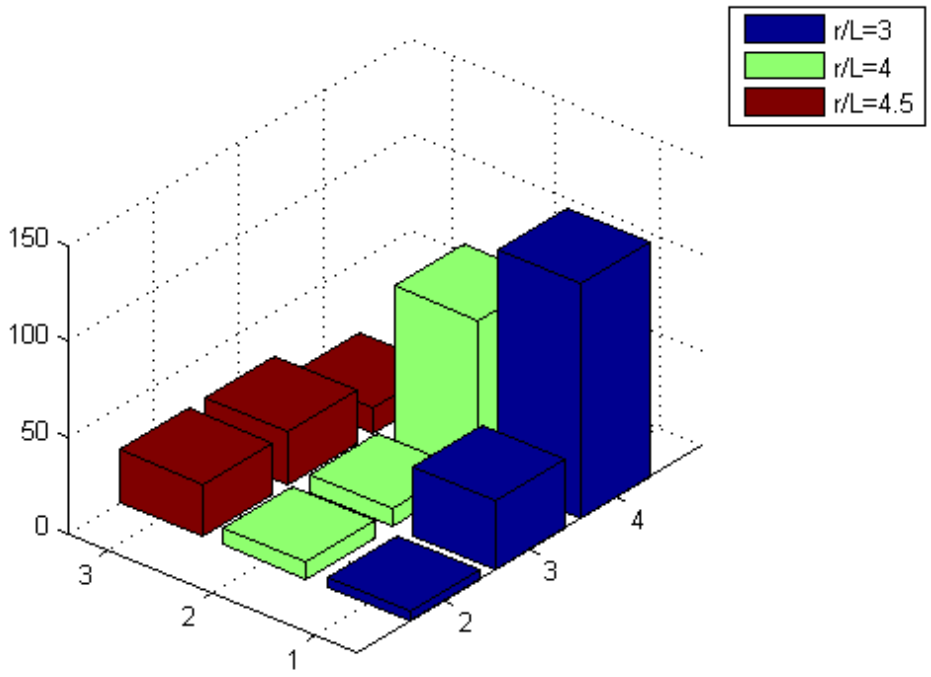

Figure 2.23:Error presentation for various values of the parameters.

5. $\omega = 2.3\, rad/\sec \quad and \quad coefficient = 0,015$

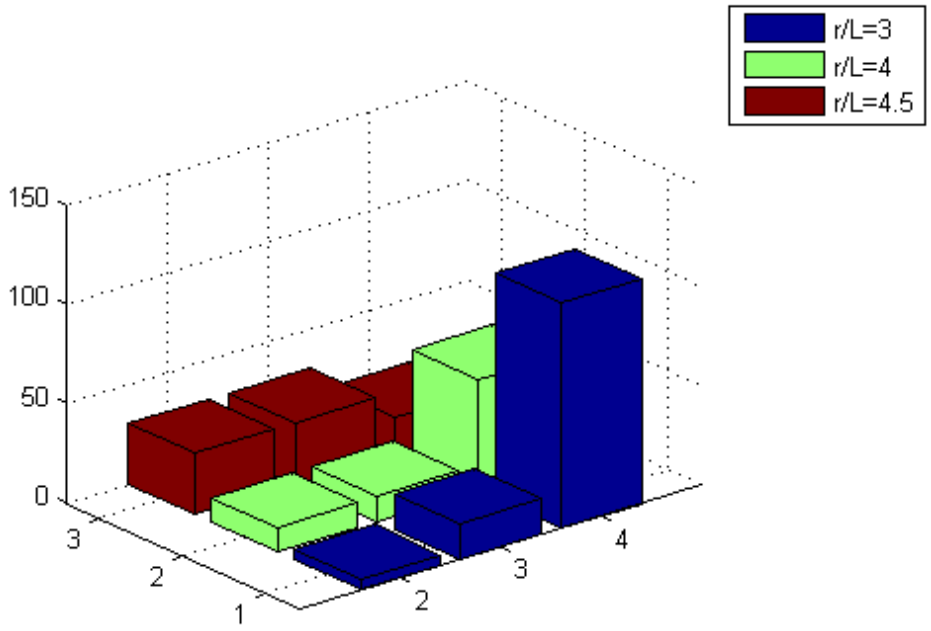

Figure 2.24:Error presentation for various values of the parameters.

6. $\omega = 2.3\, rad/\sec \quad and \quad coefficient = 0,02$

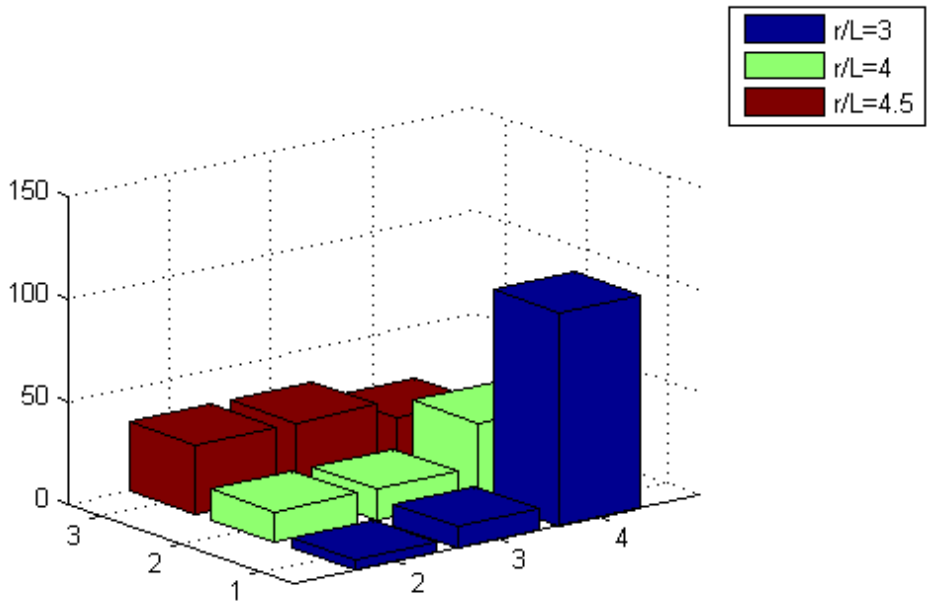

Figure 2.25:Error presentation for various values of the parameters.

7. $\omega = 5.3\, rad/\sec \quad and \quad coefficient = 0,01$

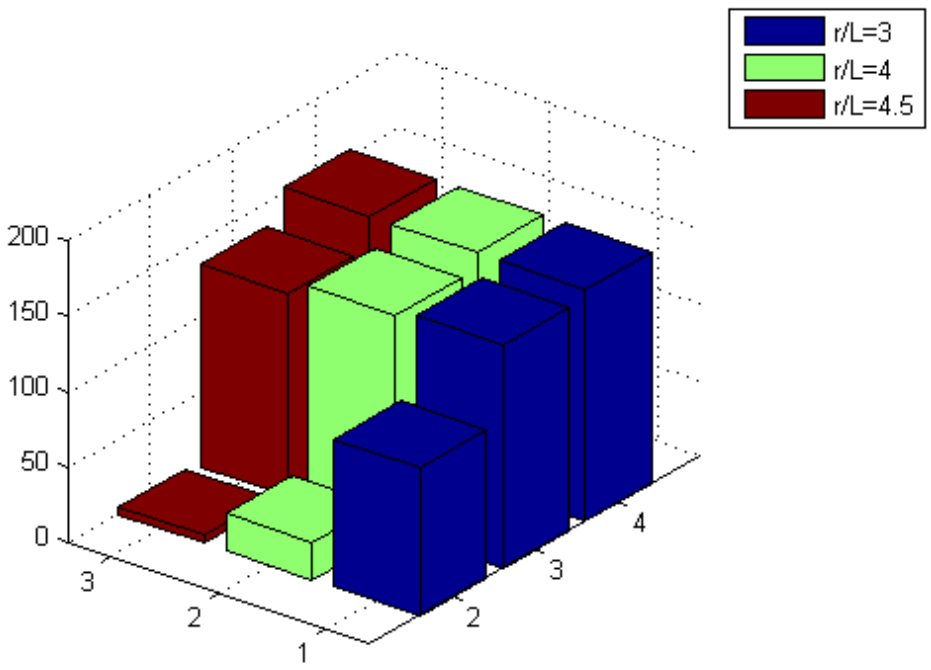

Figure 2.26:Error presentation for various values of the paramaeters.

8. $\omega = 5.3\, rad/\sec \quad and \quad coefficient = 0,015$

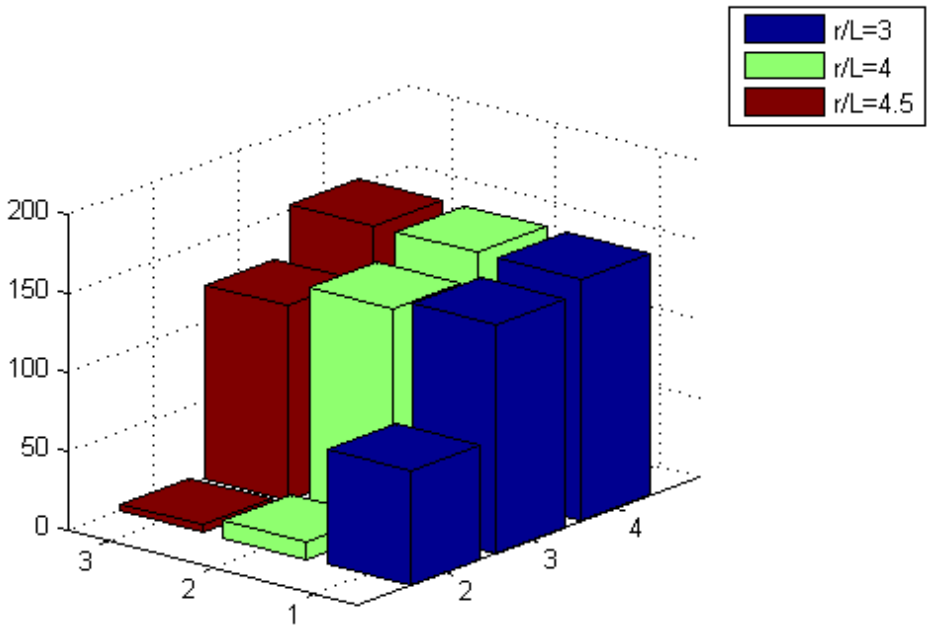

Figure 2.27: Error presentation for various values of the parameters.

9. $\omega = 5.3\, rad/\sec \quad and \quad coefficient = 0,02$

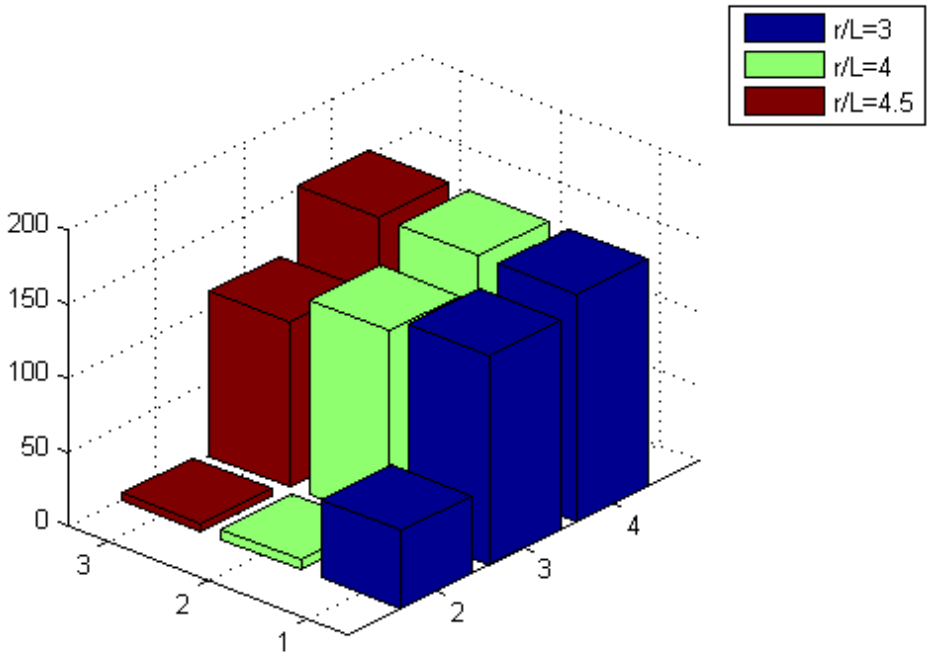

Figure 2.28:Error presentation for various values of the parameters.

These diagrams are presented in order to sort out which is the best combination for the absorbing layer. Hence, it will be used in the case of the 3d problem. At first glance, it is obvious that when the $n=2$ *and* $r/\lambda=3$ we have low error for low and intermediate frequencies , so the absorbing layer operates well for the specific combination, offering small error in relation with the analytic solution. On the other hand, the error is increased in the case of deep water . For high frequencies the parameter $r/\lambda=4-4$ .offer lower error than $r/\lambda=3$, in the same frequency. Generally, the absorbing layer substitutes well the radiation condition in low and intermediate frequencies, but in high frequencies is not strong enough to give the appropriate results.

Based on the above analysis we can conclude that an optimal version of the modified frequency parameter in the PML region is given by the following form

$$\mu(\omega)=\frac{1}{g}\left(\omega+i\,c(\omega)\left|x-x_0\right|^n\right)^2=\frac{\omega^2}{g}\left(1+i\frac{c(\omega)}{\omega}\left|x-x_0\right|^n\right)^2 \tag{2.49}$$

where the coefficient $c(\omega)$ is exponentially dependent to the frequency, taking higher values for higher frequency. We shall approximate this dependence in the following form

$$c=c_{\min}+\left(\frac{\omega}{\omega_{\max}}\right)^p \tag{2.50}$$

with appropriate (selected) values for $c_{\min}$, $\omega_{\max}$ and the exponent p. Specific values for the 3D problem concerning the diffraction and radiation problem of a 3D floating body in general bathymetry regions will be provided in the next Chapters.

Chapter 3

PML-BEM FOR 3D CYLINDER OVER FLAT BOTTOM

Summary

In this chapter, we first study the problem of a floating heaving circular cylinder in finite water depth and present the analytic solution. Subsequently, results concerning the added mass and damping coefficient and hydrodynamic forces are shown. In the next stage, a low-order Boundary Element Method is presented, based on an absorbing layer on the free surface, and applied to the hydrodynamic analysis of floating bodies over a flat horizontal bottom. Comparison of the results is presented against the analytical solution in the case of vertical cylinder, illustrating the convergence of the method, and the performance of absorbing layer technique. The latter, after validation and further optimization will be used in the next Chapter for the solution of the hydrodynamic problem of 3D bodies over general bathymetry region with different depths at infinity, where radiation conditions are not available.

3.1 Analytic solution of a vertical cylinder in finite-depth water

Due to the axi-symmetry of the geometry, both the dynamic equations and the radiation problem associated with the heaving motion, can be easily treated. This problem was studied extensively (see, e.g Young 1980, Calisal 1980, Bhatta et al 2011), since circular cylinders are common elements in floating offshore structures or in coastal and nearshore structures, used as breakwaters and port protection structures etc.

We proceed to the mathematical formulation of the problem. We consider a vertical cylinder with diameter *2a* and finite draft *T* heaving-harmonically in water of depth *h*, as it is shown in Fig.3.1. The bottom clearance is *d=h-T*. In the case of the symmetric heaving problem the cylinder response is independent of the incident wave angle, so without loss of generality, we choose the wave's direction to be parallel to the x_1 - axis.

In our case, from hydrostatic balance the mass of the body is equal to $M = \rho\pi\alpha^2 \mathrm{T}$ (ρ is water's density). Also, we consider that cylinder is upright and the center of gravity is located in the same vertical as the center of buoyancy.

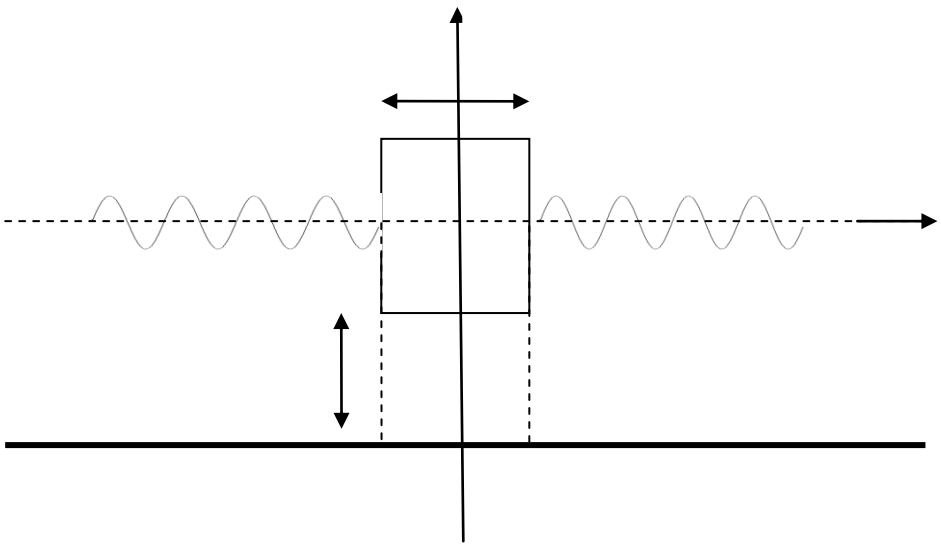

Figure 3.1: Vertical oscillation of a vertical cylinder.

So the involved added mass coefficients in heaving are $M_{33} = \mathrm{M}$, $M_{35} = J_1 = 0$ and the corresponding hydrostatic coefficients are $C_{33} = \rho g \pi \alpha^2$ and $C_{34} = C_{35} = 0$. Also, because of the body symmetry the radiation potentials $\Phi_1(x), \Phi_2(x), \Phi_4(x), \Phi_5(x)$ related with the moves $\xi_1, \xi_2, \xi_4, \xi_5$ (surge, sway, roll, pitch) are antisymmetric and their integration combined with the generalized normal vector corresponding component n_k to the body surface $x \in \partial D_B$, gives zero distribution. Consequently

$$\Pi_{l3} = \rho \iint_{\partial D_B} \Phi_l n_3 dS_B = 0, \quad l = 1,2,4,5 \ . \tag{3.1}$$

Furthermore, the radiation potential Φ_6 related with the move ξ_6 (yaw) is equal to zero, $\Phi_6(x) = 0$, since the generalized normal vector corresponding component resets $n_6 = 0$ at the submerged part of the body surface. From the above, results that only the added mass and damping matrix data (see below 3.3), which take part to vertical oscillation equation and are exclusively connected with the heave motion ξ_3, remain zero. Consequently, in heaving cylinders the dynamic equilibrium equation is simplified and takes the following form,

$$\left(-\omega^2 \left(\mathrm{M} + \mathrm{A}_{33}(\omega)\right) + i\omega \mathrm{B}_{33}(\omega) + C_{33}\right) \xi_3(\omega) = X_{03}(\omega) + X_{d3}(\omega), \tag{3.2}$$

where $X_{03}(\omega)$ and $X_{d3}(\omega)$ are the complex amplitude of the Froude-Krylov and diffraction

forces respectively. We recall that in case of existing other forces, they have to be added in the right part of the Eq. (3.2). Subsequently, we will present the application of the coupled mode method to define the potential $\Phi_3(x)$ through which the added mass's and damping coefficients can be evaluated by

$$A_{33}+\frac{1}{i\omega}\mathrm{B}_{33}=\rho\iint_{\partial D_B}\Phi_3 n_3 dS_B=\rho\int_{\theta=0}^{2\pi}d\theta\int_{r=0}^{r=a}r\,\Phi_3\left(r,x_3=-T\right)dr, \tag{3.3}$$

For the production of the right part, the property that the radiation potential Φ_3 is axisymmetric is used. Thus, Φ_3 and so independent from the azimuthal angle $\theta=\tan^{-1}\left(x_2/x_1\right)$ and therefore , $\Phi_3=\Phi_3\left(r,x_3\right)$,where $r=\sqrt{\left(x_1\right)^2+\left(x_2\right)^2}$ is the distance on the horizontal plane from the cylinder axis of symmetry. It is noteworthy that the Froude-Krylov forces are evaluated easily with direct integration of the incident wave potential over the submerged cylinder surface ∂D_B

$$\Phi_0(x)=\frac{gA}{\omega^2}\cdot\frac{\cosh\left[k_0\left(x_3+h\right)\right]}{\cosh k_0 h}\exp\left[ik_0x_1\right],\ \text{where}\ \omega^2=gk_0\tanh\left(k_0h\right), \tag{3.4}$$

and *A* the wave elevation amplitude on the free surface. Taking into consideration that $n_3=0$ on the vertical part of the wetted cylinder surface and $n_3=1$ on the cylinder bottom $\left(x_3=-T\right)$, in the present case Froude-Krylov forces are given by the following equation,

$$X_{03}=\rho\omega^2A\iint_{\partial D_B}\Phi_0 n_3 dS_B=\rho\omega^2A\int_{\theta=0}^{2\pi}d\theta\int_{r=0}^{r=a}r\,\Phi_0\left(r,x_3=-T\right)dr, \tag{3.5}$$

and they are evaluated analytically below.

The determination of the diffraction potential $\Phi_d(x)$, through which the respective diffraction forces can be evaluated,

$$X_{d3}=\rho\omega^2A\iint_{\partial D_B}\Phi_d\,n_3dS_B \tag{3.6}$$

presents some difficulties, due to the fact that the field is not axisymmetric and it depends on the three space dimensions. Nevertheless, the coupled mode method can be applied and in this case and provides solution for the problem. The reader is referred to the related works of Black, Mei & Bray (1971) and Garret (1971), where are presented details for the application of this method to the specific problem.

It is known that the total hydrodynamic forces can be evaluated by the application of the Haskind-Newman equations via $\Phi_3\left(r,x_3\right)$. Also, the force amplitude can be evaluated by the damping coefficient B_{33}, which is based only on the radiation potential $\Phi_3\left(r,x_3\right)$. The application of these equations is useful, because it allows us to avoid the diffraction potential

determination, when we examine the cylinder responses and it will be presented in detail below.

3.2 Evaluation of the cylinder radiation potential $\Phi_3(x)$

The coupled mode method, that will be presented here for the solving of the radiation problem for the cylinder vertical oscillation, constitutes a general method for solving and simulating problems of wave propagation , which is used in many applications beyond the region of the hydrodynamics of a floating body , such as the free surface wave's propagation over a variable bathymetry, propagation and scattering of acoustic waves in the sea environment and also in more general problems of wave propagation.

With the help of interfaces, that are shown with dashed lines in Fig.3.1, the total flow domain $D = D_e \bigcup D_i$ is separated in 2 regions, the interior domain below the cylinder D_i and the exterior cylindrical domain D_e. The interface in present case is the vertical cylindrical surface at $r = \sqrt{(x_1)^2 + (x_2)^2} = a$, $-h < x_3 < -T$.

Exterior domain: The representation of the solution of the radiation problem in the exterior region D_e is provided by the general representation theorem (Athanassoulis & Belibassakis 2012), taking into consideration the appropriate behavior requirements of the field to the infinity $(r \to \infty)$, which must have the form of outgoing waves that are also decaying as propagating to infinity due to the fact that the same energy is propagating through cylindrical surfaces that are constantly growing. In this case the field is axisymmetric and so independent by the azimuth angle. Therefore, all of the terms including trigonometric functions except of the first $(m = 0)$ zero, and we receive

$$\Phi_3^{(e)}(r, x_3) = a_0 H_0^{(1)}(k_0 r) Z_0^{(e)}(x_3) + \sum_{n=1}^{\infty} a_n K_0(k_n r) Z_n^{(e)}(x_3) \ , r \geq a \ , \ -h < x_3 < -T \ , \tag{3.7}$$

where

$$Z_0^{(e)}(x_3) = \cosh\left[k_0(x_3 + h)\right] / N_0^{1/2} \quad \text{and} \quad Z_n^{(e)}(x_3) = \cos\left[k_n(x_3 + h)\right] / N_n^{1/2}, \ n = 1, 2\ldots, \tag{3.8}$$

$$N_0 = \frac{1}{2}\left(1 + \frac{\sinh k_0 h}{2k_0 h}\right) , \qquad N_n = \frac{1}{2}\left(1 + \frac{\sinh k_n h}{2k_n h}\right), \quad n = 1, 2, 3\ldots, \tag{3.9}$$

and the $k_0, k_n, \ n = 1, 2\ldots,$ arising as solutions of the dispersive relation (see also Eq.2.6)

$$\mu h = k_0 h \tanh(k_0 h) \text{ and } \mu h = -k_n h \tanh(k_n h), \qquad n = 1, 2\ldots \tag{3.10}$$

In the last equation $\mu = \omega^2 / g$ is the problem frequency parameter. We remind here that the above representations are constructed with the application of the separation of variables method in Laplace equation in regions with horizontal boundaries and in the problem boundary conditions. The complex coefficients $\{a_n, n = 0,1,2\ldots\}$ are the problem unknowns in the exterior region D_e.

Interior domain: The potential in the interior region D_i below of the cylinder, satisfies the Laplace equation

$$\Delta\Phi_3 \equiv \frac{1}{r}\cdot\frac{\partial}{\partial r}\left(r\frac{\partial\Phi_3}{\partial r}\right)+\frac{\partial^2\Phi}{\partial x_3^2}=0\,, \tag{3.11}$$

where the field axisymmetric property has been used ($\frac{\partial\Phi_3}{\partial\theta}=0$), and in addition, the homogenous equation to the bottom,

$$\frac{\partial\Phi_3}{\partial n}=-\Phi_{,x_3}=0\,,\qquad x_3=-h\,, \tag{3.12}$$

and the inhomogeneous equation on the bottom of the cylinder

$$\frac{\partial\Phi}{\partial n}\equiv\Phi_{,x_3}=n_3=1\,,\qquad x_3=-T\,, \tag{3.13}$$

which constitutes the forcing condition of the problem. The general solution of the above problem is composed by a particular solution of the inhomogeneous problem, $\Phi_3^{\mathrm{NH}}(r,x_3)$, and the general solution of the corresponding homogenous problem, $\Phi_3^{\mathrm{H}}(r,x_3)$, as follows

$$\Phi_3(r,x_3)=\Phi_3^{NH}(r,x_3)+\Phi_3^{\mathrm{H}}(r,x_3). \tag{3.14}$$

A simple form for the particular solution of the inhomogeneous problem is the following

$$\Phi_3^{NH}(r,x_3)=\frac{1}{2d}\left((x_3+h)^2-\frac{r^2}{2}\right), \tag{3.15}$$

which, as it is easily noted, satisfies all the above equations. The general representation of the homogeneous problem solution in the interior region D_i below of the cylinder, can be constructed with the method of separation of variables in the region D_i and has the following form,

$$\Phi_3^{H}(r,x_3)=\sum_{n=0}^{\infty}b_nI_0(\lambda_n r)\cos(\lambda_n x_3)\ ,\qquad \lambda_n=\frac{n\pi}{d},\ \ n=0,1,2,\ldots \tag{3.16}$$

Therefore, the general representation of the potential $\Phi_3(r,x_3)$, in the interior region D_i is written as follows

$$\Phi_3^{(i)}(r,x_3)=\frac{1}{2d}\left((x_3+h)^2-\frac{r^2}{2}\right)+\sum_{n=0}^{\infty}b_nI_0(\lambda_n r)Z_n^{(i)}(\lambda_n x_3),\ \text{with}\ Z_n^{(i)}(x_3)=\cos(\lambda_n x_3) \tag{3.17}$$

where, the coefficients $\{b_n,\ n=0,1,2\ldots\}$ constitute the problem complex unknowns in D_i. With the above representations (3.7) and (3.17) all requirements of the problem have been satisfied, except from

1. The satisfaction of the boundary condition on vertical cylinder (wetted) surface

$$\frac{\partial\Phi}{\partial n}\equiv-\Phi_{,r}^{(e)}=0\,,\qquad r=a\,,\quad -T<x_3<0\,, \tag{3.18}$$

and

2. The matching of the representations on the common interface, which requires the continuity of the potential and its first derivative:

$$\Phi_{,r}^{(i)}=\Phi_{,r}^{(e)}\ \text{ and }\ \Phi_{,r}^{(i)}=\Phi_{,r}^{(e)}\ ,\quad r=a\,,\ -h<x_3<-T\ , \tag{3.19}$$

With the application of the coupled mode method, the property of the set of the eigenfunctions $\left\{Z_n^{(e)}\left(x_3\right),\ n=0,1,2\ldots\right\}$ and $\left\{Z_n^{(i)}\left(x_3\right),\ n=0,1,2\ldots\right\}$ to be an orthogonal basis (which can be easily normalized) is exploited. Thus, the latter constitute a complete set of functions in the space of squared integrable functions $f\left(x_3\right)$ defined in the intervals $-d<x_3<0$ and $-h<x_3<-T$, respectively. So, Eqs. (3.18) and the first of Eqs. (3.19) that regard to the horizontal derivative can be equivalently satisfied with their projection to the vertical basis $\left\{Z_k^{(e)}\left(x_3\right),k=0,1,2\ldots\right\}$:

$$\int_{x_3=-h}^{x_3=-T}\left(\Phi_{,r}^{(i)}\left(r=a,x_3;\{a_n\}\right)-\Phi_{,r}^{(e)}\left(r=a,x_3;\{b_n\}\right)\right)Z_k^{(e)}\left(x_3\right)dx_3$$

$$-\int_{x_3=-T}^{x_3=0}\Phi_{,r}^{(e)}\left(r=a,x_3;\{b_n\}\right)Z_k^{(e)}\left(x_3\right)dx_3=0\ ,\quad k=0,1,2,\ldots, \tag{3.20}$$

and the second from Eqs. (3.19) , which regards the continuity of the field values on the interface from the projection to the vertical basis $\left\{Z_k^{(i)}\left(x_3\right),k=0,1,2,\ldots\right\}$:

$$\int_{x_3=-h}^{x_3=-T}\left(\Phi^{(i)}\left(r=a,x_3;\{a_n\}\right)-\Phi^{(e)}\left(r=a,x_3;\{b_n\}\right)\right)Z_k^{(i)}\left(x_3\right)dx_3=0\ ,\ k=0,1,2,\ldots \tag{3.21}$$

Substituting Eqs. (3.7) and (3.17) to the above equations and integrating with respect to x_3, (which is analytically obtained), leads to a system solving for the unknown coefficients

$\{a_n,\ n=0,1,2\ldots\}$ and $\{b_n,\ n=0,1,2\ldots\}$. Coefficients $\{b_n,\ n=0,1,2\ldots\}$ are obtained from the solution of the linear system (see for details Yeung 1980)

$$b_n-\sum_{j=0}^{\infty}e_{nj}b_j=g_n,\qquad \text{for}\quad n=0,1,\ldots, \tag{3.22}$$

$$e_{nj}=\left[\sum_{k=0}^{\infty}\frac{C_{nk}C_{jk}}{m_k}\left(\frac{R_k}{R_k^{'}}\right)\right]S_j, \tag{3.23}$$

$$g_n=\sum_{k=0}^{\infty}\frac{C_{nk}}{m_k}\left(\frac{R_k}{R_k^{'}}\right)A_k^*-b_n^*, \tag{3.24}$$

where m_k are solutions of the equations

$$m\tanh m=v \tag{3.25}$$

Where m represents m_0 or im_k for $k\geq 1$

$$A_k^*=\int_0^d\frac{\partial}{\partial r}\Phi_3^{NH}\left(r,x_3\right)Z_k^{(i)}\left(x_3\right)dx_3, \tag{3.26}$$

$$b_n^*=\frac{2}{d}\int_0^d\Phi_3^{NH}\left(r,x_3\right)\cos\left(\lambda_n x_3\right)dx_3, \tag{3.27}$$

$$b_n=\sum_{k=0}^{\infty}R_kC_{nk}A_k+b_n^*\qquad n=0,1,2 \tag{3.28}$$

$$A_k=\left(\sum_{n=0}^{\infty}S_nC_{nk}b_n+A_k^*\right)/m_kR_k^{'}\ , \tag{3.29}$$

$$R_k\left(m_kr\right)=\begin{cases}H_0^{(1)}\left(m_0r\right) & for\ k=0\\ K_0\left(m_kr\right) & for\ k\geq 1\end{cases}, \tag{3.30}$$

And the coupling integrals C_{nk} are defined by:

$$C_{nk}=\frac{2}{d}\int_0^d\cos\left(\lambda_n x_3\right)Z_k\left(m_kx_3\right)dx_3\quad\begin{matrix}n=0,1,\ldots\\ k=0,1,\ldots\end{matrix}, \tag{3.31}$$

$$=\begin{cases}\dfrac{2(-)^n\sinh\left(m_0d\right)/\left(m_0d\right)}{\left[1+\left(\dfrac{\lambda_n}{m_0}\right)^2\right]N_0^{1/2}} & for\ k=0\\ \dfrac{2\sin\left(m_kd-n\pi\right)}{\left(m_kd-n\pi\right)}-\dfrac{m_kd}{\left(m_kd+n\pi\right)} & for\ k=1,2,\ldots\end{cases}$$

The quantity S_n occurring in Eq.(3. is defined by:

$$S_n=\frac{n\pi}{2}I_0^{'}\left(\lambda_na\right)/I_0\left(\lambda_na\right), \tag{3.32}$$

Practically, the infinite series, that are involved in the representations (3.7) and (3.17) , are simplified keeping only the first K terms. Consequently, the above equations end up finally to a system of 2K equations with 2K unknowns, which can be solved numerically by known methods. The infinite series simplification combined with the fast convergence, introduce an error, that languishes quickly as K is increased. It is noteworthy that the simplification of the infinite series combined with the orthogonal projections of the equations (3.18) and (3.19) to the corresponding basis constitute an application of the general Galerkin method, in the case of the problem we study.

After finding the coefficients of the series, the hydrodynamic coefficients can be evaluated by Eq. (3.3) , where obviously for the radiation potential applies that

$$\Phi_3\left(r, x_3 = -T\right) = \Phi_3^{(i)}\left(r, x_3 = -T; \{b_n\}\right). \tag{3.33}$$

3.3 Evaluation of the hydrodynamic coefficients

Using the indefinite integral $\int xI_0(x)dx = xI_1(x)$, the final result for the hydrodynamic coefficients, related with the cylinder vertical oscillation results in non-dimensionalized form, as follows

$$\hat{A}_{33} - i\hat{B}_{33} = \frac{A_{33} - (i/\omega)B_{33}}{\rho\pi a^3} = 2\left(\frac{1}{4}\frac{d}{a} - \frac{1}{16}\frac{a}{d} + \frac{\Lambda}{a}\right) \tag{3.34}$$

where,

$$\Lambda = \frac{b_0}{2} + \frac{d}{a}\sum_{n=1}^{\infty}(-1)^2 b_n \frac{I_1(\lambda_n a)}{n\pi}, \quad n = 1, 2, \ldots \tag{3.35}$$

We quote below indicative results in Figs. 3.2 and 3.3.

Especially, in Fig. 3.2. are presented the non-dimensionalized damping and added mass coefficients for radius to water depth ratio $a/h = 0.5$ and for several values of the bottom clearance to water depth ratio $d/h = 0.1$, 0.25, 0.75, 0.9 and 0.99. Also, in fig. 3.2 are presented corresponding results for $a/h = 0.2$. The infinite series are deducted for the results, using K=5 terms. As well it is noticed that from the presented method we can take estimation for many units and for the deep water case. Practically, is enough to set for the tested frequency, a finite depth, that will be much bigger than the maximum of α, T and $\lambda = 2\pi / k_0$.

An other case of hydrodynamic coefficients evaluation, that we will work out later for the hydrodynamic forces and responses estimation is presented in Fig. 3.3 and 3.4. In this case the

cylinder radius is $a = 0.35m$ and the draft $T = 0.63m$ and so the volume is $\nabla = 0.242m^3$. The water depth is $h = 3m$ and therefore the ratios $a/h = 0.116$ and $d/h = 0.79$.

The results that regard the (non-dimensionalized) hydrodynamic coefficients for several values of the non-dimensionalized wave number $k_0 a = 2\pi a/\lambda$ are presented in this case in Fig.3.3. Respectively, in Fig.3.4 the hydrodynamic coefficients are presented in the same as the previous case, for various values of the non-dimensionalized frequency $\omega\sqrt{a/g}$. Here we use a different normalization and we present the units A_{33}/M and $2\pi B_{33}/(M\omega)$, in order to show the importance of these units related to the cylinder's mass.

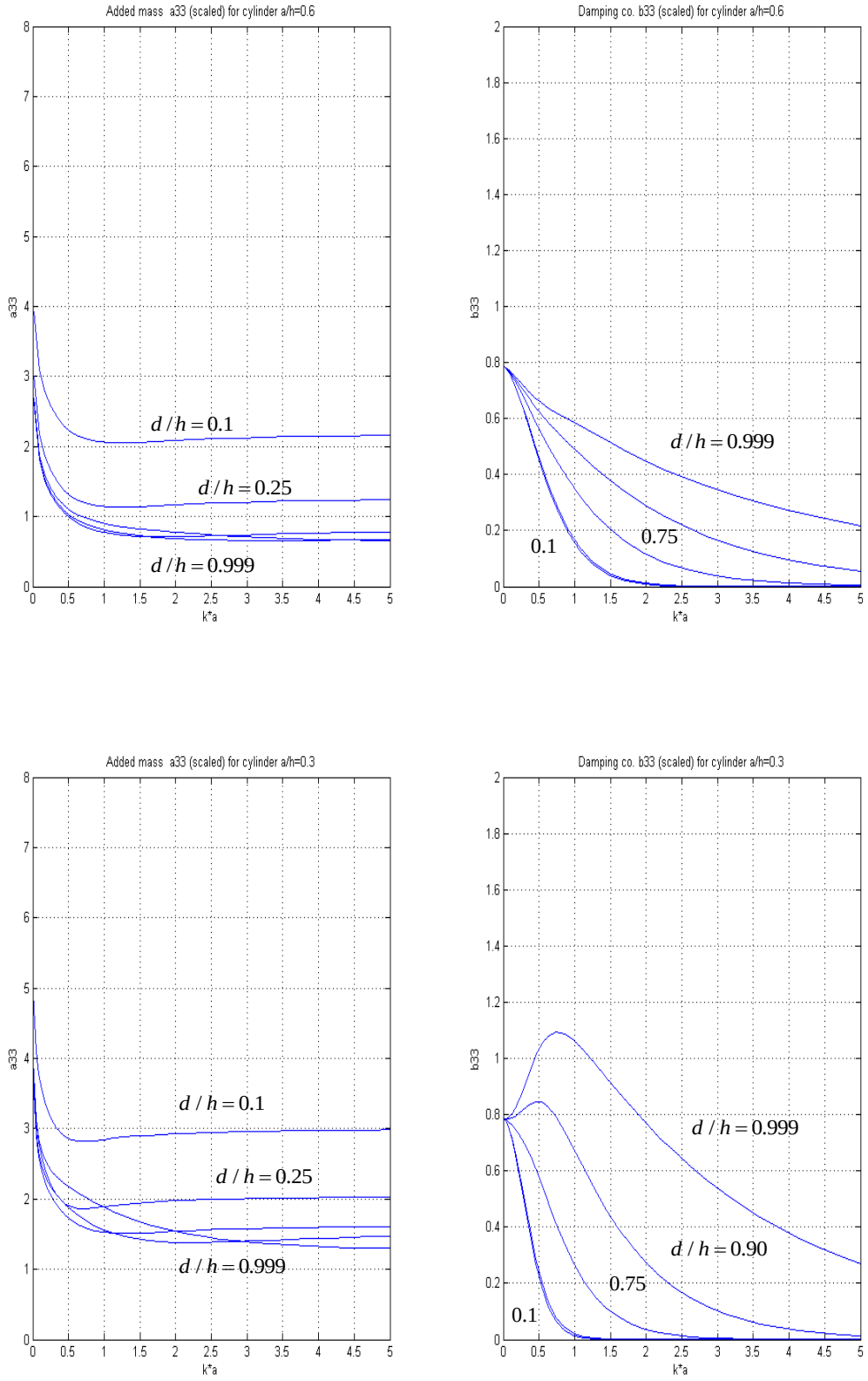

Figure 3.2: Non-dimensionalized hydrodynamic coefficients of a cylinder in vertical oscillation for $a/h = 0.5\,0.6$ and $a/h = 0.2\ 0.3$ and various values of the bottom clearance to water depth ratio $d/h = 0.1$, 0.25, 0.75, 0.9 and 0.99. The results are presented for various values of the non-dimensionalized wave number $k_0 a = 2\pi a/\lambda$.

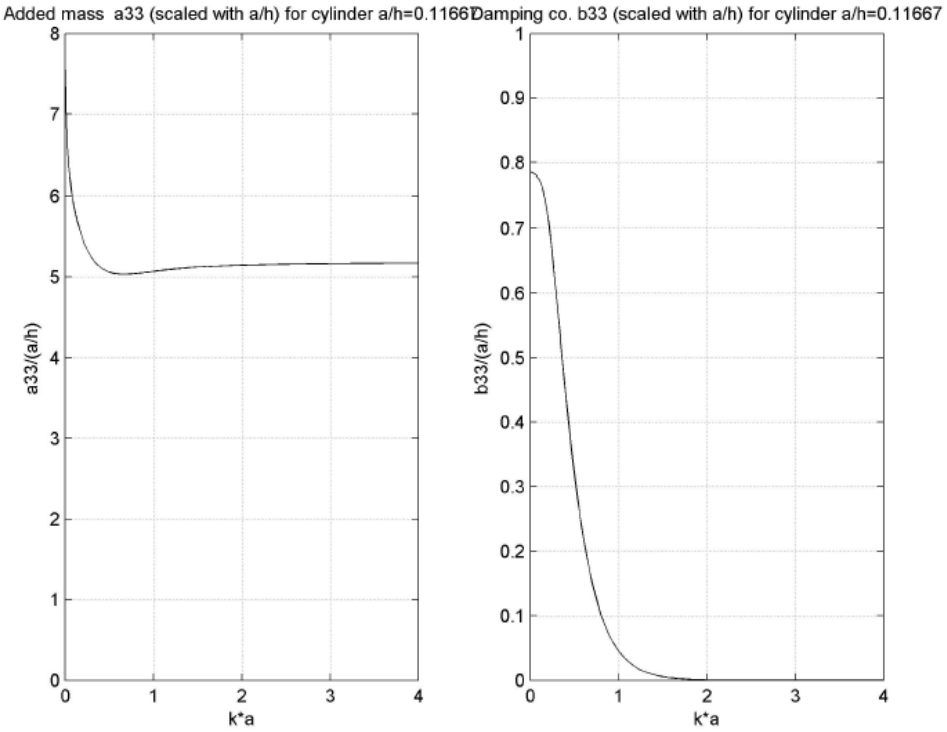

Figure 3.3: Non-dimensionalized cylinder hydrodynamic coefficients for $a/h = 0.116$ and $d/h = 0.79$, for various values of the non dimensionalized wavenumber $k_0 a = 2\pi a/\lambda$.

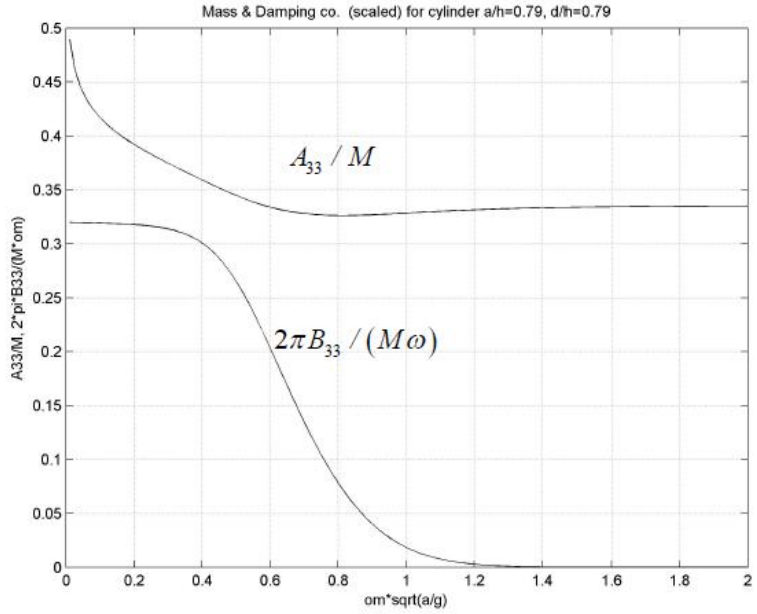

Figure 3.4: Non-dimensionalized cylinder hydrodynamic coefficients for $a/h = 0.116$ and $d/h = 0.79$, for various values of the non dimensionalized frequency $\omega\sqrt{a/g}$.

3.4 Evaluation of the Froude-Krylov's forces $\mathrm{X}_{03}(\omega)$ in the vertical direction

Substituting the results Eq. (3.4) in the Eq. (3.5) and taking into consideration the below analytic expression of the function $\exp(-ikx_1)$

$$\exp(-ikx_1) = \sum_{m=0}^{\infty} e_m (-i)^m J_m(k_0 r)\cos m\theta, \tag{3.36}$$

with $e_m = 1$, for m=1 and , $e_m = 2$ for $m = 2,3,\ldots,$ we obtain

$$X_{03} = \rho\omega^2 A \frac{g}{\omega^2} \cdot \frac{\cosh k_0 d}{\cosh k_0 h} \int_{\theta=0}^{2\pi} d\theta \int_{r=0}^{r=a} r \sum_{m=0}^{\infty} e_m (-i)^m J_m(k_0 r)\cos m\theta \, dr \tag{3.37}$$

From the sum's terms in the integrated part, because of the integration of θ, only the term m=0 has non zero contribution, and so

$$X_{03} = 2\pi\rho g A \frac{\cosh k_0 d}{\cosh k_0 h} \int_{r=0}^{r=a} r\, J_0(k_0 r)\, dr = 2\pi\rho g A \frac{\cosh k_0 d}{\cosh k_0 h} \frac{k_0 a}{k_0^2} J_1(k_0 a) \tag{3.38}$$

where the indefinite integral was used $\int x J_0(x) dx = x J_1(x)$. The final result is presented in a non-dimensionalized form, as follows

$$\widehat{X}_{03} = \frac{X_{03}}{\rho g \pi a^2 A} = \frac{2}{k_0 a} \frac{\cosh k_0 d}{\cosh k_0 h} J_1(k_0 a) \tag{3.39}$$

From the equation above, we conclude that in our case the Froude-Krylov forces have zero phase difference concerning the incident's wave elevation in the cylinder centre *r=0*, as a consequence of body's symmetry. Also, for very slow motion, to wit ω and $k_0 a \to 0$, these forces tend to the hydrostatic added force due to the wave's elevation $\widehat{X}_{03} \to 1$, as it is naturally expected. In the end, for a very fast oscillation, to wit ω and $k_0 a \to \infty$ these forces tend to zero.

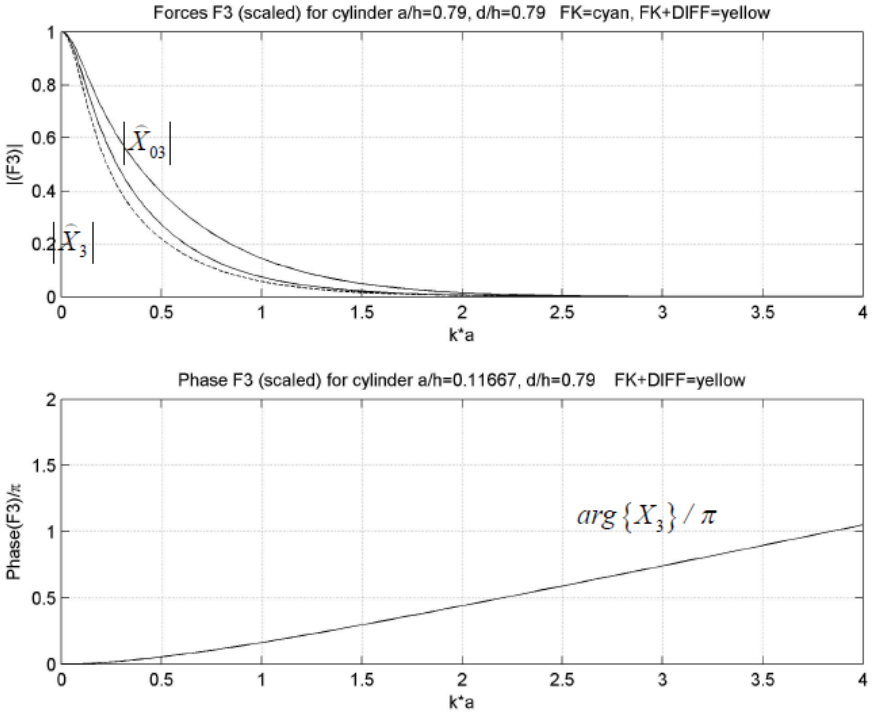

Figure 3.5: Amplitude and Phase of Cylinder hydrodynamic forces for $a/h=0.116$ and $d/h=0.79$, for various values of the non dimensionalized wavenumber $k_0 a = 2\pi a/\lambda$.

This is explained naturally due to the fact that as the frequency increases, the wave length tends to zero, so the contribution of many wave lengths in the pressure forces on cylinder bottom are mutually reversed. Numerical results in cylinder case with $a/h=0.116$ and $d/h=0.79$ are presented in Fig.3.5 , where it is observed a good accordance with the above asymptotic behavior.

3.5 Evaluation of total hydrodynamic forces

According to previous Section results, the aggregate hydrodynamic force $X_3(\omega)=X_{03}(\omega)+X_{d3}(\omega)$ can be evaluated by integration of the incident wave and radiation potential to the circular cylinder collateral surface ∂D_R^* for quite big radius $R\to\infty$, as follows

$$X_3=-\rho\omega^2 A\iint_{\partial D_R^*}\left(\Phi_0\frac{\partial\Phi_3}{\partial R}-\Phi_3\frac{\partial\Phi_0}{\partial R}\right)dS_B=-\rho\omega^2 A\int_{x_3=-h}^{x_3=0}dx_3\int_{\theta=0}^{\theta=2\pi}d\theta\,R\,\mathrm{E}(R,\theta,x_3)\,, \tag{3.40}$$

where $E(r=R,\theta,x_3)=\left(\Phi_0\frac{\partial\Phi_3}{\partial R}-\Phi_3\frac{\partial\Phi_0}{\partial R}\right)_{\partial D_R^*}$. According to the previous Eq. (3.36), the incident wave potential is written in the form

$$\Phi_0\left(r=R,\theta,x_3\right)=\frac{g}{\omega^2}\frac{\cosh\left[k_0\left(x_3+h\right)\right]}{\cosh k_0 h}\sum_{m=0}^{\infty}e_m\left(-i\right)^m J_m\left(k_0R\right)\cos m\theta \tag{3.41}$$

After substitution of the radiation potential $\Phi_3^{(e)}\left(r,x_3\right)$ in the exterior region D_e and taking into consideration that

(i) The functions $K_0\left(k_n r\right)$ decay exponentially in large distances and can be omitted for $R\to\infty$ and

(ii) The terms that include $\cos m\theta$, $m=1,2,3\ldots$ are zero during the θ-integration

the totalhydrodynamic force becomes

$$X_3=\int_{x_3=-h}^{x_3=0}\frac{\cosh^2\left[k_0\left(x_3+h\right)\right]}{N_0^{1/2}\cosh k_0 h}dx_3\int_{\theta=0}^{\theta=2\pi}rd\theta\left(J_0\left(k_0R\right)\frac{\partial H_0^{(2)}\left(k_0R\right)}{\partial R}-H_0^{(2)}\left(k_0R\right)\frac{\partial J_0\left(k_0R\right)}{\partial R}\right), \tag{3.42}$$

where we recall that $N_0=\frac{1}{2}\left(1+\frac{\sinh k_0 h}{2k_0 h}\right)$. The vertical integral in the last equation is evaluated analytically as follows

$$\int_{x_3=-h}^{x_3=0}\frac{\cosh^2\left[k_0\left(x_3+h\right)\right]}{N_0^{1/2}\cosh k_0 h}dx_3=\frac{hN_0^{1/2}}{\cosh k_0 h}\ . \tag{3.43}$$

Furthermore, the part in the bracket of the *r*-integration is easily noted that it is equal to

$$jk_0\left(Y_0\left(k_0R\right)J_1\left(k_0R\right)-J_0\left(k_0R\right)Y_1\left(k_0R\right)\right)=\frac{2i}{\pi R}\ , \tag{3.44}$$

As it is calculated by the determinant Wronski of the functions $J_0\left(k_0R\right)$ and $Y_0\left(k_0R\right)$. With substitution all of the above results to equation (3.31) finally we take

$$\widehat{X}_3=\frac{X_3}{\rho g\pi a^2 A}=\frac{4i}{\pi}\frac{a_0}{\left(a/h\right)^2}\frac{N_0^{1/2}}{\cosh k_0 h}\ , \tag{3.45}$$

Where we recall that a_0 is the first coefficient of the exterior potential series $\Phi_3^{(e)}\left(r,x_3\right)$, and so it depends on the problem's frequency and the non-dimensionalize $\rho g\pi a^2 A$ corresponds to the added hydrostatic forces due to the incident wave's amplitude A.

In the case of vertical oscillating cylinder, the aggregate forces tend to the value of Froude-Krylov's forces for ω and $k_0 a \to 0$, that is due to the diffraction potential is negligible while the body moves very slow. Also, for the same reasons as in the Froude –Krylov forces case , as the frequency increases and wave length tend to zero, the contribution of the pressure forces to the cylinder's bottom is reversed due to the big number of wave lengths and so $X_3 \to 0$, for $k_0 a \to \infty$.

In addition to the Froude-Krylov forces , that in the case of the vertical oscillating cylinder present zero phase difference from the incident wave's elevation in cylinder's center $r = 0$ (for every frequency's value), the aggregate forces present non-zero phase difference, which for low frequency tend to zero and for high frequency shows asymptotic behavior:

$\arg\{X_3\} \to ka - \pi/4$, for $k_0 a \to \infty$

The application results of the final above equation in our example, for the case of the floating cylinder $a/h = 0.116$ and $d/h = 0.79$, are presented, also, in fig. 3.5 , that we conclude full accordance with the above predictions for the asymptotic behavior.

Finally, we recognize that the aggregate force amplitude can be evaluated alternatively via the problem Kochin function . The Kochin function is connected with the damping coefficients, that for the studied case we take

$$|H_3|^2 = \frac{2k_0 B_{33}}{\rho\omega D(k_0 h)}\ , \tag{3.46}$$

Where due to the axisymmetry, the Kochin function is independent from the azimuth angle (θ). Finally we take :

$$|\hat{X}_3| = \frac{|X_3|}{\rho g \pi a^2 A} = \sqrt{\frac{2\left[\tanh(k_0 h) + k_0 h\left(1 - \tanh^2(k_0 h)\right)\right] B_{33}}{\pi k_0 a}}\ . \tag{3.47}$$

Numerical results for the case of the cylinder $a/h = 0.116$ and $d/h = 0.79$ are presented in fig.3.5 (with dashed line). We observe a quite well accordance in our calculations, related with the aggregate hydrodynamic force amplitude from the application of the equations (3.34) and (3.37) . The little presented differences are due to the solution numerical approximation, keeping only a few terms(we recall that we have taken $K = 5$), both of the predictions tend to coincide, as K is increased.

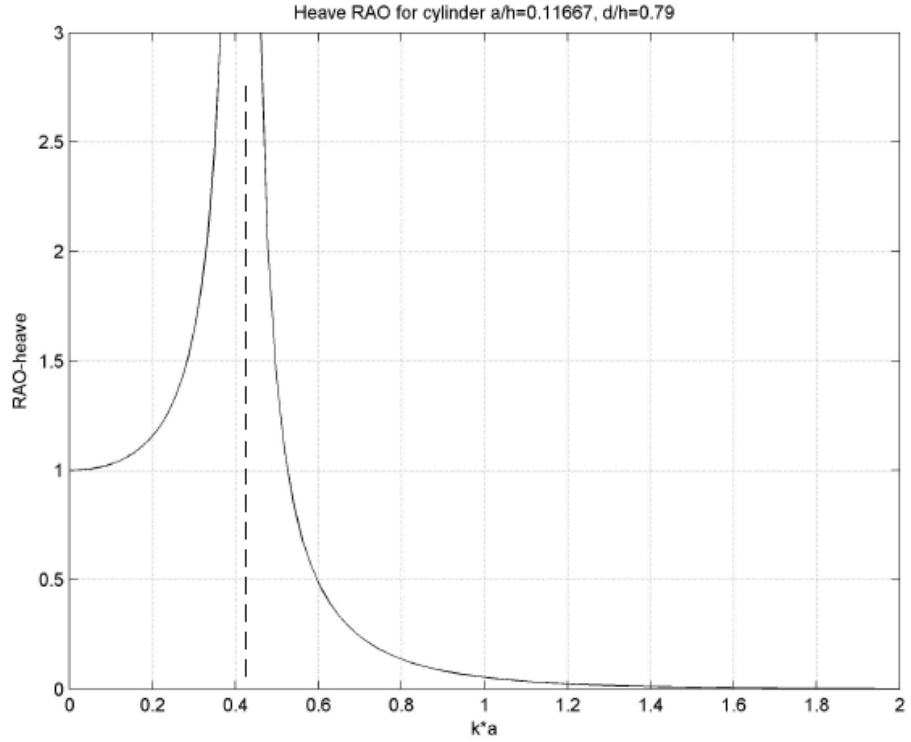

Figure 3.6: Response Amplitude Operator of Cylinder for $a/h = 0.116$ and $d/h = 0.79$, for various values of the non dimensionalized wavenumber $k_0 a = 2\pi a/\lambda$.

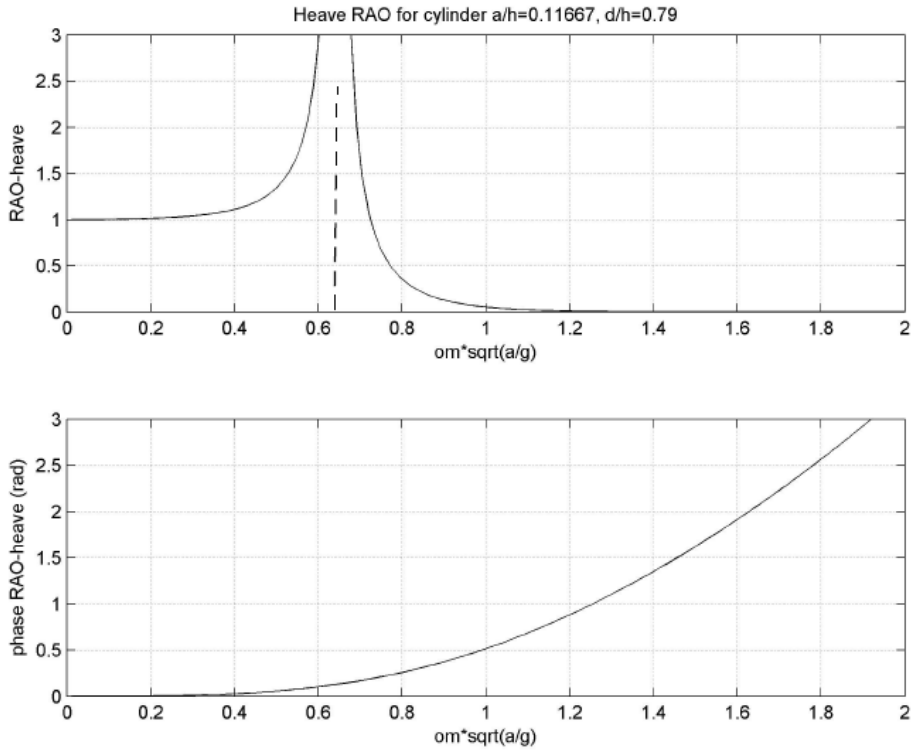

Figure 3.7: Heave Response Amplitude Operator and Phase of Cylinder with $a/h = 0.116$ and $d/h = 0.79$, for various values of the non dimensionalized frequency $\omega\sqrt{a/g}$.

3.6 Evaluation of the response of the floating cylinder in vertical oscillation.

Based on all previous, the complex measure of the response of the vertical oscillating cylinder is calculated with substitution of the various quantities to the equation (3.2), and in non-dimensionalized form(related to the free surface's elevation measure of the incident wave) is

$$\frac{\xi_3(\omega)}{A} = RAO_{heave}(\omega) = \frac{1}{A}\frac{X_{03}(\omega) + X_{d3}(\omega)}{\left(-\omega^2\left(M + A_{33}(\omega)\right) + i\omega B_{33}(\omega) + C_{33}\right)} \quad . \tag{3.48}$$

Numerical results for the case of the cylinder with $a/h = 0.116$ and $d/h = 0.79$ are presented in Fig.3.6 , for various values of the non-dimensionalized wavenumber $k_0 a = 2\pi a/\lambda$ and in Fig.3.7, respectively, for several values of the non-dimensionalized frequency $\omega\sqrt{a/g}$. In these figures is illustrated with dashed line the resonance location of the vertical oscillating cylinder.

Specifically, in the above figures we observe that in low frequency the cylinder is oscillating hydrostatically, watching the wave vertical elevation, with the same phase $\left(\xi_3(\omega)/\mathrm{A} \to 1,\ \omega \to 0\right)$, as it is physically expected. Otherwise, as the frequency is being increased well above from the resonance value, the cylinder vertical oscillation is languishing continually and the phase difference between the move and the wave elevation is being increased continually.

3.7 3D – Boundary Element Method

In this section a 3D - Boundary Element Method is applied to evaluate the diffraction and radiation potentials $\Phi_D(x,z)$ and $\Phi_k(x,z)$, associated with the operation of a floating cylinder oscillating on the water's free surface, over a horizontal seabed. The latter BEM is a low-order method, based on piecewise constant normal-dipole singularity distributions and 4-node quadrilateral boundary elements ensuring continuity of the geometry approximation of the various part of the boundary, as described in detail in Appendix A. In this section the BEM is applied in constant depth regions and the bottom boundary condition is satisfied by simple mirroring techniques, as described below. We use this version of the BEM, in order to test and optimize the absorbing layer method similarly as in the 2D problem examined in the previous chapter, which is used to replace the radiation condition. The optimum set up will be subsequently used in the next Chapter to study diffraction radiation problems by floating bodies in variable bathymetry regions.

For this purpose it is very important to investigate the absorbing layer parameters, offering a good comparison between the BEM numerical solution and the analytic solution (which is available for flat bottom). To start with, the description of the studied environment is presented in Figure 3.8. The diffraction and radiation potentials have to be evaluated on the wetted surface of the floating body ∂D_c, the horizontal bottom surface ∂D_Π and the free surface ∂D_F. In accordance with the present absorbing layer model, the free surface boundary condition is modified as follows,

$$\frac{\partial \Phi}{\partial n} - \mu(\omega)\Phi = 0, \quad r \in \partial D_F , \tag{3.49}$$

where $\mu = \omega^2 / g$ and the coefficient $\sigma = 1$ everywhere on ∂D_F, except in the absorbing layer where it is given by,

$$\mu(\omega) = \frac{1}{g}\left(\omega + ic(\omega)\frac{(R-R_a)^n}{\lambda^n} \right)^2 , \; R = \sqrt{x_1^2 + x_2^2} > R_a \quad , \tag{3.50}$$

which is an extension of Eq.(2.41) in the present 3D problem. In the above equation (3.50) λ the local wavelength and R_a denotes the starting radius of the absorbing layer. Using the piecewise constant singularity distribution in the 4-node boundary element, the potential and velocity fields are approximated by,

$$\varphi(r) = \sum_p F_p \Phi_p(r), \; \nabla\varphi(r) = \sum_p F_p \mathbf{U}_p(r) \tag{3.51}$$

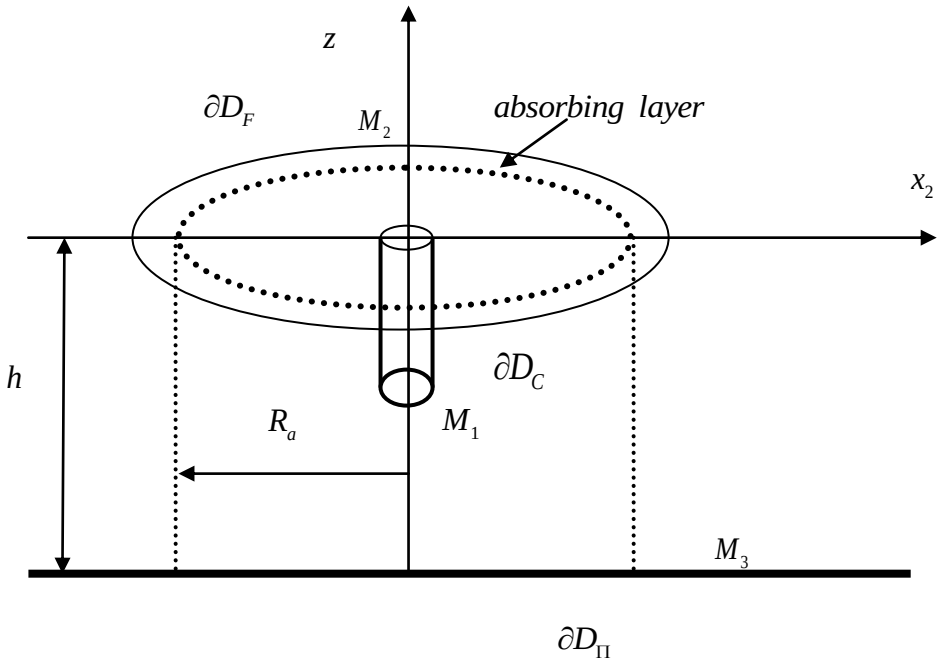

Figure 3.8: Formulation of diffraction and radiation problems in flat bottom regions.

where the summation ranges over all panels (all boundary elements in all parts of the boundary surfaces), and $\Phi_p(r)$ and $\mathbf{U}_p(r)$ denote induced potential and velocity from the p-th element with unit singularity distribution to the field point r, including contribution from each element and its mirror with respect to the bottom with appropriate strength in order to automatically satisfy the bottom boundary condition

$$\frac{\partial \Phi}{\partial n} = 0, \quad r \in \partial D_\Pi. \tag{3.52}$$

Furthermore, the body boundary conditions are presented below in discrete form using the present BEM approximation, as follows

$$\sum_{m=1}^{M} F_p\left(\mathbf{n}_p \mathbf{U}_{pm}\right) = n_{d,p} \text{ (diffraction) or } n_{l,p} \ (l - \text{radiation problem}), \quad p = 1, M_1 \tag{3.53}$$

Where $n_d = -\Phi_{0,1} n_1 - \Phi_{0,2} n_2 - \Phi_{0,3} n_3,$ diffraction problem (3.54)

And for the radiation problems (l=1,2,3,…,6):

$$n_l = \begin{cases} n_1 = n_x, & \text{Surge} \\ n_2 = n_y, & \text{Sway} \\ n_3 = n_z, & \text{Heave} \\ n_4 = zn_2 - yn_3, & \text{Roll} \\ n_5 = xn_3 - zn_1, & \text{Pitch} \\ n_6 = xn_2 - yn_1, & \text{Yaw} \end{cases} \tag{3.55}$$

Also, on the free surface the discrete boundary condition is

$$\frac{F_p}{2} + \sum_{p=1}^{P} F_p \left(\mathbf{n}_p \mathbf{U}_{pm} - \mu \Phi_{pm} \right) = 0, \quad p = M_1 + 1, \ \sum_{i=1}^{2} M_i \tag{3.56}$$

Where the parameter of the absorbing layer is

$$\mu(\omega) = \begin{cases} \dfrac{\omega^2}{g}, & R < R_a \\ \dfrac{\omega^2}{g}\left(1 + i\tilde{c}\dfrac{\left(R - R_a\right)^n}{\lambda^n} \right)^2, & R \geq R_a \end{cases} \tag{3.57}$$

3.7.1 Meshing

An important part of the present BEM implementation deals with the construction of the mesh on the various parts of the boundary. The discretization is accomplished by incorporating corresponding meshes on the floating body, that a cylindrical distribution of panels is applied too, but with a radius sharp decreasing , using a great exponent root, as it is shown in Figure 3.9.

The free surface grid is based on cylindrical distribution of panels around the waterline of the floating cylinder. An important feature of the present method is the continuous junction of the various parts of the mesh, which, in conjunction with the quadrilateral elements, ensures global continuity of the boundary. The following Figure 3.10 is presented below for the free surface.

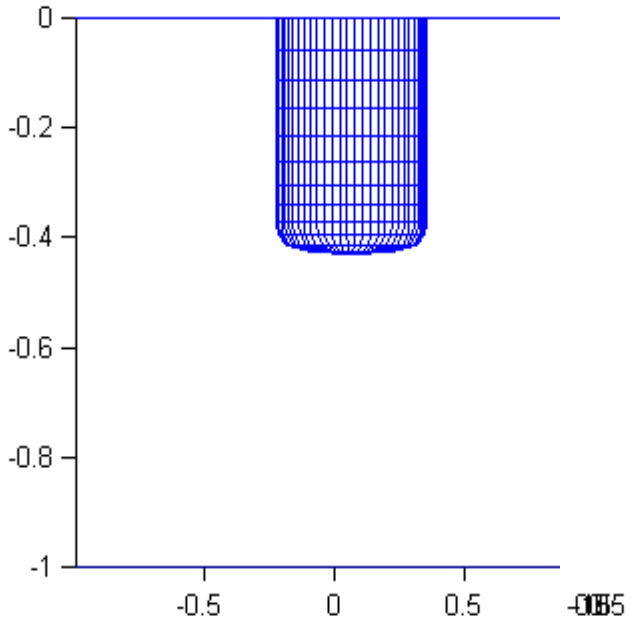

Figure 3.9: Construction of the computational grid for a simple WEC. The mesh on the wetted surface of the body is 12 (in the vertical) X 88(in the azimuthal direction) elements.

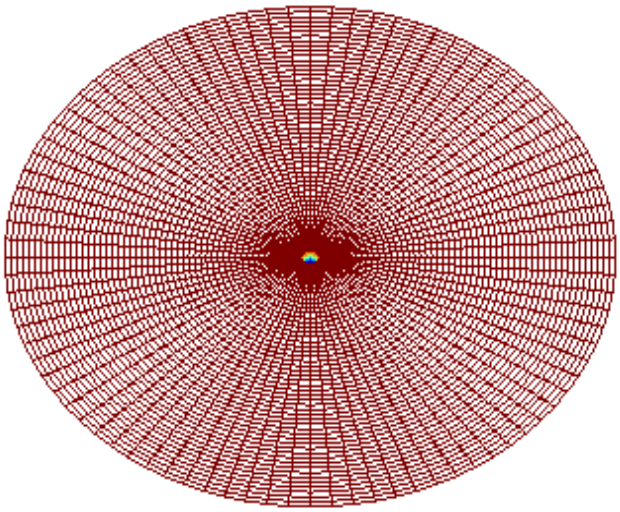

Figure 3.10: Construction of the cylindrical computational grid on the free surface and the body (top view).

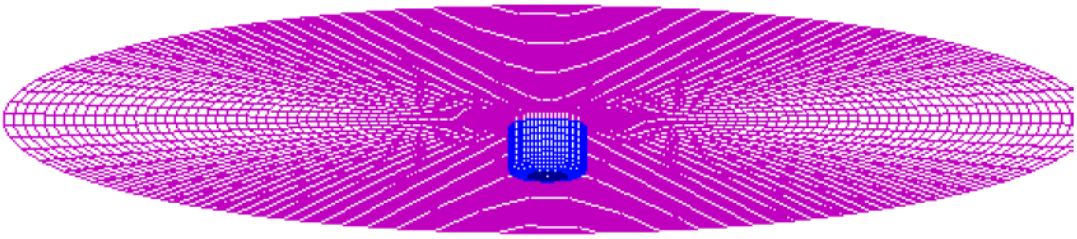

Figure 3.11: Construction of the cylindrical computational grid for the free surface and the body (3D view). The position of the bottom is also shown, however, it is not involved in the computational mesh since the bottom boundary condition is satisfied by mirroring techniques.

Another type of meshing is used, which consists of two parts, the one close to the waterline of the floating unit and the far part; see Fig.3.12. The near mesh is based on cylindrical distribution of panels around the waterline of the floating cylinder that gradually deforms in order to end in a rectangular boundary. After the rectangular boundary, the inner mesh on the free surface, the mesh again deforms to become a cylindrical arrangement on the outer part, which is optimum for the numerical representation of the radiating behavior of the solution of the studied diffraction and multiple scattering problems.

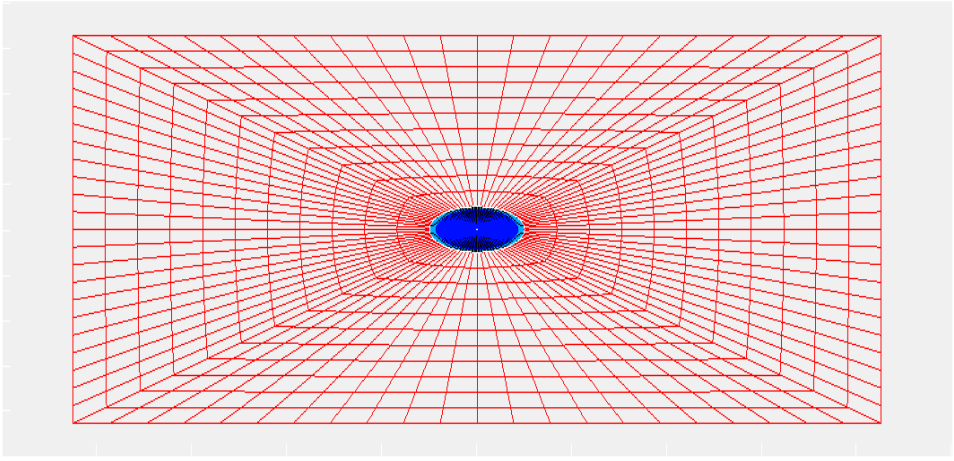

Figure 3.12: Construction of the rectangular computational grid for the free surface near body.

The bottom mesh is based on a cylindrical distribution in our case, where the bottom is flat. In the next chapter, the problem of variable bathymetry is faced and an appropriate meshing is required. In this chapter, bottom meshing is not needed, since a mirroring method is used to satisfy the bottom boundary condition. With this treatment we save significant computing time and to increase the number of the elements on the free surface, which enables the systematic study for the optimization of the absorbing layer parameters.

3.7.2 Numerical results

We consider a floating cylinder approximated using 6x88 or 12x88 elements to model its geometry, where the first number denotes elements along the depth direction and the second number azimuthally distributed elements. On the free surface a variable number of elements per wave length are used including the absorbing layer, which is large enough for numerical approximation. In our case, the free surface is extended for 5 wavelengths distance from the axis of the floating cylinder. As the number of elements is increased, a better approximation is achieved, for the absorbing layer characteristics determination. The meshing of the various parts of the problem is implemented in Matlab® , and subsequently the solver is a fortran code internally called in order to evaluate the induced potential and velocity from the p-th element to the center of the m-th element serving as the collocation point(s). The numerical quadratures used to calculate the induced quantities over a quadrilateral element are presented in more detail in Appendix A.

3.7.3 Absorbing layer

In this chapter the absorbing layer is again introduced, as it is described in Chapter 2, with some (minor) changes explained below. As it is known, absorbing layer is used to substitute the exact radiation conditions, which in more complicated problems are unknown. In our case, the analytic solution of the floating cylinder oscillating over a flat bottom is known and will be used to evaluate the absorbing layer performance. The main parameters of the absorbing layer are :

- Dimensionless Frequency, $\tilde{\omega} = \sqrt{\frac{\omega^2 \cdot h}{g}}$
- Coefficient, $\tilde{c} = \frac{c \cdot \lambda^n}{\omega}$
- The activation length(or activation distance per wave length), $x_0\left(\frac{r}{\lambda}\right)$
- The exponent, n
- The number of panels per wave length, $\frac{N}{\lambda}$

The dimensional frequency takes values corresponding to swallow, intermediate and deep water conditions, in order to optimize absorbing layer in the whole frequency range. The activation length varies from half a wavelength to 2 wavelengths. The exponent can be *n*=2, 3 or 4 and the number of panels per wavelength can be 10,15 or 20. The general equation of the absorbing layer remains the same.

$$\mu(\omega)=\frac{\omega^2}{g}\left(1+i\tilde{c}\frac{(R-R_a)^n}{\lambda^n}\right)^2,\ R=\sqrt{x_1^2+x_2^2}>R_a \tag{3.59}$$

The main difference between Chapter 2 and Chapter 3 concerning the absorbing layer, is that in this part the dimensional coefficient takes values according to the wave frequency.

$$c=0.01+\left(\frac{\omega}{\omega_{\max}}\right)^5 \quad \omega\le 4\ rad/s \tag{3.60}$$

$$c=0.01+\left(\frac{\omega}{\omega_{\max}}\right)^7 \quad \omega>4\ rad/s \tag{3.61}$$

This change is made, since this model works better in 3D boundary element problems in relation with the method in Chapter 2.

3.7.4 Discussion of numerical results

In this Section, first an optimization of the absorbing layer characteristics is presented, by examining the difference between the analytical potential and the approximate solution on the free surface. After that results concerning the added mass, damping coefficient , Froude-Krylov and diffraction forces are presented and discussed, for two different cylinder geometries. In the beginning, we consider a cylinder of radius $\alpha=0.2857m$ and draft $T=1.5a$, in constant depth regions $a/h=1/3.5$. The present BEM is used to calculate the potential using 6×88 elements on ∂D_C and 75×88 elements for whole part of the free surface ∂D_F which includes the absorbing layer. In our case the number of elements varies from 10 to 20 elements per wave length and the free surface extends for 5 wave lengths from the cylinder axis. The total number of elements is 7128. A finer mesh of 9328 elements is also considered for comparison and illustration of convergence properties. As it is mentioned and above, the absorbing layer depends on various parameters. Giving different values for these parameters and comparing the analytic solution with the approximate, we lead in the best combination. The code gives as a result the Chebyshev norm of the difference between the analytic and approximate potential. These parameters are presented below:

- Dimensionless Frequency, $\tilde{\omega} = \omega\sqrt{\frac{h}{g}}$
- Coefficient, $\tilde{c} = \frac{c \cdot \lambda^n}{\omega}$
- The activation length(or activation distance per wave length), $x_0\left(\frac{r}{\lambda}\right)$
- The exponent, n
- The number of panels per wave length, $\frac{N}{\lambda}$

$$\omega = \begin{cases} 1\,rad/s \\ 2.3\,rad/s, \\ 5.3\,rad/s \end{cases} \quad \omega\sqrt{h/g} = \begin{cases} 0.3193(\text{shallow}) \\ 0.7343(\text{intermediate}) \\ 1.6922\ (\text{deep}) \end{cases} \quad \frac{r}{\lambda} = \begin{matrix} 0.5 \\ 1 \\ 2 \end{matrix} \quad n = \begin{matrix} 2 \\ 3 \\ 4 \end{matrix} \quad \frac{N}{\lambda} = \begin{matrix} 10 \\ 15 \\ 20 \end{matrix}$$

The PML is based on Eqs. (3.60) where ω_{max}=8rad/s.

In comparison with Chapter 2, the coefficient is changed and as a consequence the program runs 81 times to find the best combination. We choose this form of c, since it makes the approximation better. Below, some figures are presented, comparing the approximate (BEM) and the analytic potential on the free surface, in the case of heaving motion.

Case: $\omega = 1 rad/s \quad n = 2 \quad r/\lambda = 3 \quad N/\lambda = 20$

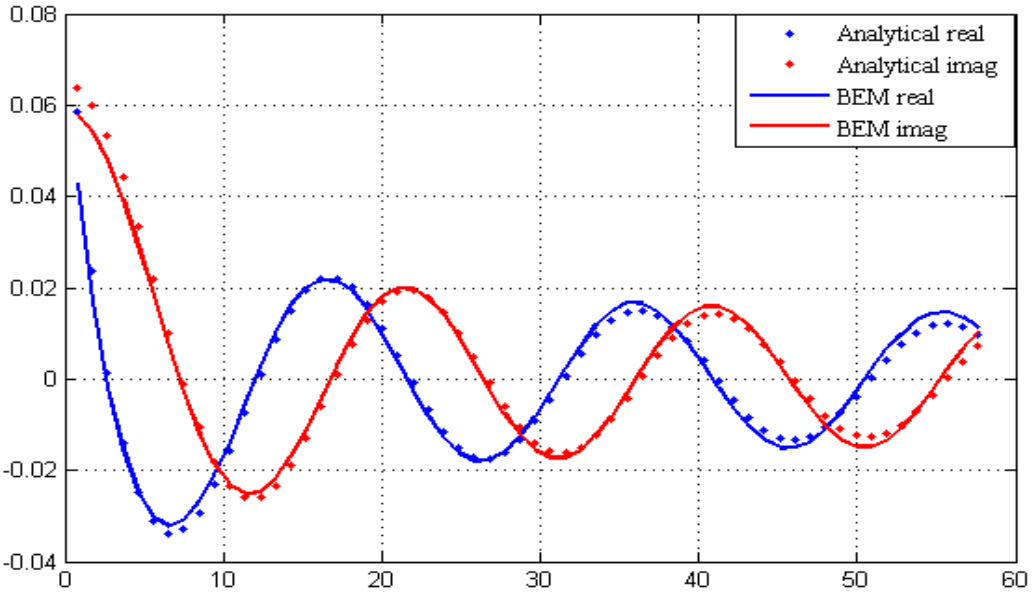

Figure 3.13: Real and imaginary part of the analytic and approximate solution for ω=1 *rad/s*

Case: $\omega = 2.3 rad/s \quad n = 3 \quad r/\lambda = 3 \quad N/\lambda = 20$

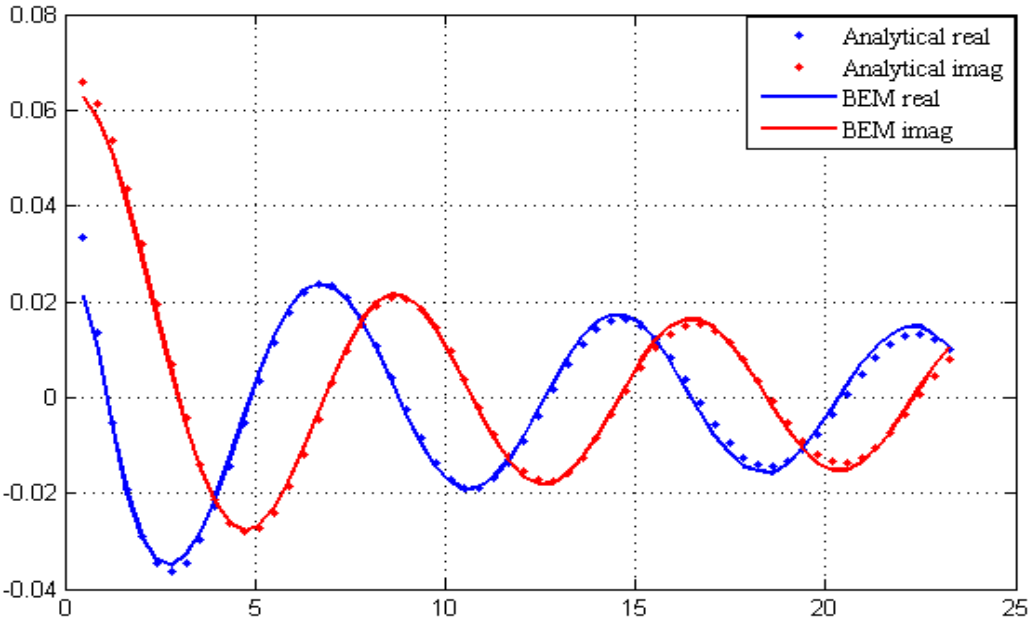

Figure 3.14: Real and imaginary part of the analytic and approximate solution for ω=2.3 *rad/s*.

Case: $\omega = 5.3 rad/s \quad n = 2 \quad r/\lambda = 3 \quad N/\lambda = 15$

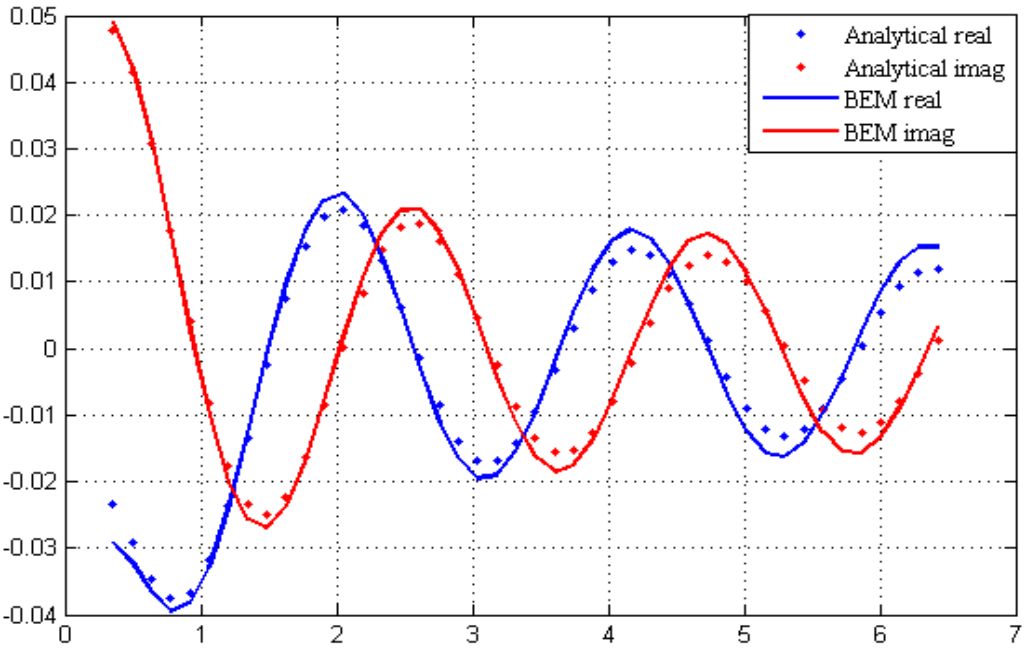

Figure 3.15: Real and imaginary part of the analytic and approximate solution for ω=5.3 *rad/s*.

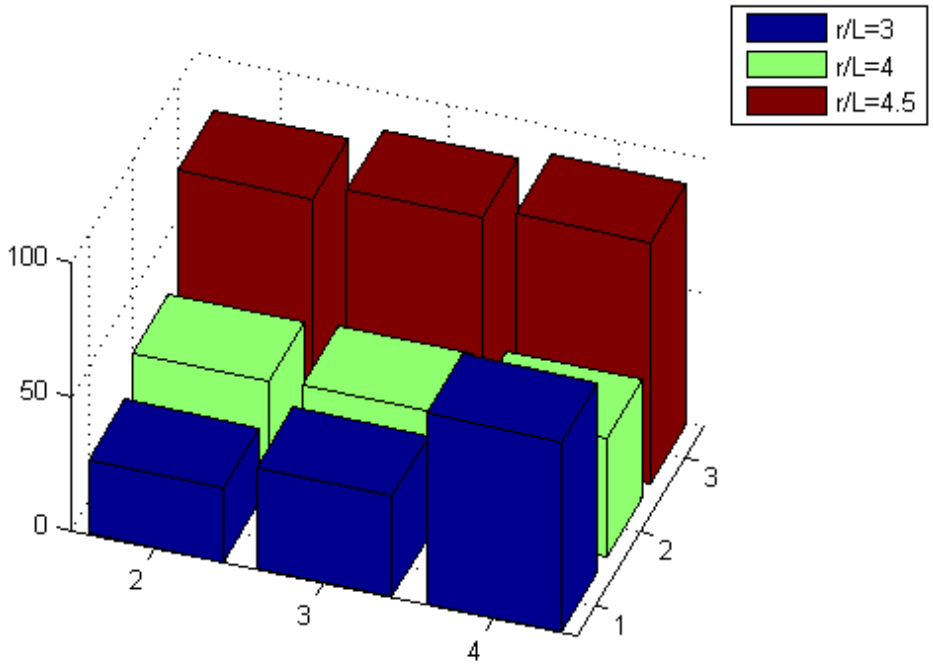

Figure 3.16: Error distribution of the analytic and approximate solution for case: $\omega = 1 rad/s \quad and \quad N/\lambda = 10$

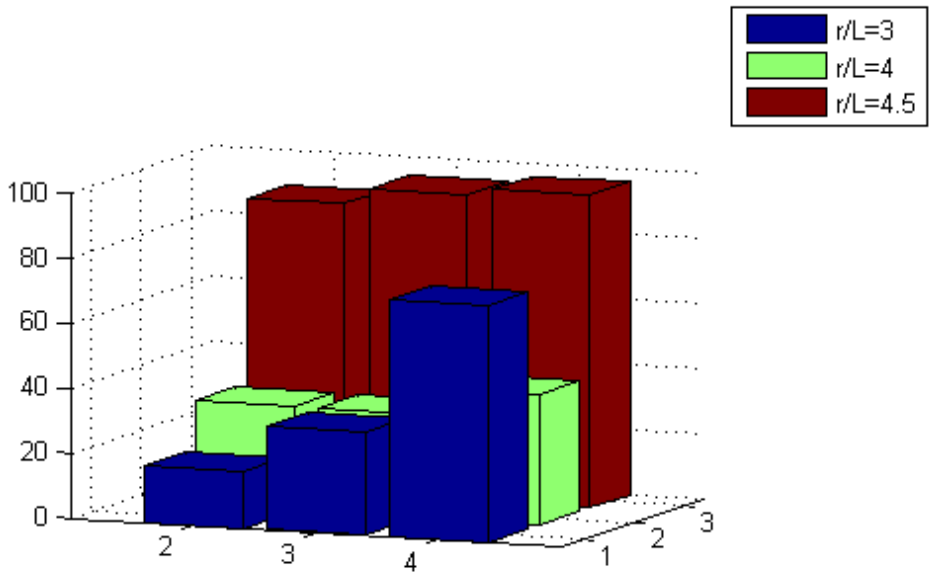

Figure 3.17: Error distribution of the analytic and approximate solution for case: $\omega = 1 rad/s \quad and \quad N/\lambda = 15$.

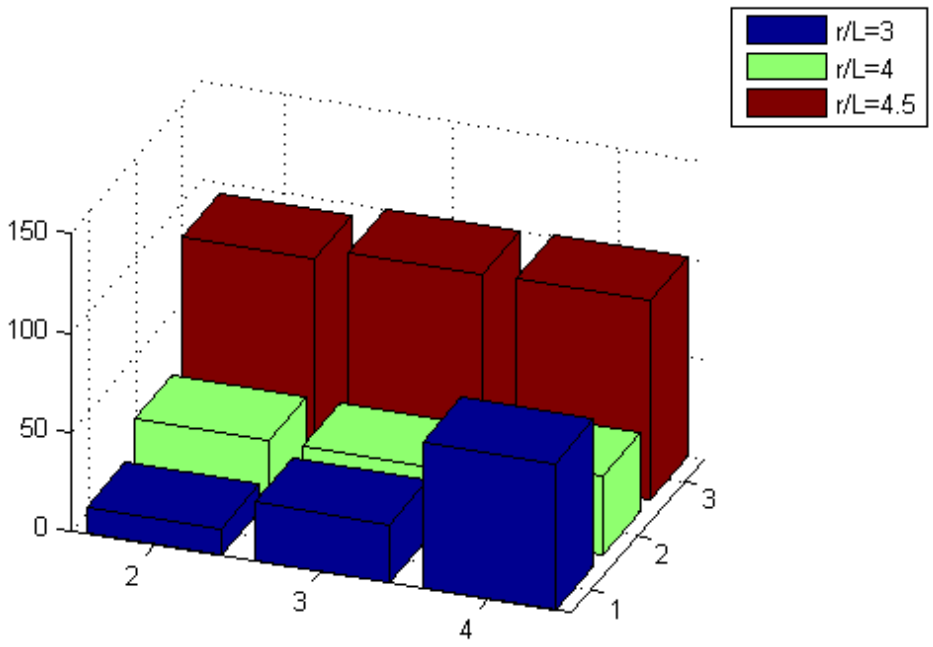

Figure 3.18: Error distribution of the analytic and approximate solution for case: $\omega = 1 rad/s \quad and \quad N/\lambda = 20$.

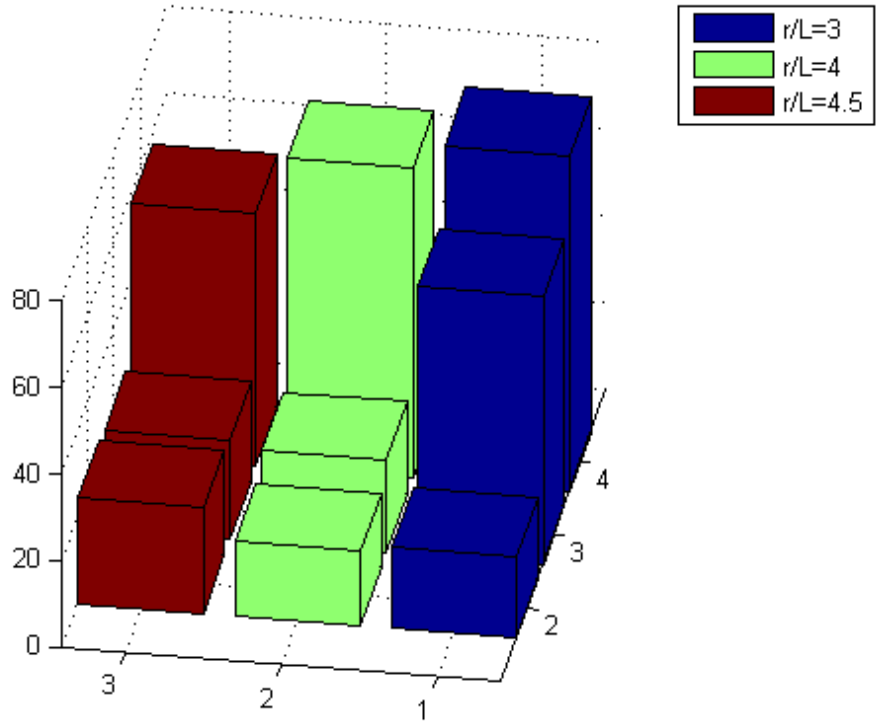

Figure 3.19: Error distribution of the analytic and approximate solution for case: $\omega = 2.3 rad/s \quad and \quad N/\lambda = 10$.

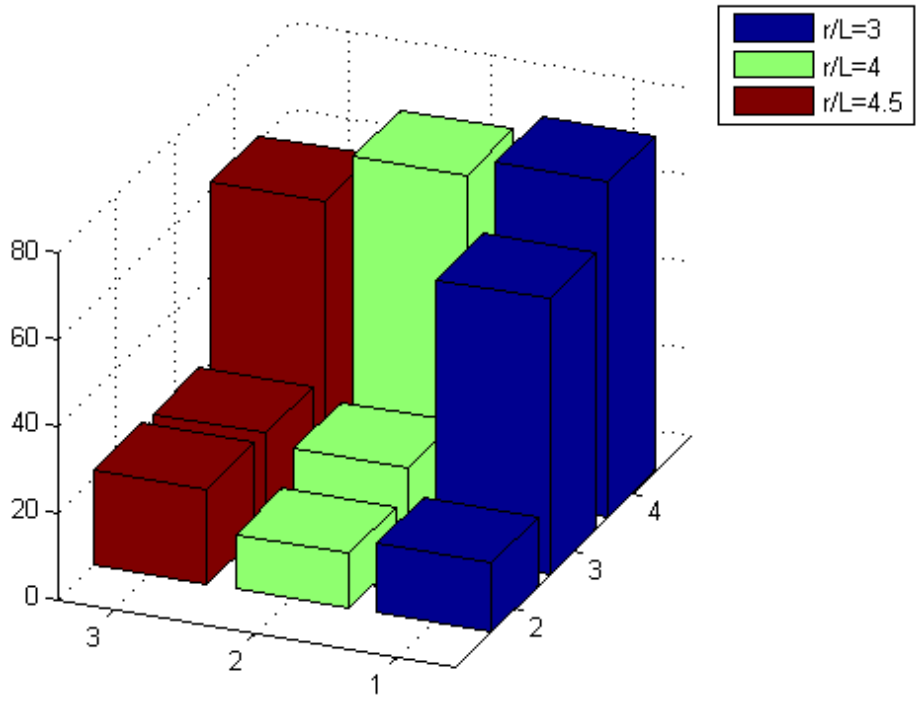

Figure 3.20: Error distribution of the analytic and approximate solution for case: $\omega = 2.3 rad/s \quad and \quad N/\lambda = 15$

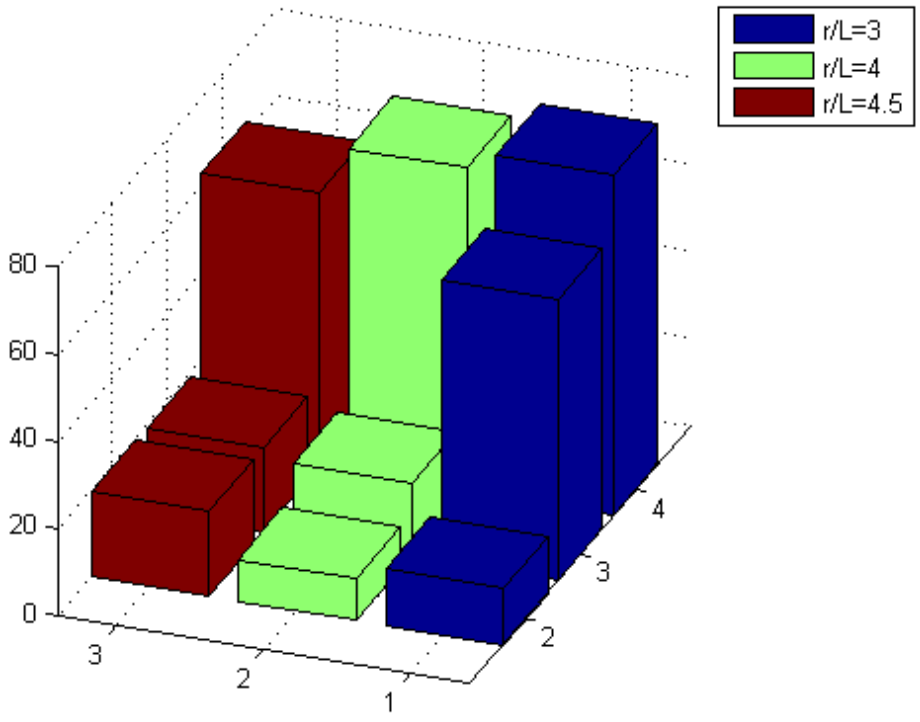

Figure 3.21: Error distribution of the analytic and approximate solution for case: $\omega = 2.3 rad/s \quad and \quad N/\lambda = 20$

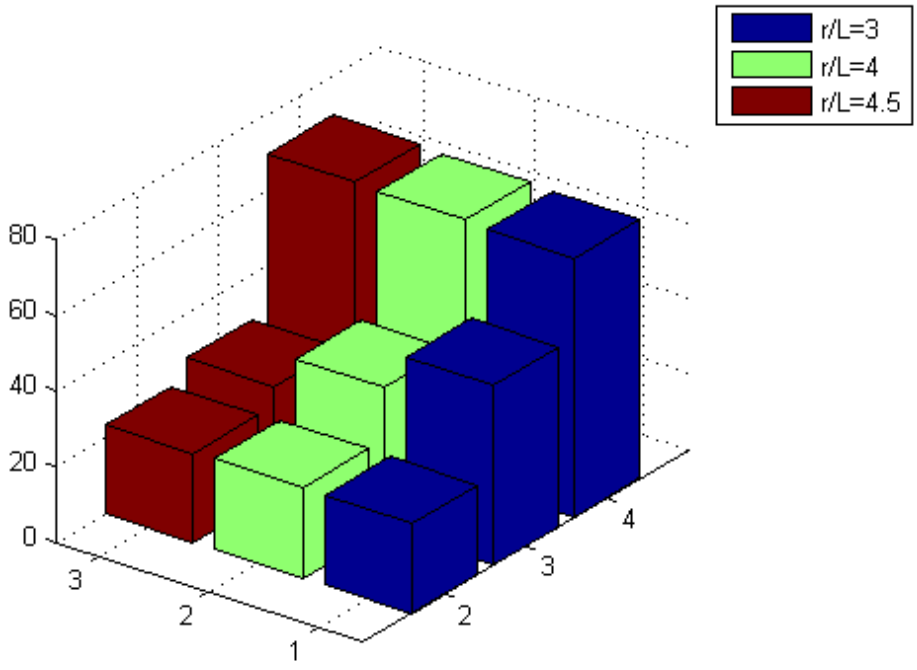

Figure 3.22: Error distribution of the analytic and approximate solution for case: $\omega = 5.3 rad/s \quad and \quad N/\lambda = 10$

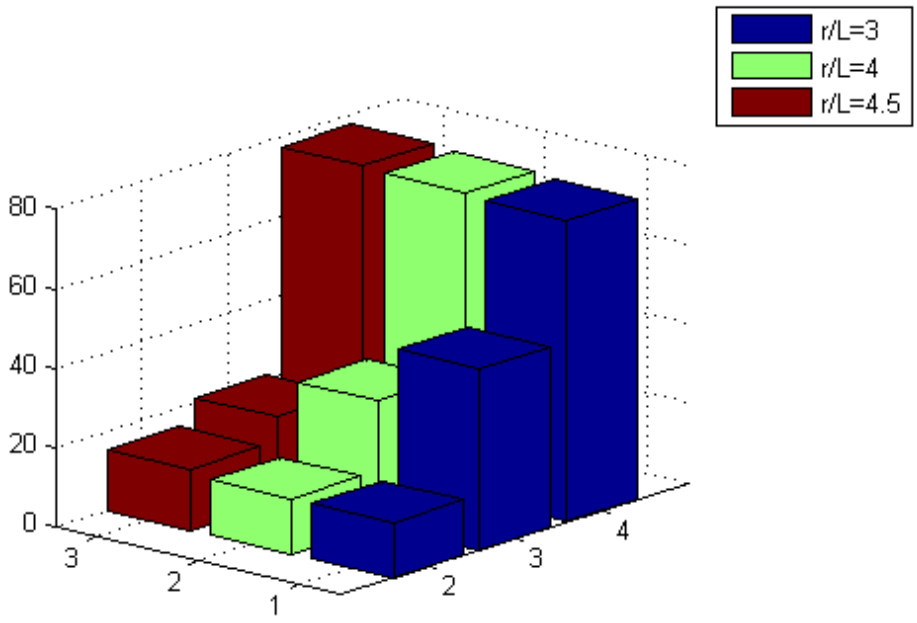

Figure 3.23: Error distribution of the analytic and approximate solution for case: $\omega = 5.3 rad/s \quad and \quad N/\lambda = 15$

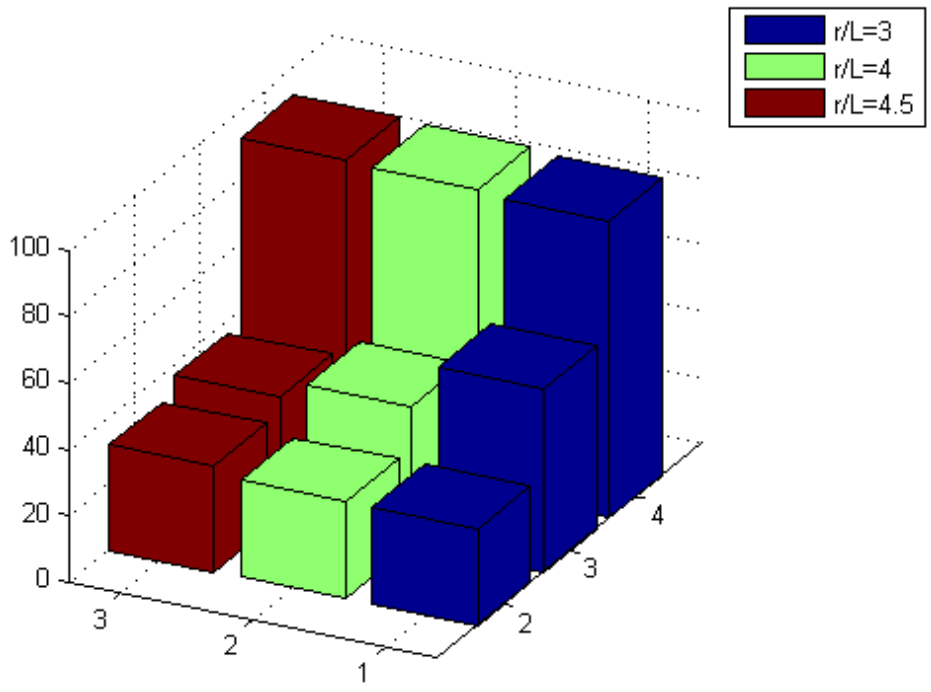

Figure 3.24: Error distribution of the analytic and approximate solution for case: $\omega = 5.3 rad/s \quad and \quad N/\lambda = 20$

As it is seen, for all the frequencies and number of elements per wave length, the best performance is obtained by using $n = 2 \quad and \quad r/\lambda = 3$. We observe that in high frequencies and consequently in deep water, that in case of $N/\lambda = 20$ the error is increased in comparison with the case of $N/\lambda = 15$. Generally, the results follow the same pattern as the ones of Chapter 2, as the best combination is the same and in low and intermediate frequencies the increase in the number of elements offers smaller error.

We consider now a single cylindrical body of radius $\alpha = 0.2857m$ and draft $T = 1.5a$, in constant depth regions $a/h = 1/3.5$. Choosing the best combination of parameters for the absorbing layer, we present in Fig.3.25 the added mass and damping coefficient in relation with the non-dimensional frequency $\omega\sqrt{\alpha/g}$, from BEM, for the above floating cylinder and we compare them with the corresponding analytical results. This comparison is made for 2 meshes on the body. One mesh with 6×88 elements and one with 12×88 elements. This is made to have a better approximation to body geometry and also to the body coefficients. Also, in Fig.3.26, the Froude-Krylov and diffraction forces are presented comparing BEM solution against analytical results.

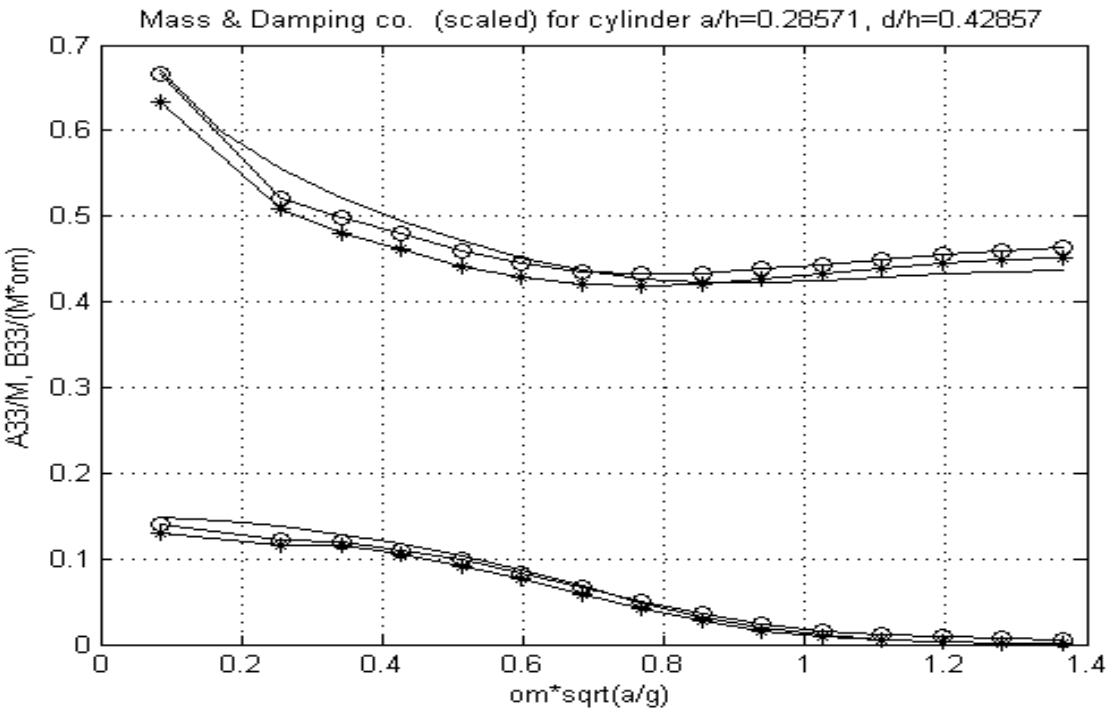

Figure 3.25: Non-dimensionalized cylinder hydrodynamic coefficients for various values of non-dimensionalized frequency $\omega\sqrt{a/g}$. BEM results by using the 6x88 mesh on the body are shown by using circles, and by 12x88 by using stars. Analytic solution is indicated by using solid lines.

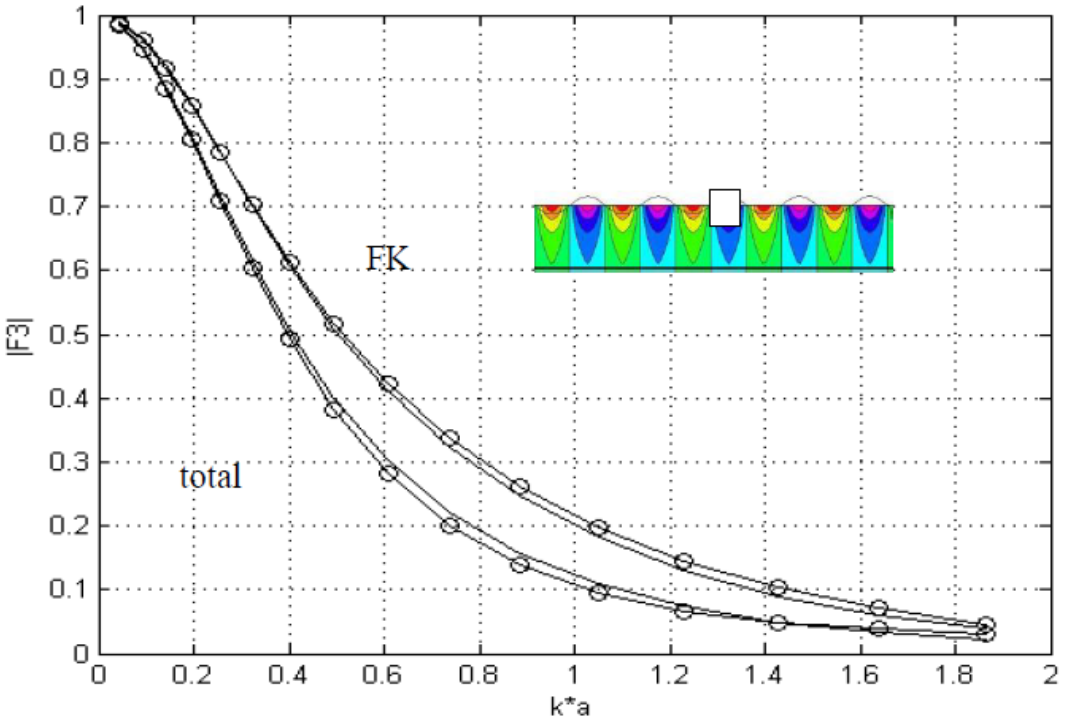

Figure 3.26: Non-dimensionalized cylinder hydrodynamic Froude-Krylov and total forces for various values of non-dimensionalized wavenumber $k_0 a = 2\pi a/\lambda$. BEM results by using the 6x88 mesh on the body are shown by using circles, and analytic solution is indicated by using solid lines.

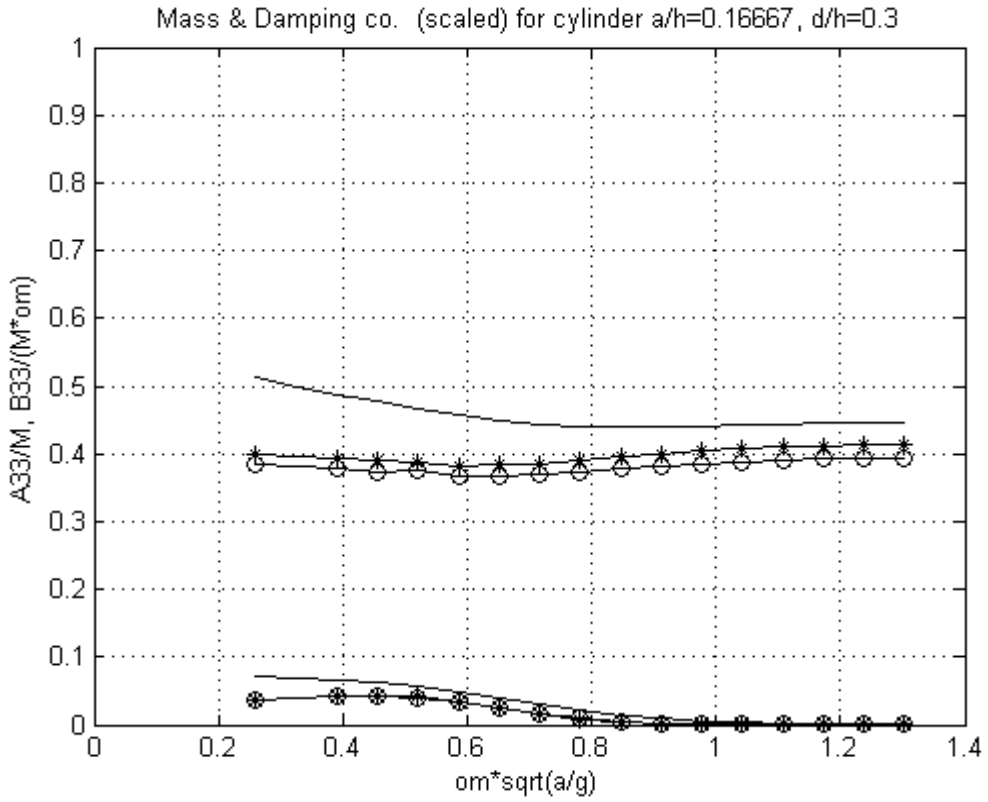

Figure 3.27: Non-dimensionalized cylinder hydrodynamic coefficients for various values of non-dimensionalized frequency $\omega\sqrt{a/g}$. BEM results by using the 6x88 mesh on the body are shown by using circles, and by 12x88 by using stars. Analytic solution is indicated by using solid lines.

Now we consider another cylindrical body of radius $a/h=0.167$ and draft $T=1.8a$ in constant depth regions $h=1m$. Also, in this case we present the added mass and damping coefficient in relation with the non-dimensional frequency $\omega\sqrt{\alpha/g}$. Furthermore, we evaluate the Froude-Krylov and diffraction forces with regard to $k\,a$.

The PML is based on Eqs (3.60) where ω_{max}=8 rad/s.

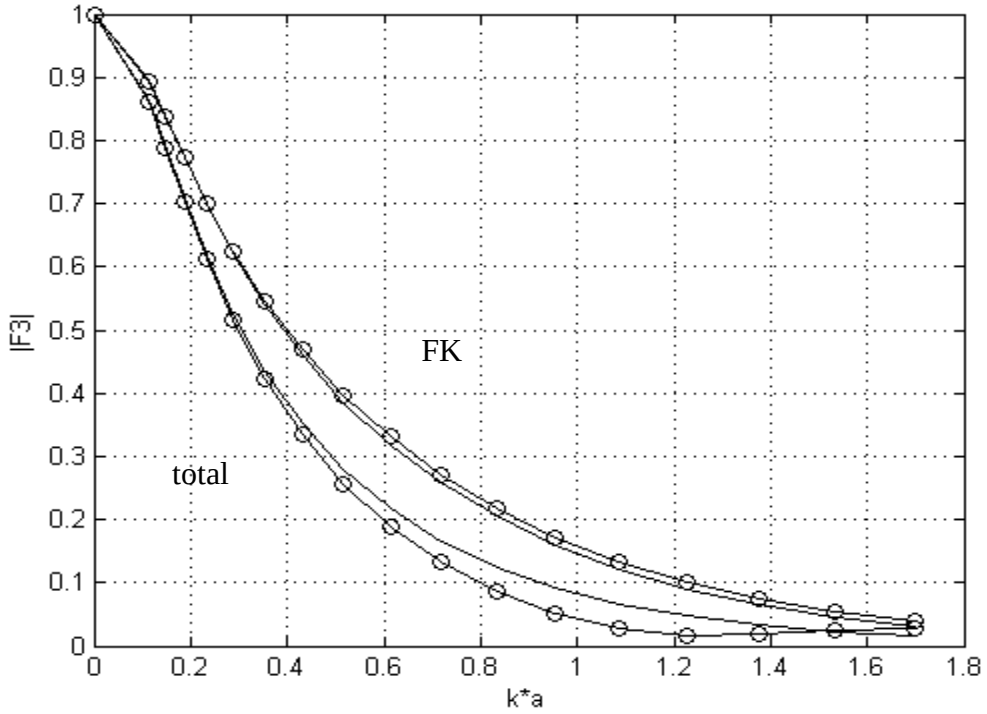

Figure 3.28: Non-dimensionalized cylinder hydrodynamic Froude-Krylov and total forces for various values of non-dimensionalized wavenumber $k_0 a = 2\pi a / \lambda$. BEM results by using the 6x88 mesh on the body are shown by using circles, and analytic solution is indicated by using solid lines.

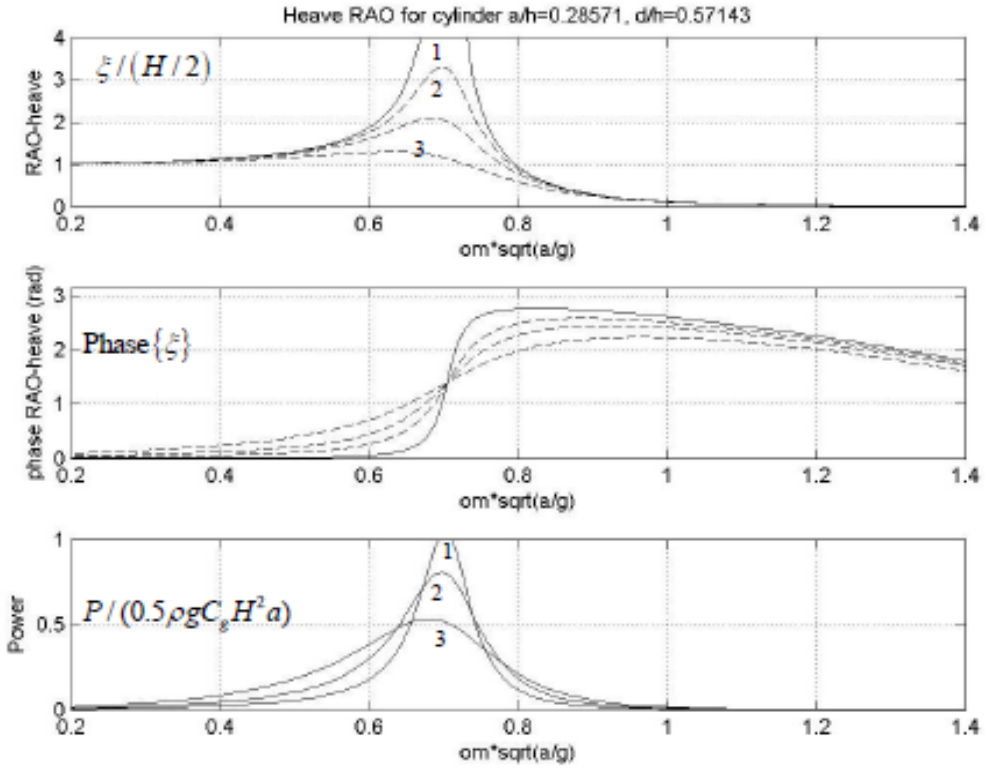

Figure 3.28. Added mass and damping coefficients for floating cylinder of radius a=10m and draft d/a=1.5 in constant depth h/a=3.5. Responses in the case of freely floating cylindrical body against nondimensional frequency $\omega\sqrt{a/g}$, as modified by PTO modelled by damping constants B_S /b_m=5,10,20 (shown by dashed lines and indicated as 1,2,3, respectively). The corresponding output power is shown in the last subplot.

The present BEM results are found in satisfactory agreement with various techniques to treat such problems in homogeneous environments based on eigenfunction expansions (e.g. Yeung 1980). Furthermore, the WEC responses (both modulus and phase) of the heaving WEC are plotted in the top subplots of Fig.3.28, both for the freely floating body (shown by solid lines) and for three selected values for the PTO damping coefficient B_S (shown by dashed lines). The indicative values considered correspond to 5,10,20 times a mean value of hydrodynamic damping b_m over frequency (estimated as $2\pi b_m / m\omega_R = 0.12$, where the resonance frequency $\omega_R\sqrt{a/g} = 0.7$) which are indicated by a number. In the last subplot of Fig.3.28 the output power of the WEC by the above PTO, normalized with respect to the incident wave powerflux defined as $P/(0.5)\rho C_g H^2 a$ and estimated by using $\eta_{eff} = 1$, is plotted. We observe in this figure the maximization of the output around the resonance which in the examined case is around the non-dimensional frequency $\omega_R\sqrt{a/g} = 0.7$. Also, it is observed in this figure that higher values of PTO damping produce lower output powerlevels, however spread in wide frequency bands around the resonant frequency.

Chapter 4

PML-BEM FOR 3D FLOATING BODIES IN VARIABLE BATHYMETRY

The interaction of free-surface gravity waves with floating bodies, in water of intermediate depth and in variable bathymetry regions, is an interesting problem finding important applications and can be treated by the above method. Specific examples concern the design and evaluation of performance of special-type ships and structures operating in nearshore and coastal waters; see, e.g., Mei (1983, Ch.7). Also, pontoon-type floating bodies of relatively small dimensions find applications as coastal protection devices (floating breakwaters) and are also frequently used as small boat marinas; see, e.g., Drimer et al (1992). In all these cases, the estimation of wave-induced loads and motions of the floating structure can be based on the solution of classical wave-body-seabed hydrodynamic interaction problems; see, e.g., Wehausen (1971). In this final Chapter, the developed Boundary Element method is applied to estimate the hydrodynamic behaviour of a body with arbitrary geometry, in a variable bathymetry region. The BEM is used, in conjunction with the best combination of parameters of the the absorbing layer, as it is studied before.

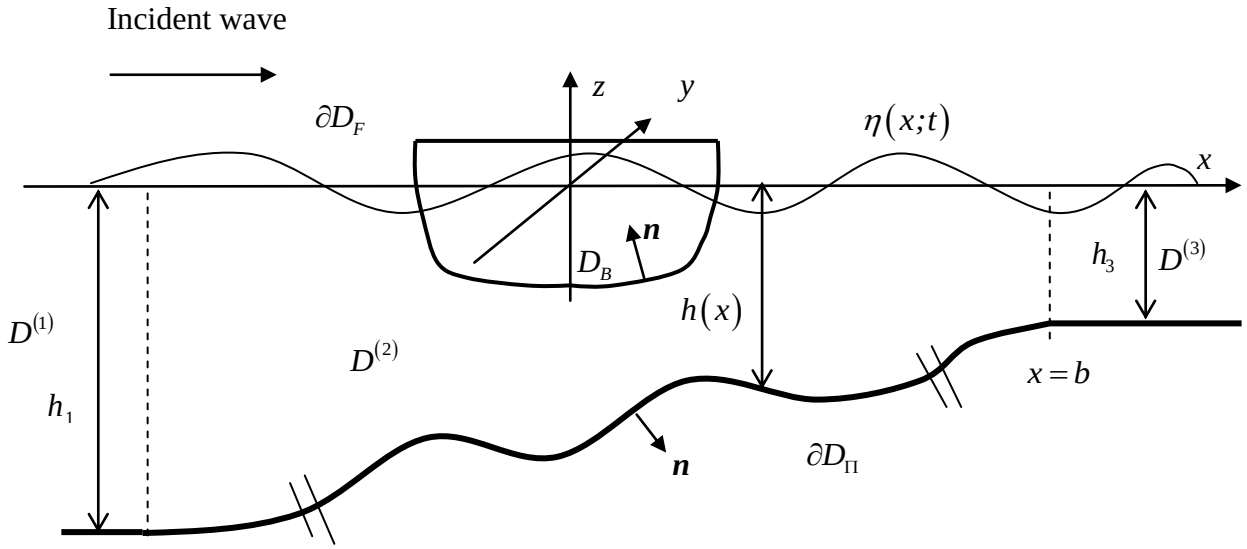

Figure 4.1:Formulation of diffraction and radiation problems in variable bathymetry regions.

We consider here the hydrodynamic problem concerning the behavior of a generally-shaped body, D_B, of characteristic radius *a* and draft *d*, operating in the nearshore environment, as shown in Fig. 4.1.

An important part of the formulation deals with the calculation of the propagating water-wave field over the variable bathymetry region, without the presence of the body. For simplicity, the variable bathymetry region is considered between two infinite subregions of constant, but possibly different depths $h = h_1$ (region of incidence) and $h = h_3$ (region of transmission). In the middle subregion it is assumed that the depth h exhibits an arbitrary variation. The wave field is excited by a harmonic incident wave of angular frequency ω, propagating with direction θ; see Fig.4.1. Under the assumptions that the free-surface elevation and the wave velocities are small, the wave potential is expressed as follows

$$\Phi(\mathbf{x}, z; t) = \mathrm{Re}\left\{-\frac{igH}{2\omega}\varphi(\mathbf{x}, z; \mu)\cdot\exp(-i\omega t)\right\} \tag{4.1}$$

where $\mathbf{x} = (x_1, x_2)$, and satisfies the linearised water wave equations; see, e.g., Mei (1983). In the above equation H is the incident wave height, g is the acceleration due to gravity, $\mu = \omega^2 / g$ is the frequency parameter, and $i = \sqrt{-1}$. The free surface elevation is then obtained in terms of the wave potential as follows,

$$\eta(\mathbf{x}; t) = -\frac{1}{g}\frac{\partial\Phi(\mathbf{x}, z=0)}{\partial t}. \tag{4.2}$$

Using standard floating-body hydrodynamic theory (e.g. Wehausen 1971), the complex potential can be decomposed as follows,

$$\varphi(\mathbf{x}, z) = \varphi_P(\mathbf{x}, z) + \varphi_D(\mathbf{x}, z) + \frac{2\omega^2}{gH}\varphi_R(\mathbf{x}, z), \tag{4.3}$$

$$\varphi_R(\mathbf{x}, z) = \sum_{\ell=1}^{6}\xi_\ell\varphi_\ell(\mathbf{x}, z), \tag{4.4}$$

where $\varphi_P(\mathbf{x}, z)$ is the normalized propagation wave potential in the variable bathymetry region in the absence of the body, $\varphi_D(\mathbf{x}, z)$ is the diffraction potential due to the presence fixed (motionless) body D_B, that satisfies the boundary condition $\partial\varphi_D(\mathbf{x}, z)/\partial n = -\partial\varphi_P(\mathbf{x}, z)/\partial n$ on the body, where $\mathbf{n} = (n_1, n_2, n_3)$ the normal vector on the wetted surface of the body, directed outwards the fluid domain (inwards the body). Furthermore, $\varphi_\ell(\mathbf{x}, z)$, denotes the radiation potential in the non-uniform domain associated with the ℓ-oscillatory motion of the body with complex amplitude ξ_ℓ, satisfying $\partial\varphi_\ell(\mathbf{x}, z)/\partial n = n_\ell$, equal to the ℓ-component of

generalized normal vector on the wetted surface of the body ($n_\ell = (\mathbf{r}\times\mathbf{n})_{\ell-3}$ for $\ell = 4,5,6$). In the present work the field $\varphi_P(\mathbf{x},z)$ will be calculated by means of the coupled-mode model developed by Athanassoulis & Belivassakis (1999), described in the next subsection and in more detail in Appendix B.

In the case when the body is a simple heaving WEC only the vertical oscillation of the body is considered $\xi = \xi_3$, which is one of the most power intensive modes concerning this type of wave energy systems. In the sequel we will concentrate on this simpler configuration, leaving the analysis of the more complex case to be examined in future work. For a heaving WEC the hydrodynamic response is obtained by

$$\xi_3 = (A)^{-1}(X_P + X_D), \tag{4.5}$$

where $X_P + X_D$ denote the exciting vertical force on each WEC due to propagating and diffraction field, respectively, and the coefficient A is given by

$$A = -\omega^2(M + a_{33}) - i\omega(B_S + b_{33}) + (C_S + c) \tag{4.6}$$

where M is the body mass . The hydrodynamic coefficients (added mass and damping) of the above system Eq.(5) are calculated by the following integrals

$$a_{33} - \frac{1}{i\omega} b_{33} = \rho \iint_{\partial D_B} \varphi_3 n_3 \, dS, \tag{4.7}$$

of the heaving-radiation potential of the WEC on the wetted surface ∂D_B of the WEC. Moreover, $c = \rho g A_{WL}$ is the hydrostatic coefficient in heaving motion with A_{WL} the waterline surface, and B_S ,C_S are characteristic constants of the Power Take Off (PTO) system. The components of the exciting (Froude-Krylov and diffraction) forces are calculated by the following integrals of the corresponding potentials,

$$X_P = \frac{\rho g H}{2} \iint_{\partial D_B} \varphi_P n_3 \, dS, \tag{4.8}$$

$$X_D = \frac{\rho g H}{2} \iint_{\partial D_B} \varphi_D n_3 \, dS, \tag{4.9}$$

on the wetted surface ∂D_B of the WEC. The total power extracted by the WEC is obtained as

$$P(\omega,\theta) = \eta_{eff} \, \omega^2 \left| B_S (\xi_3)^2 \right|, \tag{4.10}$$

where η_{eff} indicates the efficiency of the PTO (that could be a function of the frequency ω).

Obviously the calculated performance depends on the frequency, direction and waveheight of the incident wave, as well as on the physical environment.

4.1 The coupled-mode model

In the case of waves in variable bathymetry region there is no analytic solution for the wave potential $\varphi_P(\mathbf{x},z)$ associated with the propagation of water waves in the variable bathymetry region. The wave potential $\varphi_P(\mathbf{x},z)$ associated with the propagation of water waves in the variable bathymetry region, without the presence of the scatterer (floating body), can be conveniently calculated by means of the consistent coupled-mode model developed by Athanassoulis & Belibassakis (1999), as extended for three-dimensional environments by Belibassakis et al (2001). This model is based on an enhanced coupled mode method, which is described in detail in Appendix B. Generally, this model is based on the following enhanced local-mode representation:

$$\varphi_P(\mathbf{x},z)=\varphi_{-1}(\mathbf{x})Z_{-1}(z;\mathbf{x})+\sum_{n=0}^{\infty}\varphi_n(\mathbf{x})Z_n(z;\mathbf{x}) \tag{4.11}$$

In the above expansion, the term $\varphi_0(\mathbf{x})Z_0(z;\mathbf{x})$ denotes the propagating mode of the generalised incident field. The remaining terms $\varphi_n(\mathbf{x})Z_n(z;\mathbf{x}),\quad n=1,2,\ldots,$ are the corresponding evanescent modes, and the additional term $\varphi_{-1}(\mathbf{x})Z_{-1}(z;\mathbf{x})$ is a correction term, called the sloping-bottom mode, which properly accounts for the satisfaction of the Neumann bottom boundary condition on the non-horizontal parts of the bottom.

The function $Z_{-1}(z;\mathbf{x})$ is defined as the vertical structure of the sloping-bottom mode. This term is introduced in the series in order to consistently satisfy the Neumann boundary condition on the non-horizontal parts of the seabed. It becomes significant in the case of seabottom topographies with non-mildly sloped parts and has the effect of significant acceleration of the convergence of the local mode series; see Athanassouis & Belibassakis (1999). By following the procedure described in the latter work, the coupled-mode system of horizontal equations for the amplitudes of the incident wave field propagating over the variable bathymetry region is finally obtained, in the form

$$\sum_{n=-1}A_{mn}(\mathbf{x})\nabla^2\varphi_n(\mathbf{x})+B_{mn}(\mathbf{x})\nabla\varphi_n(\mathbf{x})+C_{mn}(\mathbf{x})\varphi_n(\mathbf{x})=0,\quad m=-1,0,1,\ldots., \tag{4.12}$$

where the coefficients A_{mn}, B_{mn}, C_{mn} are defined in terms of the vertical modes $Z_n(z;\mathbf{x})$. The coefficients are dependent on $\mathbf{x}$ through $h(\mathbf{x})$ and the corresponding expressions can be found in Table 1 of Appendix B. The system is supplemented by appropriate boundary conditions specifying the incident waves and treating reflection, transmission and radiation of waves.

4.2 Bem for the diffraction and radiation problems

The corresponding problems on the diffraction and radiation potentials $\varphi_D(\mathbf{x},z)$ and $\varphi_\ell(\mathbf{x},z)$, associated with the dynamics of the floating body, are treated, as in Chapter 3, by means of the same low-order Boundary Element Method, based on simple singularity distributions and 4-node quadrilateral boundary elements (see, e.g. Beer et al 2008), ensuring continuity of the geometry approximation of the various parts of the boundary. The potential and velocity fields are again approximated by,

$$\varphi(\mathbf{r})=\sum_p F_p\Phi_p(\mathbf{r}),\quad \nabla\varphi(\mathbf{r})=\sum_p F_p\mathbf{U}_p(\mathbf{r}) \tag{4.13}$$

where the summation ranges over all panels and $\Phi_p(\mathbf{r})$ and $\mathbf{U}_p(\mathbf{r})$ denote induced potential and velocity from the p-th element with unit singularity distribution to the field point ***r*** (see, e.g., Katz & Plotkin 1996). We remark here that in the present case the bottom boundary is also included and discretized into elements along with the other parts of the boundary, i.e. the body wetted surface and the free surface. Again, in order to eliminate the infinite extent of the domain and treat the radiating behaviour of the diffraction and radiation fields at far distances from the bodies, the Chapter 3 absorbing layer technique is used, based on a matched layer all around the fore and side borders of the computational domain on the free surface, choosing the best parameters combination, as it is exported in Chapter 3.

Thus, the diffraction and radiation potentials are represented by integral formulations with support only on the wetted surface of the floating body ∂D_B, the bottom surface ∂D_Π and free surface ∂D_F; see Fig.4.2. In accordance with the present absorbing layer model, the free surface boundary condition is modified as it is described in Chapter 3,

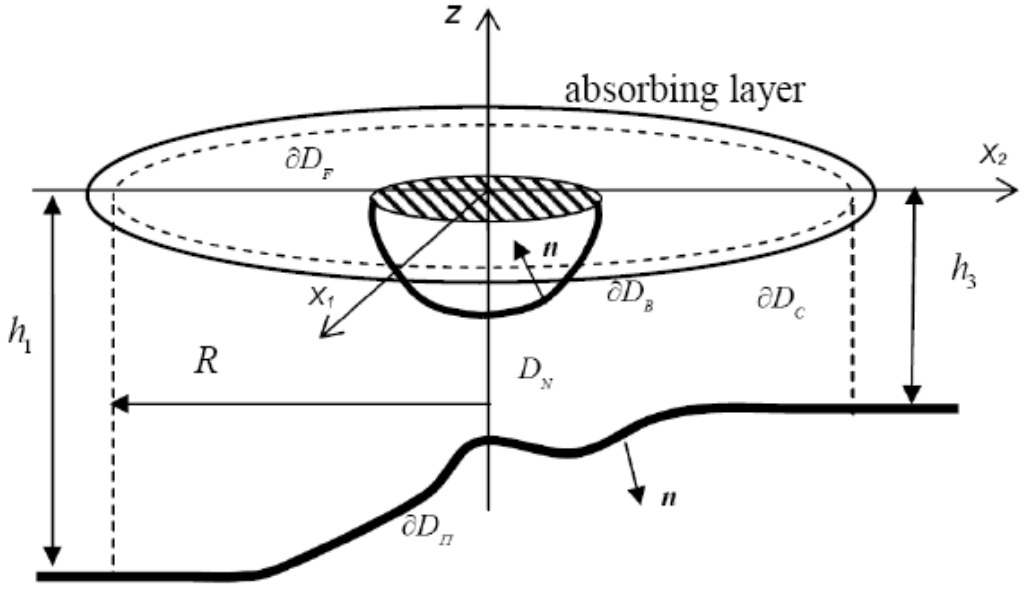

Figure 4.2. Formulation of diffraction and radiation problems in variable bathymetry regions.

$$\frac{\partial \Phi}{\partial n} - \mu(\omega)\Phi = 0, \quad r \in \partial D_F , \tag{4.14}$$

where $\mu = \omega^2 / g$ and the coefficient $\sigma = 1$ everywhere on ∂D_F, except in the absorbing layer where it is given by,

$$\mu(\omega) = \frac{\omega^2}{g}\left(1 + i\tilde{c}\frac{(R - R_a)^n}{\lambda^n}\right)^2 , \; R = \sqrt{x_1^2 + x_2^2} > R_a \tag{4.15}$$

In the above equation λ is the local wavelength. Also the starting radius of the absorbing layer $R_a >> \lambda$. The discrete solution is then obtained using collocation method, by satisfying the boundary conditions at the centroid of each panel on the various parts of the boundaries. Induced potentials and velocities from each panel to any collocation point are calculated by numerical quadratures, treating the self-induced quantities semi-analytically, as it is shown in Appendix A. The body and bottom boundary conditions are presented below:

$$\frac{\partial \Phi}{\partial n} = 0 , \quad r \in \partial D_\Pi \tag{4.16}$$

$$\frac{\partial \Phi}{\partial n} = n_d \text{ (diffraction) or } n_l \text{ } (l - \text{radiation problem}), \quad r \in \partial D_B \tag{4.17}$$

With the appropriate formulation we conclude to the following linear system:

$$\sum_{m=1}^{M} F_p\left(\mathbf{n}_p \mathbf{U}_{pm}\right) = n_{d,p} \text{ (diffraction) or } n_{l,p} \text{ } (l - \text{radiation problem}), \quad p = 1, M_1 \tag{4.18}$$

$$\text{Where } n_d = -\Phi_{0,1} n_1 - \Phi_{0,2} n_2 - \Phi_{0,3} n_3, \text{ diffraction problem} \tag{4.19}$$

And for the radiation problems (l=1,2,3,…,6):

$$n_l = \begin{cases} n_1 = n_x, & \text{Surge} \\ n_2 = n_y, & \text{Sway} \\ n_3 = n_z, & \text{Heave} \\ n_4 = zn_2 - yn_3, & \text{Roll} \\ n_5 = xn_3 - zn_1, & \text{Pitch} \\ n_6 = xn_2 - yn_1, & \text{Yaw} \end{cases} \tag{4.20}$$

Also, on the free surface the discrete boundary condition is

$$\frac{F_p}{2} + \sum_{p=1}^{P} F_p \left(\mathbf{n}_p \mathbf{U}_{pm} - \mu \Phi_{pm} \right) = 0, \quad p = M_1 + 1, \ \sum_{i=1}^{2} M_i \tag{4.21}$$

Where the parameter of the absorbing layer is

$$\mu(\omega) = \begin{cases} \dfrac{\omega^2}{g}, & R < R_a \\ \dfrac{\omega^2}{g}\left(1 + i\tilde{c}\dfrac{\left(R - R_a\right)^n}{\lambda^n} \right)^2, & R \geq R_a \end{cases} \tag{4.22}$$

Finally, on the bottom surface the discrete boundary condition is

$$\frac{F_p}{2} + \sum_{m=1}^{M} F_p \left(n_p U_{pm} \right) = 0, \quad p = \sum_{i=1}^{2} M_i + 1, \ \sum_{i=1}^{3} M_i \tag{4.23}$$

M_1 *Body*
M_2 *Free – surface*
M_3 *Bottom*

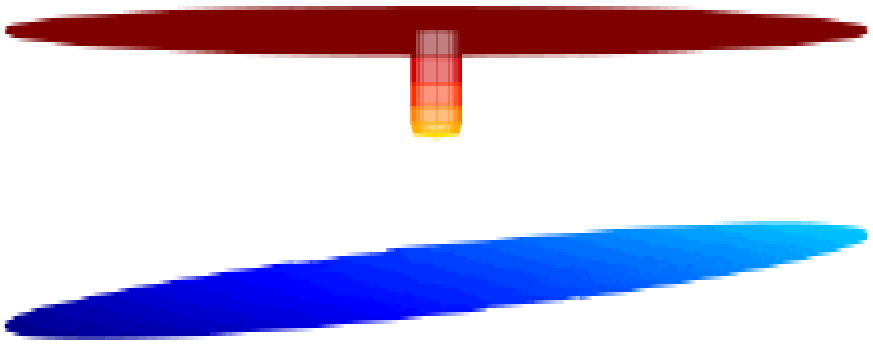

Figure 4.3. Construction of the computational grid for simple WEC

4.2.1 Meshing

An important part of the present BEM implementation deals with the construction of the mesh on the various parts of the boundary. That part is discussed in Chapter 3, but in this Chapter there is a variable bottom geometry, so we give details about the bottom meshing. The bottom follows cylindrical arrangement in meshing, as the free surface, and it is formulated with a lower number of elements, increasing the number of elements on the free surface. Body and free surface follow a similar arrangement in meshing. In case of the body, the cylindrical arrangement, is optimum for the numerical representation of the radiating behaviour of the solution of the studied diffraction and multiple scattering problems. More specifically in Fig.4.3 the mesh on the free surface around a single WEC is plotted. The discretization is accomplished by the incorporation corresponding meshes on each floating body and on the bottom variable bathymetry surface, as shown in Fig.4.3 . An important feature is the continuous junction of the various parts of the mesh, which, in conjunction with the quadrilateral elements, ensures global continuity of the geometry approximation of the boundary.

4.2.2 Absorbing layer

As it is described in Chapter 3, the absorbing layer is used in this Chapter, with its best combination of parameters, giving results for the problem of an arbitrary geometry body, floating in a variable bathymetry region.. As it is known, absorbing layer is used to substitute the radiation condition, which in more complicated problems is unknown. In our case, radiation condition is unknown, so we trust the conclusion of Chapter 3. The main parameters of the absorbing layer are :

- Dimensionless Frequency, $\tilde{\omega} = \sqrt{\frac{\omega^2 \cdot h}{g}}$
- Coefficient, $\tilde{c} = \frac{c \cdot \lambda^n}{\omega}$
- The activation length(or activation distance per wave length), $x_0\left(\frac{r}{\lambda}\right)$
- The exponent, n
- The number of panels per wave length, $\frac{N}{\lambda}$

In our case, we choose the activation length to be equal to 2 wave lengths. The exponent will be equal to 3 and the number of panels per wave length will be 15. The general equation of the absorbing layer remains the same.

$$\mu(\omega) = \frac{\omega^2}{g}\left(1 + i\tilde{c}\frac{(R - R_a)^n}{\lambda^n}\right)^2 , \; R = \sqrt{x_1^2 + x_2^2} > R_a \tag{4.23}$$

The dimensionalized coefficient gets values according to the wave frequency.

$$c = 0.01 + \left(\frac{\omega}{\omega_{\max}}\right)^5 \quad \omega \le 4 \; rad/s \tag{4.24}$$

$$c = 0.01 + \left(\frac{\omega}{\omega_{\max}}\right)^7 \quad \omega > 4 \; rad/s \tag{4.25}$$

4.2.3 Numerical results and discussion

As an example, we consider a cylindrical body of radius *a*=1/3.5m and draft *d/a*=1.5, in constant depth regions *h/a*=3.5. The present BEM is used to calculate the responses using 6x88 elements on ∂D_B, 75x88 elements on the free surface ∂D_F and 26x88 elements on the bottom surface ∂D_Π, as shown in Fig.4.3. The total number of elements is 9416.

First, we consider a variable bathymetry region of the form of smooth shoal characterized by continuously decreasing depth, from h_1 = 1.5 to h_3 = 0.5; see Fig.4.4. The depth function, presenting monotonic variation along the x_1-axis, is defined by

$$h(x) = h_m - 0.5(h_1 - h_3)\tanh(\alpha x_1)\ , \qquad (17)$$

where the mean depth is $h_m = 0.5(h_1 + h_3)$, and the coefficient $\alpha = 5\%$, and thus, the mean bottom slope is 0.08 and the max bottom slope is 0.03. The horizontal x-extent of the variable bathymetry region is 15. The solution corresponding to the propagating wavefield φ_P for waves of non-dimensional frequency $\omega\sqrt{h_m / g} = 1.44$ is shown in Fig. 4.4, as obtained by the present CMS, Eq.(B.13). Numerical results have been obtained by using 2^{nd}-order finite difference scheme and discretizing the domain by using 201 points and keeping 5 totally modes in the expansion Eq.(B.10), which was found enough for numerical convergence. The wave field (real and imaginary parts) is shown in the Fig.4.4(a) in the case of normally incident waves, and in Fig.4.4(b) for 45deg obliquely incident waves, respectively, by using contours. Also, the wave field on the free surface which is proportional to the free surface elevation is shown in these figures by using solid lines. We clearly observe in this figure the consistent satisfaction of the bottom Neumann boundary condition by the fact that the equipotential lines become perpendicular to the bottom profile.

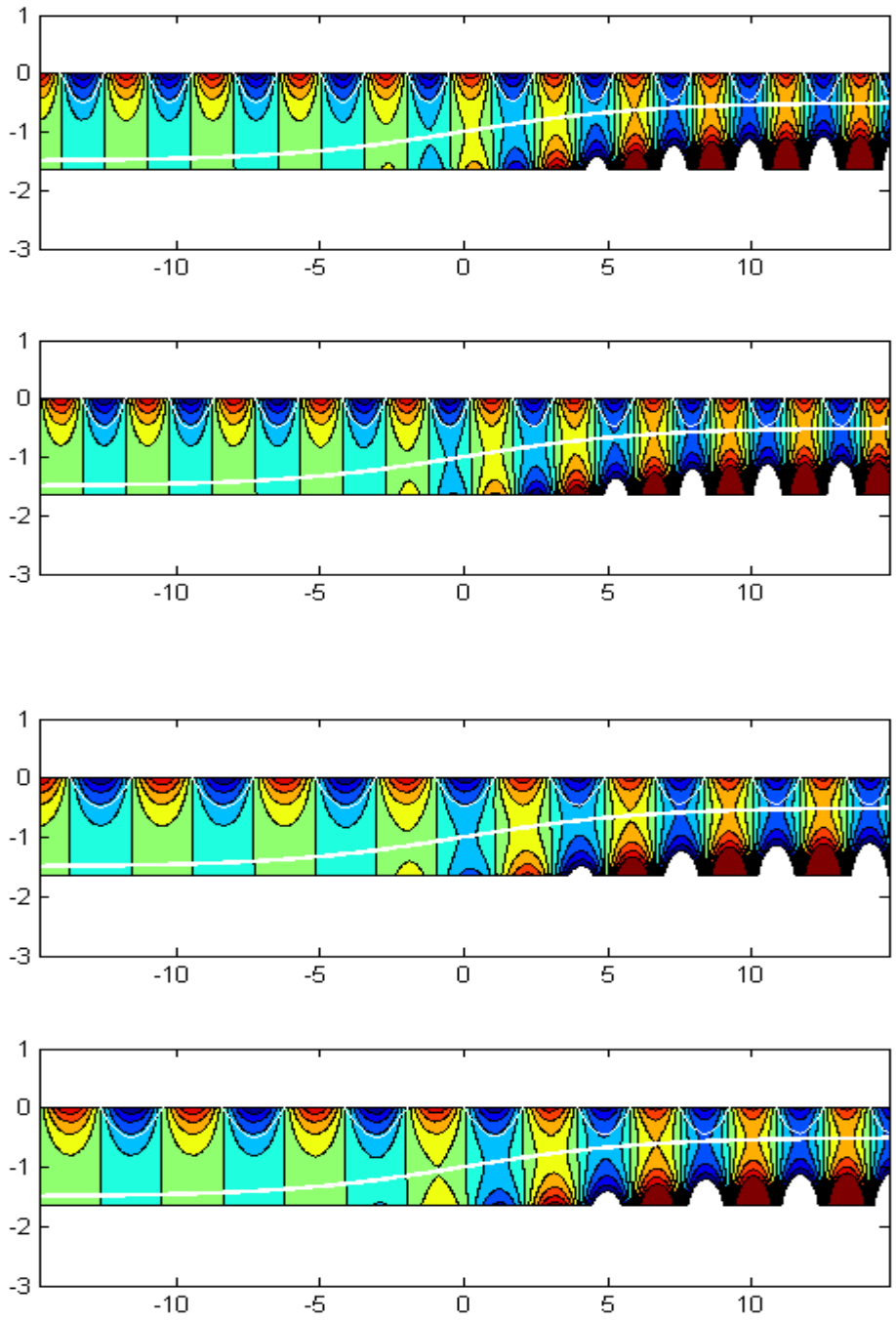

Figure 4.4. (a) Propagating field over a shoaling region, for normally incident waves of nondimensional frequency $\omega\sqrt{h/g}=1.44$. (b) Same as before, but for 45deg obliquely incident waves.

Next, we consider a single cylindrical body of radius a=1/3.5m and draft $d/a=1.5$, floating in the center of the variable bathymetry domain of Fig.4,5. The present BEM is used to calculate the diffraction and radiation fields using the mesh shown in Fig.3(a) with total number of elements is 9416. The calculated diffraction and radiation fields at the non-dimensional frequency $\omega\sqrt{h_m/g}=1.44$, and $\omega\sqrt{a/g}=0.77$, is shown in Fig.6.

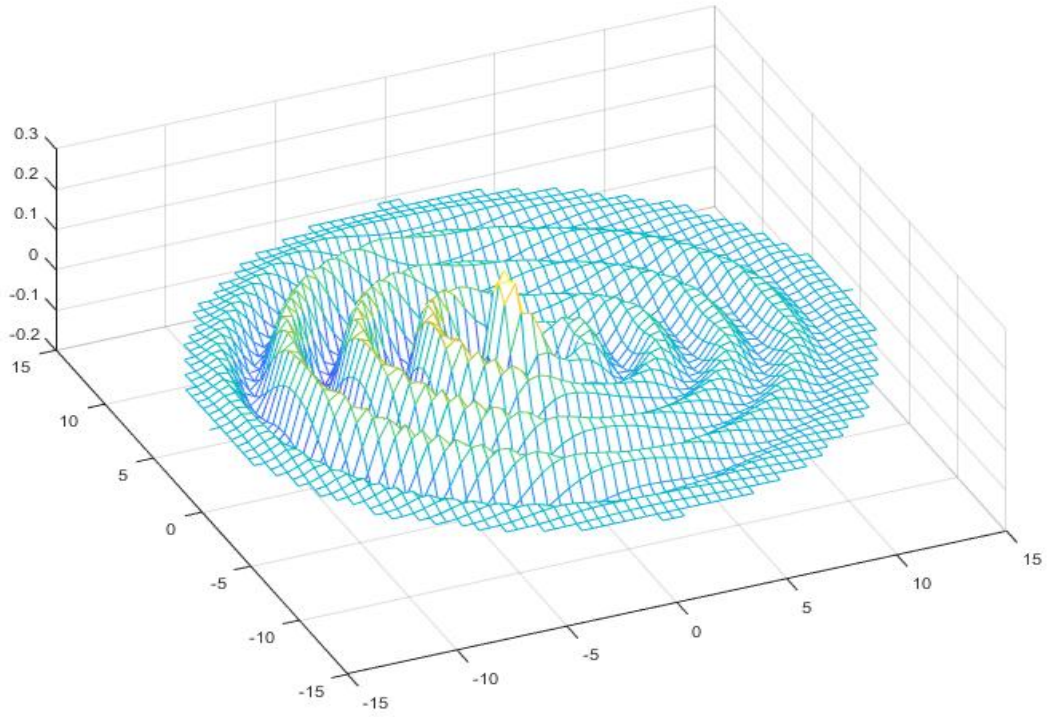

Figure 4.5. Calculated diffraction/radiation fields from a single cylindrical floater (*d/a*=1.5) in the middle of the domain of Fig.4.4 for $\omega\sqrt{a/g}=0.77$. Plots on the free surface of (a) diffraction field radiating potential, as calculated by the present BEM.

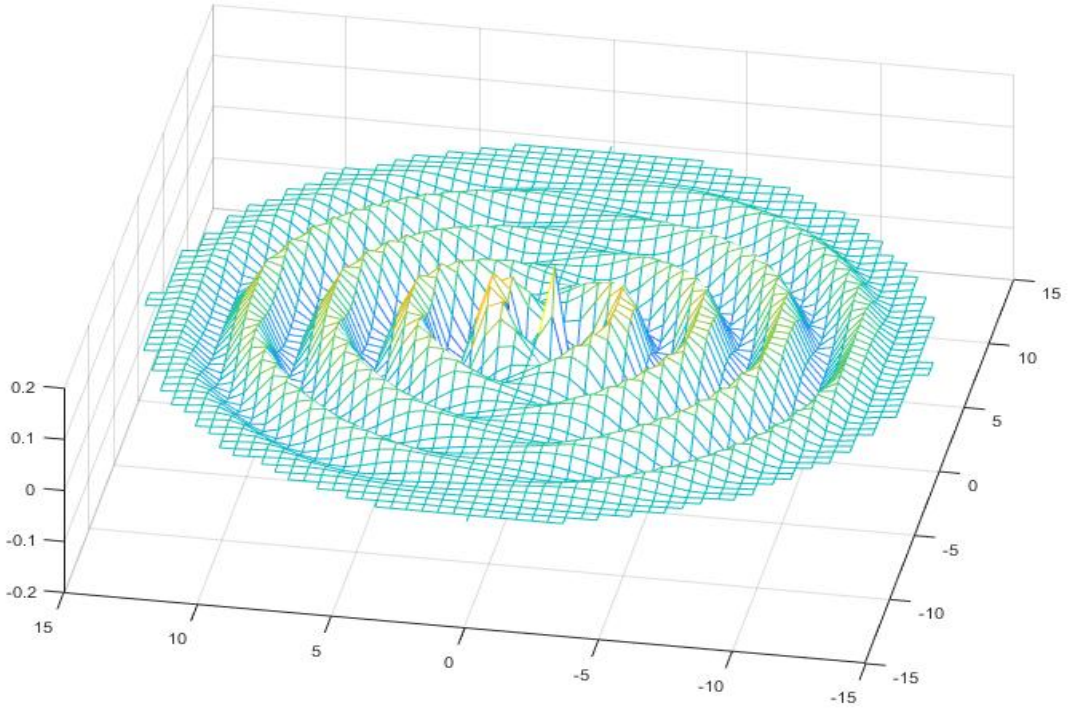

Figure 4.6. Calculated diffraction/radiation fields from a single cylindrical floater (*d/a*=1.5) in the middle of the domain of Fig.4.4 for $\omega\sqrt{a/g}=0.77$. Plots on the free surface of sway field radiating potential, as calculated by the present BEM.

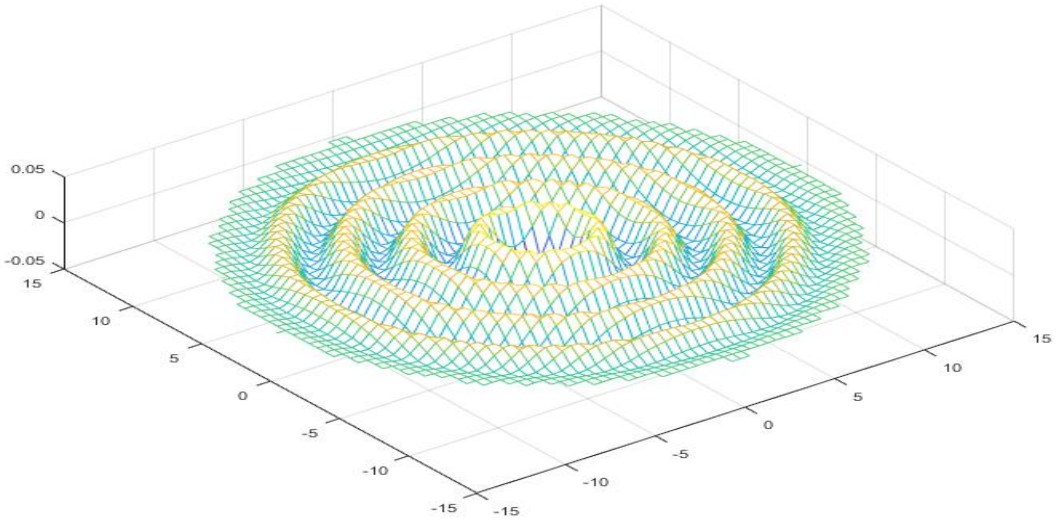

Figure 4.7. Calculated diffraction/radiation fields from a single cylindrical floater (*d/a*=1.5) in the middle of the domain of Fig.4.4 for $\omega\sqrt{a/g}=0.77$. Plots on the free surface of heave field radiating potential, as calculated by the present BEM.

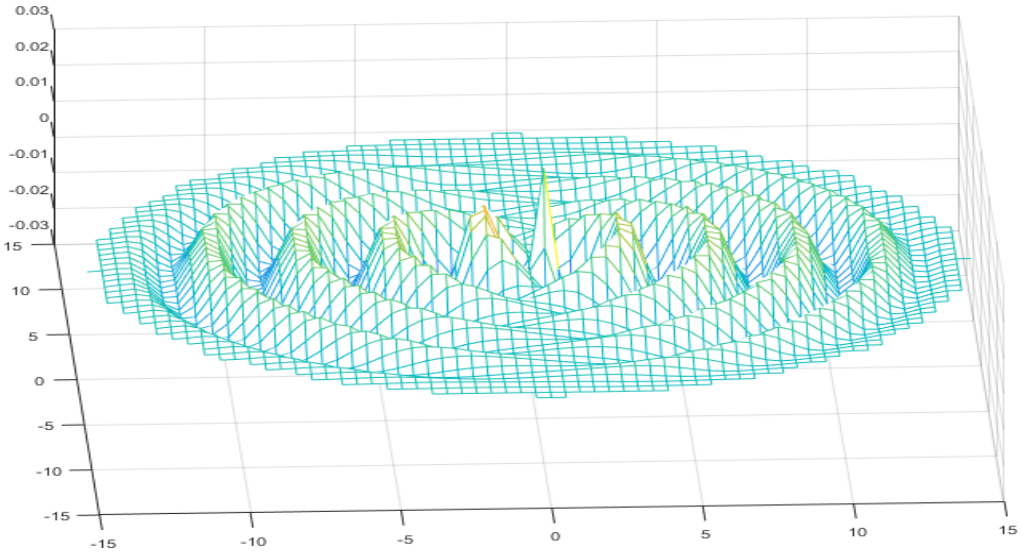

Figure 4.8. Calculated diffraction/radiation fields from a single cylindrical floater (*d/a*=1.5) in the middle of the domain of Fig.4.4 for $\omega\sqrt{a/g}=0.77$. Plots on the free surface of pitch field radiating potential, as calculated by the present BEM.

The details of the diffraction/radiation fields are very well represented, and the effect of the absorbing layer of thickness, equal to two wavelengths, is clearly illustrated by the damping of the waves reaching in the outward limit of the free surface mesh, without significant reflection. In this case the depth around the exterior boundary continuously varies from *h*=1.5, in the deeper water region, to *h*=0.5, in the shallow water region, and thus, application of Sommerfeld–type radiation condition could generate significant contamination of the numerical solution.

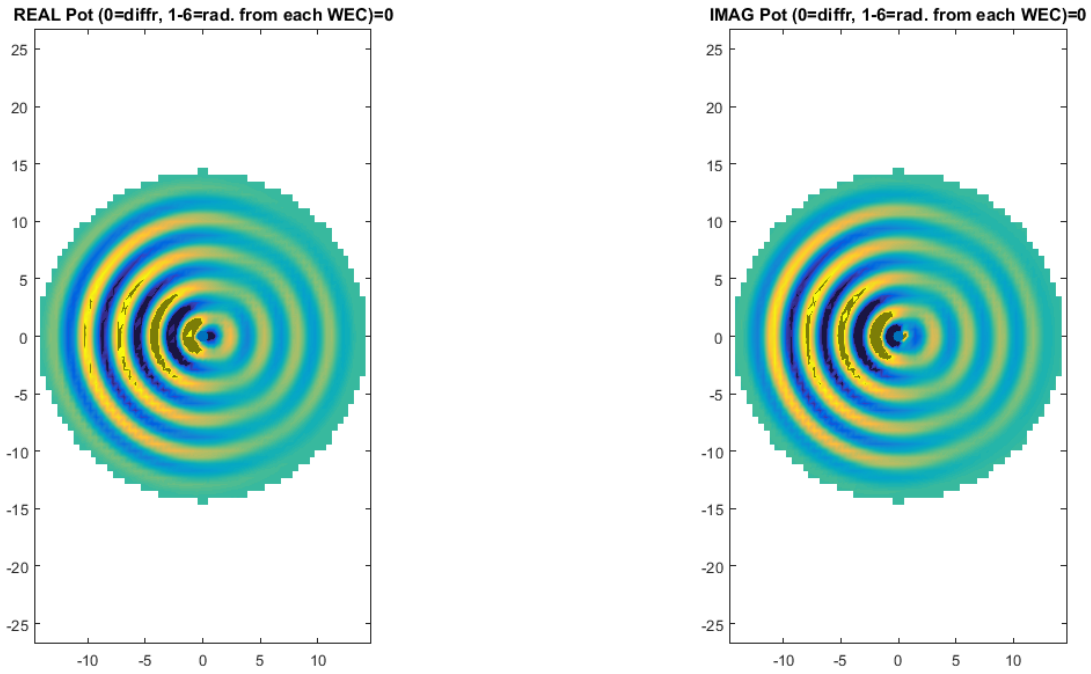

Figure 4.9. Diffraction pattern for a body (like heaving WEC) for the 0deg incident wave conditions in the variable bathymetry region of Fig.4.4 (a).

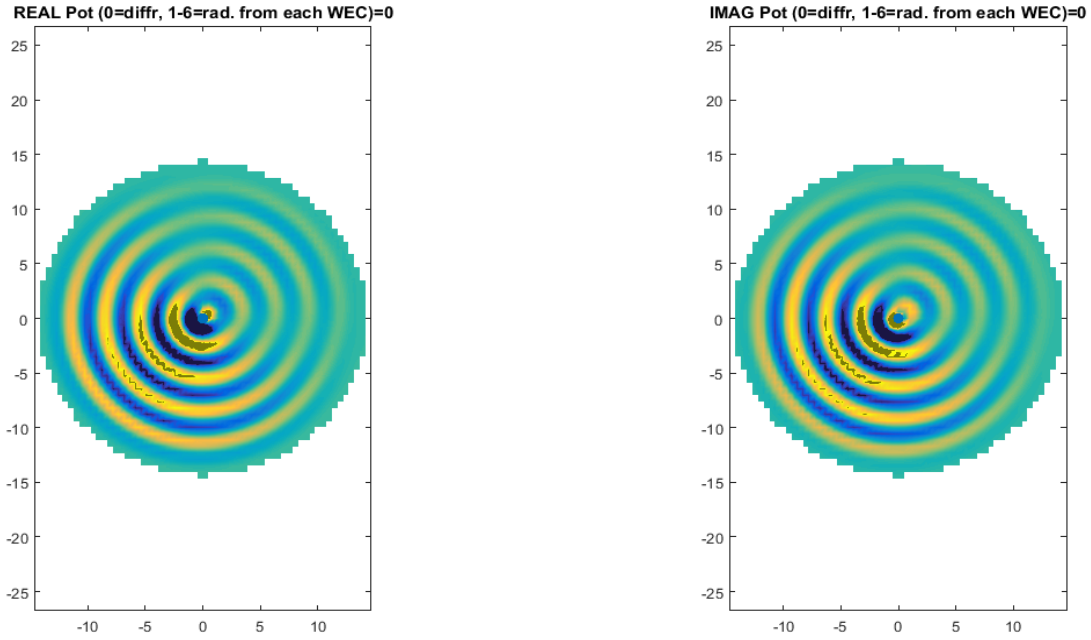

Figure 4.10. Diffraction pattern for a body (like heaving WEC) for the 45deg incident wave conditions in the variable bathymetry region of Fig.4.4 (b).

Conclusions and proposal for future work

In this work a method for evaluating the hydrodynamic analysis of a floating body over a general bathymetry region is presented, calculating the wave power absorption by a single floating body like a WEC (point absorber) and providing useful conclusions about the application of wave energy devices in nearshore and coastal regions.

The present approach is based on the coupled-mode model for the calculation of the wave field propagating over the variable bathymetry region, in conjunction with an optimized absorbing layer model, that treats the conditions at infinity (Radiation condition). The optimization of the absorbing layer is achieved comparing the analytic with the approximate solution, via a low-order Boundary element method , firstly in 2D and then in 3D, providing us a strong tool to face the hydrodynamic analysis in variable bathymetry regions. Numerical results are presented and discussed concerning a simple body (heaving vertical cylinder) in a flat bottom region and in variable bottom region.

Future work is planned towards the detailed study and optimization of the present BEM for WEC arrays extracting energy by combined oscillatory modes, and the development of hybrid techniques to numerically treat the high-frequency part of the spectrum supporting its application to optimal layout of WEC arrays.

REFERENCES

Abramowitz M. Stegun I. A. 1964 Handbook of Mathimatical functions Dover publications inc, New York 486-61272-4

Athanassoulis, G.A., Belibassakis, K.A. 1999. A consistent coupled-mode theory for the propagation of small-amplitude water waves over variable bathymetry regions. *J. Fluid Mechanics* 389: 275-301

Bhatta D. D. 2008 Computations of hydrodynamic coefficients, displacement-amplitude ratios and forces for a floating cylinder due to wave diffraction and radiation Internation Journal of Non-linear mechanics 1027-1041

Beer G.. Ian Smith Duenser C. 2008 The boundary element method with programming for engineers and scientists. Springer Wien New York 978-211-71574-1.

Belibassakis, K.A. 2008. A Boundary Element Method for the hydrodynamic analysis of floating bodies in general bathymetry regions. *Engineering Analysis with Boundary Elements* 32: 796-810.

Belibassakis, K.A. 2015. Power absorption by wave energy converters over variable bottom topography. *Proceedings of the 11th European Wave and Tidal Energy Conference, (EWTEC2015), Nantes, France, 6 – 11 September.*

Belibassakis, K.A., Athanassoulis, G.A., Gerostathis, T. 2001. A coupled-mode system for the refraction-diffraction of linear waves over steep three dimensional topography. *Applied Ocean Res.* 23: 319-336.

Belibassakis, K.A., Athanassoulis, G.A., Gerostathis, Th. 2014. Directional wave spectrum transformation in the presence of strong depth and current inhomogeneities by means of coupled-mode model. *Ocean Engineering* 87: 84–96.

Belibassakis, K.A., Gerostathis, Th., Athanassoulis, G.A., 2011. A coupled-mode model for water wave scattering by horizontal, non-homogeneous current in general bottom topography. *Applied Ocean Research* 33:384– 397.

Belibassakis, G.A., Gerostathis K.A., Athanassoulis, 2016 A 3D-BEM coupled-mode method for WEC arrays in variable 978-1-138-62627-0

Booij, N., R. C. Ris, and L. H. Holthuijsen. 1999. A third-generation wave model for coastal regions, 1. Model description and validation. *J. Geophys. Res.* 104:7649–7666.

Calisal S. Sabuncu T. 1981 Hydrodynamic coefficients for vertical circular cylinders at finite depth Ocean Engineering 0029-8018/81/010025-39

Charrayre, F., Peyrard C., Benoit M., Babarit A. 2014. A coupled methodology for wave body interactions at the scale of a farm of wave energy converters including irregular bathymetry. *Proceedings of the 33th IntConf on Offshore Mechanics and Arctic Engin (OMAE2014). San Francisco, CA, 8 – 13 June*.

Coddington A. Earl Levinson 1972 N. Theory of ordinary differential equations Tata Mcgraw-Hill 110015

Dean G. R. Dalrymple A. R. 1984 Water wave mechanics for engineers and scientists world scientific 9810204213

Drimer, N. Agnon Y., Stiassnie M. 1992. A simplified analytical model for a floating breakwater in water of finite depth, *Applied Ocean Research* 14:33–41.

Ergatoudis I. Irons B. M. Zienkiewicz C. 1968 Curved, isoparametric, Quadrilateral Elements for finite element analysis Solids structures

Gerostathis, T., Belibassakis, K.A., Athanassoulis, G.A. 2008. A coupled-mode model for the transformation of wave spectrum over steep 3d topography. A Parallel-Architecture Implementation. *Journal Offshore Mechanics and Arctic Engineering* 130(1), 011001.

Hess, J. L., and Smith, A. M. 0., "Calculation of Potential Flow About Arbitrary Bodies," Progress in Aeronautical Sciences, vol. 8, pp. 1—138, 1967

Hess, J. L., 1972 "Calculation of Potential Flow About Arbitrary Three-Dimensional Lifting Bodies," Final Technical Report MDC 15679-01, McDonnell Douglas, Long Beach, Calif.,

Katz J and Plotkin A. 2001. *Low speed aerodynamics*. McGraw-Hill.

Kress R.1989 Linear integral equations Springer Verlag Berlin3-540-50616-0

Lee C.H., Newman J.N.. 2004. Computation of wave effects using the panel method. In S. Chakrabarti (ed.), *Numerical Modelling in Fluid-Structure Interaction*, WIT Press.

Magne, R., Belibassakis, K., Herbers, T., Ardhuin, F., O'Reilly, Rey, V. 2007. Evolution of surface gravity waves over a submarine canyon. *J. Geographical Research (JGR Oceans)* 112:C01002.

Mei, C.C. 1983. *The applied dynamics of ocean surface waves.* Second Edition 1996, World Scientific.

Massel, S.1993. Extended refraction-diffraction equations for surface waves. *Coastal Eng* 19:97-126.

Mavrakos S., & Kalofonos A. 1997. Power absorption by arrays of interacting vertical axisymmetric wave-energy devices. *Journal of Offshore Mechanics and Arctic Engineering* 119:244-251.

Mavrakos S., McIver P. 1997. Comparison of methods for computing hydrodynamic characteristics of arrays of wave power devices. *Applied Ocean Research* 19:283-291.

Moran J. 1984 An introduction to the theoretical and computational aerodynamics John Wiley and Sons 0-471-87491-4

Newman, J., 1986, Distributions of sources and normal dipoles over a quadrilateral panel,Journal of Engineering Mathematics 20, 113 – 126

Prenter P. M. 1975. Splines and variational methods, *Wiley-Interscience publication* 0-471-50402-5

Rey V. 1995. A note on the scattering of obliquely incident surface gravity waves by cylindrical obstacles in waters of finite depth. *European Journal of Mechanics B/Fluids* 14(1):207–216.

Sclavounos P., Borgen H. 2004. Seakeeping analysis of a high-speed monohull with a motion control bow hydrofoil. *J. Ship Research* 48(2):77-117.

Sinha A. 2015 Hydrodynamics of arrays of heaving point absorbers Engenharia Naval

Wang C.M. Wang B. 2015 T. Large floating structures Springer 978-981-287-136-7

Wehausen J.V. 1971. The motion of floating bodies. *Ann. Review of Fluid Mechanics* 3:237-268.

Yeung R. 1981. Added mass and damping of a vertical cylinder in finite-depth waters. *Applied Ocean Research* 3:119-133.

Yu Z. Falnes J.1995 State-space modelling of a vertical cylinder in heave Applied ocean research 0141-1187/95/S09

APPENDIX A

QUADRILATERAL ELEMENTS

The corresponding problems on the diffraction and radiation potentials $\Phi_D(x,z)$ and $\Phi_k(x,z), k=1,2...6,$ associated with floating WEC in variable bathymetry, are treated by means of a low-order Boundary Element Method (presented in Chap.3 and 4), based on simple singularity distributions and 4-node quadrilateral boundary elements. Except of the singularity distribution also a keypart of the above BEM is the discretization of the problem's boundary by menas of elements. These may be one-dimensional segments, when we treat 2D problems or two dimensional surface elements when treating 3D problems. In the latter case, the simplest element shapes are trianglular and rectanglular, defined by three or four nodes respectively. The first has rightly become most popular due to the ease with which the subdivision can be succeeded and its efficiency in the approximation of general boundary shapes. The rectangular shape places much greater constraints on these factors but has the advantage to model at first order also curvature effects, in contrast with the triangular element which is usually flat. Both elements present the lowest possible forms of approximation and are of first-order accuracy. The elements are separated in flat and curved elements. Curved boundary elements , as shown in Fig. A.1 help us to ensure continuity of the geometry approximation of the various parts of the boundary. Also, there are elements with more nodes, giving more accuracy in our problem and much complication. See details in Ergatoudis et al (1967)

An obvious improvement is the addition of a number of nodal points along the sides of such elements thus permitting a smaller number of variables to be used for solution of practical problems with a given degree of accuracy. An increase of available parameters associated with an element usually leads to improved accuracy of solution for a given number of parameters representing the whole assembly. It is possible thus to use fewer elements for the solution. As such element have yet to be able to follow prescribed boundaries to a good degree of approximation curved shapes are desirable. This appendix describes the usefulness of the curved quadrilateral elements of low order for use in three-dimensional boundary value problems.

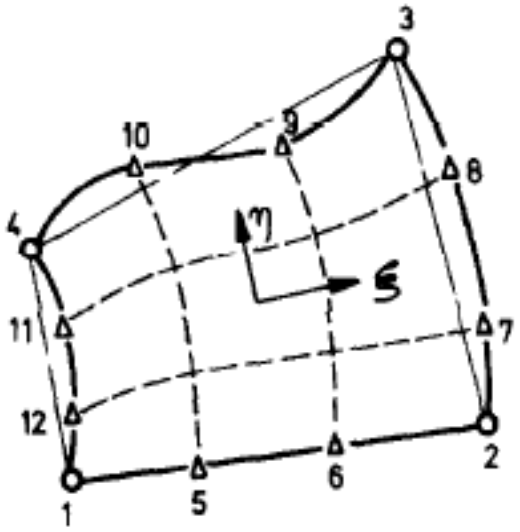

Figure A.1: General quadrilateral element with nodes placed along the sides.

In our problem the geometry approximation of the various parts of the boundary is accomplished by using 4-node curved quadrilateral boundary elements (see Fig.A.2) , ensuring global continuity of the geometry approximation of the various parts of the boundary, and avoiding generation of gaps between element sides. In contrast the constant strength, flat quadrilateral elements introduced by Hess & Smith (1967) commonly used in potential flow problems do not ensure global continuity of the boundary geometry; for more details see Katz & Plotkin (1991, Chapter 10)

In the present work the constant strength, 4-node curved boundary element is used for the approximation of the geometry of the boundary. This is also a low order approximation and does not increase the total number of unknowns (which are the discrete singularity strengths of the boundary elements). A significant benefit of the 4-node elements is that it help us to avoid inter-elemental discontinuity of geometry, and offers better potential approximation, which is a common feature in numerically treating 3D problems with low-order boundary elements.

In addition, the present analysis is based on selecting the surface dipole as the main singularity distribution on the boundary. It is remarked here that the scheme based on using the 4-node curved boundary element and selecting a constant strength dipole distribution as the surface singularity has the following important properties:

(1) The induced potential and velocity from each element can be obtained analytically in all cases of not excessively twisted elements, which however covers most of the cases of interest concerning the examined applications in the present work and ensures a very fast calculation for large discretizations

(2) The self-induced potential and velocity, i.e the induced values from each element to its center (which is used for the collocation points) are very strong, and this guarantees the formation of matrix coefficients that are diagonal dominant for all cases of boundary conditions (Dirichlet, Neumann, mixed-type) which covers all types of boundary conditions encountered in the formulation of the present 3D free-surface problems.

(3) Diagonal dominance of the matrix coefficients offers the possibility to use iterative methods (like Gauss Seidel, see e.g. Press et al 1996) for the solution of the discrete system, which is very important in cases of problems in large domains with variable boundaries (bottom surface, body(ies) wetted surface etc) with fine meshes that are required especially at higher frequencies.

Definition of the 4-node quadrilateral element

We consider intrinsic coordinates (ξ,η) within the boundary element ranging from -1 to 1; see Fig.A2. Using the following formulas a transformation is set up from the rectangle $[-1,1]^2 \subset \mathbb{R}^2$ to the 3D surface patch $\mathbf{x} \in E$, defined as follows:

$$\mathbf{x}(\xi,\eta) = \sum_{n=1}^{L} \mathbf{x}_n N_n(\xi,\eta) \qquad \text{(A.1)}$$

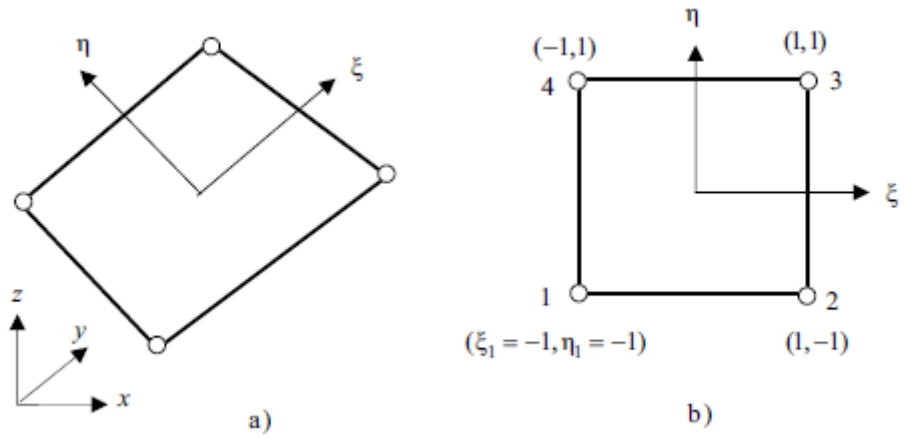

Figure A.2 : 4-node quadrilateral element in a) global and b) local coordinate system.

where $\mathbf{x} = (x, y, z)$ are the Cartesian coordinates of a point with intrinsic coordinates (ξ,η) and $\mathbf{x}_n$ are the coordinates of the element (corner) nodes $n = 1,..4$, numbered as shown in Figure A.2. Furthermore, the (polynomial) shape functions have the following form:

$$N_n = \frac{1}{2}(1+\xi_n\xi)\frac{1}{2}(1+\eta_n\eta) \qquad \text{(A.2)}$$

It is nevertheless possible to use a more direct approach and write by inspection

$$N_1(\xi,\eta)=\frac{1}{4}(1-\xi)(1-\eta) \tag{A.3}$$

$$N_2(\xi,\eta)=\frac{1}{4}(1+\xi)(1-\eta) \tag{A.4}$$

$$N_3(\xi,\eta)=\frac{1}{4}(1+\xi)(1+\eta) \tag{A.5}$$

$$N_4(\xi,\eta)=\frac{1}{4}(1-\xi)(1+\eta) \tag{A.6}$$

As an example, the shape function $N_1(\xi,\eta)$ is shown in Fig. A.3. It describes a curved surface consisting of straight lines in the ξ,η directions. The surface, also called a hyper-surface, has been a widely used shape for concrete shells, because the formwork is simple to construct.

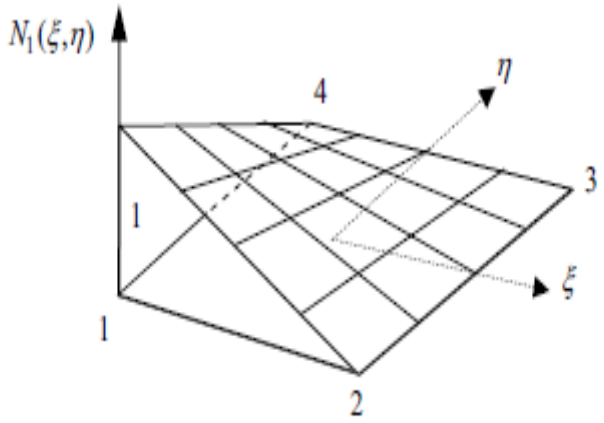

Figure A.3: 4-node quadrilateral element shape function $N_1(\xi,\eta)$ connected with node 1.

In order to evaluate the integrals, it is important to calculate the elements centroid and the tangent vectors parallel to ξ and η direction. These are obtained as follows

$$C_0=\frac{1}{4}(\mathbf{x}_1+\mathbf{x}_2+\mathbf{x}_3+\mathbf{x}_4) \tag{A.7}$$

$$\mathbf{e}_\xi=\frac{\partial\mathbf{x}}{\partial\xi}=\sum_{i=1}^{4}\frac{\partial N_i(\xi,\eta)}{\partial\xi}\mathbf{x}_i \tag{A.8}$$

$$\mathbf{e}_\eta=\frac{\partial\mathbf{x}}{\partial\eta}=\sum_{i=1}^{4}\frac{\partial N_i(\xi,\eta)}{\partial\eta}\mathbf{x}_i \tag{A.9}$$

Integration of a function $f(\mathbf{x}(\xi,\eta))$ on the element is then defined as follows

$$\int_E f\,dS=4\cdot\int_{\eta=-1}^{\eta=1}\int_{\xi=-1}^{\xi=1} f(\mathbf{x}(\xi,\eta))\sqrt{\alpha(\xi,\eta)}\,d\xi d\eta \tag{A.10}$$

where

$$\sqrt{\alpha}=\left\|\mathbf{e}_\xi\times\mathbf{e}_\eta\right\| \tag{A.11}$$

is the metric tensor determinant (Jacobian of the transformation), and also

$$\mathbf{n} = \left(\mathbf{e}_\xi \times \mathbf{e}_\eta\right) / \left\|\mathbf{e}_\xi \times \mathbf{e}_\eta\right\| = \left(\mathbf{e}_\xi \times \mathbf{e}_\eta\right) / \sqrt{\alpha} \tag{A.12}$$

is the unit normal vector on the quadrilateral element. Using the above definitions we are able to calculate induced potential from a constant (normal) dipole distribution on the quadrilateral element as described below.

We assume that every quadrilateral element has constant doublet distribution μ. Using the doublet element which points in the z-direction the velocity potential can be obtained by integrating the point elements:

$$\Phi(x, y, z) = -\mu \int_S \mathbf{n} \, \nabla G(x; x_0) \, dS \tag{A.13}$$

$$4\pi G(\mathbf{x}; \mathbf{x}_0) = \left[(x - x_0)^2 + (y - y_0)^2 + (z - z_0)^2 \right]^{1/2} \tag{A.14}$$

In the special case when the 4 nodes of the quadrilateral element lie on the same plane the velocity potential can be obtained by the following integral:

$$\Phi(x, y, z) = \frac{-\mu}{4\pi} \int_S \frac{z \, dS}{\left[(x - x_0)^2 + (y - y_0)^2 + z^2 \right]^{1/2}} \tag{A.15}$$

Evaluation of Induced Velocity over a quadrilateral boundary element

From Katz & Plotkin (1991), we know that the three-dimensional constant –strength doublet element is equivalent to a constant-strength vortex ring that is placed at the panel edges; see Figure A.4. The proof of the above theorem is repeated below from Katz & Plotkins (1991, Chapter 10).

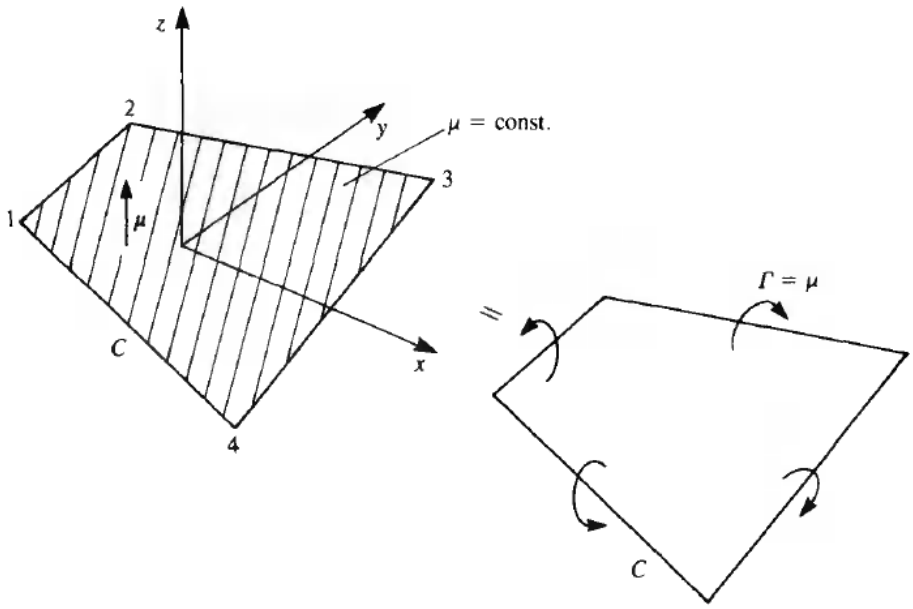

Figure A.4 : Quadrilateral doublet element and its vortex ring equivalent.

Proof of constant doublet panel equivalence to vortex ring

Consider the doublet panel of the above figure with constant strength μ. The induced potential can be written as

$$\Phi = -\frac{\mu}{4\pi}\int_S \frac{z\,dS}{r^3} \tag{A.16}$$

where $r = \sqrt{(x-x_0)^2 + (y-y_0)^2 + z^2}$. Moreover, the corresponding induced velocity is

$$q = \nabla\Phi = -\frac{\mu}{4\pi}\int_S \nabla\frac{z}{r^3}\,dS = \frac{\mu}{4\pi}\int_S \left[i\frac{\partial}{\partial x_0}\frac{z}{r^3} + j\frac{\partial}{\partial y_0}\frac{z}{r^3} + k\left(\frac{1}{r^3} - \frac{3z}{r^5}\right)\right] dS \tag{A.17}$$

where we have used

$$\frac{\partial}{\partial x}\frac{1}{r^3} = -\frac{\partial}{\partial x_0}\frac{1}{r^3}, \qquad \frac{\partial}{\partial y}\frac{1}{r^3} = -\frac{\partial}{\partial y_0}\frac{1}{r^3} \tag{A.18}$$

Now, let C represent the curve surrounding the panel in the above figure and consider a vortex filament of circulation Γ along C. The velocity due to the filament is obtained from the Biot-Savart law (Katz & Plotkin 1991), as follows

$$q = \frac{\Gamma}{4\pi}\int_C \frac{\mathbf{dl}\times\mathbf{r}}{r^3} \tag{A.19}$$

and for $\mathbf{dl} = (dx_0, dy_0)$ and $\mathbf{r} = (x-x_0, y-y_0, z)$ we get

$$q = \int_C \left\{ i\frac{z}{r^3}dy_0 - j\frac{z}{r^3}dx_0 + k\left[(y-y_0)dx_0 - (x-x_0)dy_0\right]\right\} \tag{A.20}$$

Furthermore, the Stokes theorem for the vector $\vec{A}$ is

$$\oint_C \mathbf{A}\cdot\mathbf{dl} = \int_S \mathbf{n}\cdot\nabla\times\mathbf{A}\; dS \tag{A.21}$$

Using the above theorem with $\mathbf{n}=\hat{\mathbf{k}}$ this becomes

$$\oint_C \mathbf{A}\cdot\mathbf{dl} = \int_S \left(\frac{\partial A_y}{\partial x_0} - \frac{\partial A_x}{\partial y_0}\right) dS \tag{A.22}$$

Using Stokes' theorem on the above velocity integral we get

$$q = \frac{\Gamma}{4\pi}\int_S \left[\hat{i}\,\frac{\partial}{\partial x_0}\frac{z}{r^3} + \hat{j}\,\frac{\partial}{\partial y_0}\frac{z}{r^3} - \hat{k}\left(\frac{\partial}{\partial x_0}\frac{x-x_0}{r^3} + \frac{\partial}{\partial y_0}\frac{y-y_0}{r^3}\right)\right] dS \tag{A.23}$$

Once the differentiation is performed, it is seen that the velocity of the filament is identical to the velocity of the doublet panel if $\Gamma = \mu$. We conclude this part by noticing that, as shown by Hess (1972) , the above holds also true in the case of the twisted 4-node quadrilateral element.

Evaluation of the induced velocity

Therefore, the above formulas for the velocity potential and its derivatives are valid for twisted panels as well. In order to evaluate induced velocities, we make use of this theorem. Consider one side of the element and a point P in the space as in the fig. A.5.

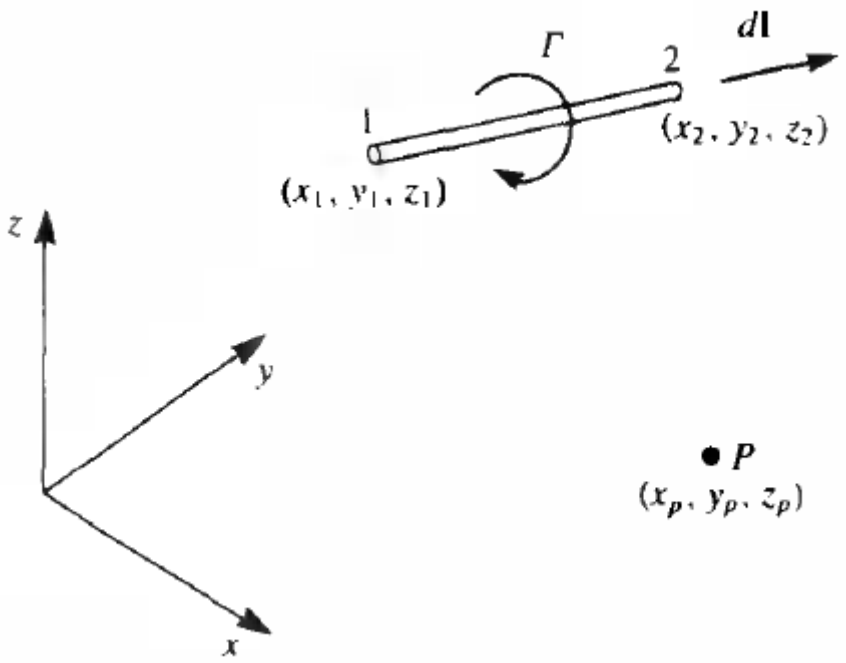

Figure A.5 : Influence of a straight vortex line segment to a point P.

The velocity induced by such a vortex segment of circulation Γ states

$$\Delta q = \frac{\Gamma}{4\pi}\frac{\mathbf{dl}\times\mathbf{r}}{r^3} \tag{A.24}$$

If the vortex points from 1 to point 2, then the velocity at an arbitrary point P can be obtained by the equation below

$$q_{1,2} = \frac{\Gamma}{4\pi}\frac{\boldsymbol{r}_1\times\boldsymbol{r}_2}{\left|\boldsymbol{r}_1\times\boldsymbol{r}_2\right|^2} r_0 \cdot \left(\frac{\boldsymbol{r}_1}{r_1}-\frac{\boldsymbol{r}_2}{r_2}\right) \tag{A.25}$$

For the numerical computation in a Cartesian system where the (x, y, z) values of the points 1,2 and P are given, the velocity can be calculated by the following steps:

1. Calculate $\boldsymbol{r}_1\times\boldsymbol{r}_2$:

$$\left(\boldsymbol{r}_1\times\boldsymbol{r}_2\right)_x = \left(y_P-y_1\right)\left(z_P-z_2\right)-\left(z_P-z_1\right)\left(y_P-y_2\right) \tag{A.26}$$

$$\left(\boldsymbol{r}_1\times\boldsymbol{r}_2\right)_y = -\left(x_P-x_1\right)\left(z_P-z_2\right)-\left(z_P-z_1\right)\left(x_P-x_2\right) \tag{A.27}$$

$$\left(\boldsymbol{r}_1\times\boldsymbol{r}_2\right)_z = \left(x_P-x_1\right)\left(y_P-y_2\right)-\left(y_P-y_1\right)\left(x_P-x_2\right) \tag{A.28}$$

   Also, the absolute value of this vector product is

$$\left|\boldsymbol{r}_1\times\boldsymbol{r}_2\right|^2 = \left(\boldsymbol{r}_1\times\boldsymbol{r}_2\right)_x^2+\left(\boldsymbol{r}_1\times\boldsymbol{r}_2\right)_y^2+\left(\boldsymbol{r}_1\times\boldsymbol{r}_2\right)_z^2 \tag{A.29}$$

2. Calculate the distances r_1, r_2:

$$r_1 = \sqrt{\left(x_P-x_1\right)^2+\left(y_P-y_1\right)^2+\left(z_P-z_1\right)^2} \tag{A.30}$$

$$r_2 = \sqrt{\left(x_P-x_2\right)^2+\left(y_P-y_2\right)^2+\left(z_P-z_2\right)^2} \tag{A.31}$$

3. Check for singular conditions.(Since the vortex solution is singular when the point P lies on the vortex. Then a special treatment is needed in the vicinity of the vortex segment-which for numerical purposes is assumed to have a very small radius $\in$)

   $$\text{in the case when } \left(r_1,\ or\ r_2, or \left|\boldsymbol{r}_1\times\boldsymbol{r}_2\right|^2 < \in\right)$$

   where $\in$ is the vortex core size(which can be as small as the truncation error)

   $$\text{then } \left(u=\upsilon=w=0\right)$$

   or else u, υ, w can be estimated by assuming solid body rotation or any other (more elaborate) vortex core model

4. Calculate the inner-product:

$$\boldsymbol{r}_0\cdot\boldsymbol{r}_1 = \left(x_2-x_1\right)\left(x_P-x_1\right)+\left(y_2-y_1\right)\left(y_P-y_1\right)+\left(z_2-z_1\right)\left(z_P-z_1\right) \tag{A.32}$$

$$\boldsymbol{r}_0 \cdot \boldsymbol{r}_2 = (x_2 - x_1)(x_P - x_2) + (y_2 - y_1)(y_P - y_2) + (z_2 - z_1)(z_P - z_2) \tag{A.33}$$

5. The resulting velocity components are

$$u = K(\boldsymbol{r}_1 \times \boldsymbol{r}_2)_x \tag{A.34}$$

$$\upsilon = K(\boldsymbol{r}_1 \times \boldsymbol{r}_2)_y \tag{A.35}$$

$$w = K(\boldsymbol{r}_1 \times \boldsymbol{r}_2)_z \tag{A.36}$$

where

$$K = \frac{\Gamma}{4\pi |\boldsymbol{r}_1 \times \boldsymbol{r}_2|^2} \left(\frac{\boldsymbol{r}_0 \cdot \boldsymbol{r}_1}{r_1} - \frac{\boldsymbol{r}_0 \cdot \boldsymbol{r}_2}{r_2} \right) \tag{A.37}$$

This procedure must be done for each vortex segment at the edge of the 4-node element and the calculated induced velocities from each segment have to be summed, in order to obtain the induced velocity of the boundary element to every point in the domain.

Evaluation of the induced potential from constant strength 4-node quadrilateral element

Having completed the induced velocity calcuation, we follow Newman (1986), for the evaluation of the induced potential from each 4-node quadrilateral boundary element at every point in the domain. In particular, we evaluate the potential, which is induced from a quadrilateral element with constant distribution of doublet ($\mu = const$) to an arbitrary field point P with coordinates (x, y, z), as shown in Fig.A.6. In order to find the induced potential, we evaluate the following integral (note that the negative sign of Eq.A.6 may be considered absorbed in the value of μ)

$$\Phi_\mu = \frac{\mu}{4\pi} \int_E \vec{n}_Q \frac{(\mathbf{x}_P - \mathbf{x}_Q)}{r^3} dS(Q) \tag{A.38}$$

where

E: Quadrilateral element's area

$\mathbf{n}_Q$: normal vector at the center of the element

$\mathbf{x}_P$: The vector from the start of the axis to the field point P

$\mathbf{x}_Q$: The vector from each point $Q \in E$, which is an arbitrary point of the element

In our case, we consider $\mu = 1$. If we consider a sink at the field point P, with unit strength $\sigma = -1$, then we observe that the sink flow is equal to U.

$$U_r = -\frac{1}{4\pi r^2} \qquad U_\sigma = -\frac{1}{4\pi}\frac{\mathbf{x}_Q - \mathbf{x}_P}{r^3} \tag{A.39}$$

Now, if we consider a sink at point P and evaluate the sink flow rate through E, we observe that the integral is exactly the same as in our case, of the dipole constant distribution, i.e.

$$Q(\mathbf{U}_\sigma \mid E) = -\frac{1}{4\pi}\int_{\mathrm{E}} \mathbf{n}_Q \frac{\mathbf{x}_Q - \mathbf{x}_P}{r^3} dS_Q \equiv \Phi_\mu$$

(A.40)

However, the sink flow rate through the element's area is equal to the flow rate through a sphere with unit radius $r_0 = 1$ and center the field point P, which is easily calculated to be

$$\Phi_\mu = \int_{\Sigma(x=x_P|=r_0)} U_\sigma d\Sigma = -\frac{1}{4\pi}\int_\Sigma r_0^{-2} d\Sigma = -\frac{a}{4\pi} \to \pm\frac{a}{4\pi} \tag{A.41}$$

where a is the solid angle of the element. In our case we separate the quadrilateral element in two three-node elements, as it is shown in fig.A.7 and we evaluate the solid angle by means of the corresponding angles of the two tetrahedral and then simply we sum the potentials.

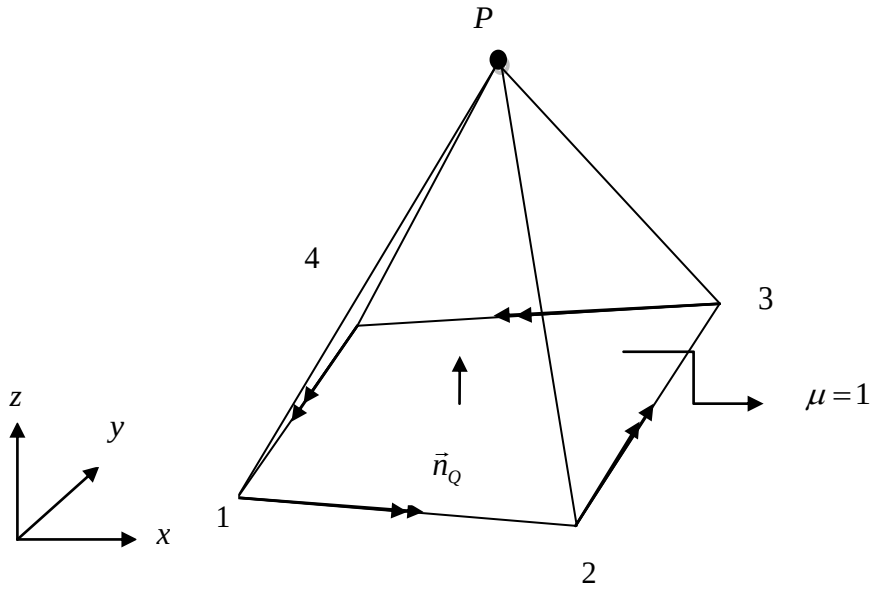

Figure A.6: Influenced of a curved quadrilateral element to an arbitrary field point P.

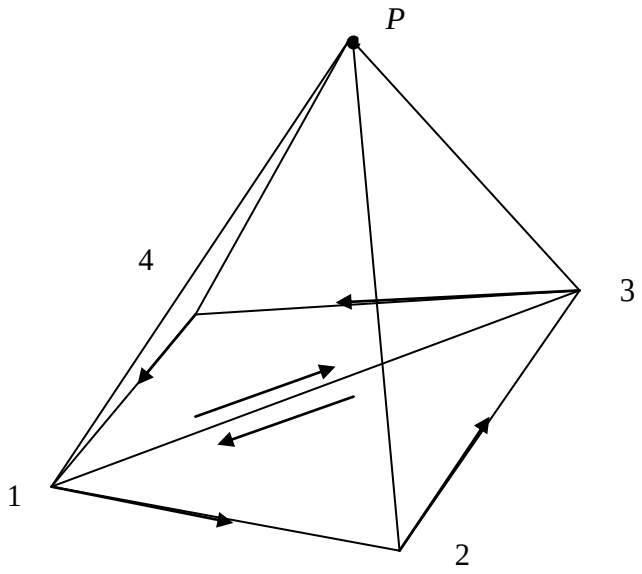

Figure A.7 : Quadrilateral element separation in 2 three-node elements.

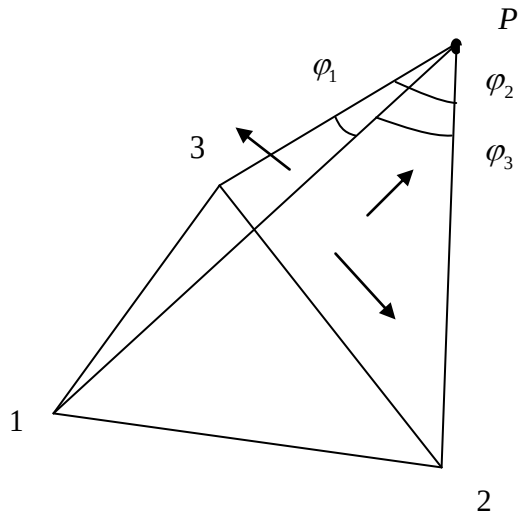

Figure A.8: Solid angle of a tetrahedron.

In particular, the solid angle for a tetrahedron is given by the following equation

$$a = 2\pi - \varphi_1 - \varphi_2 - \varphi_3 \qquad \text{(A.42)}$$

where $\varphi_1, \varphi_2, \varphi_3$ are shown in Figure A.8.

Consequently, the induced potential from a quadrilateral element with unit singularity distribution to a field point P is given by the following equation

$$\Phi = \Phi_1 + \Phi_2 = \frac{a_1}{4\pi} + \frac{a_2}{4\pi} \tag{A.43}$$

where α_1 is the solid angle for the first three-node element and a_2 is the solid angle for the second three-node element.

Examples

Subsequently, some figures are quoted, showing the induced potential and velocity from a quadrilateral element with unit singularity distribution depending on the location of the field point P.

In the first case, we consider a curved quadrilateral element presented in Fig.A.9 with coordinates Q_1=(-1,-1,-0.1), Q_2=(1,-0.5,0.1), Q_3=(2,-0.5,0.3), Q_4=(-0.5,0.8,0), and the induced potential and velocity are evaluated to a field point at a line, normal to the element passing through the element center, as it is shown in Fig. A.9. Then the induced potential and velocity as calculated by the present method are presented. Having obtained the induced potential along the line (passing through the center of the element in Fig.A.9 with direction the normal of the element) we are able to differentiate the potential alonmg the line ans estimate the induced velocity. Then, we are able to present a comparison between the potential's and velocity's methods as shown in Fig. A.10.

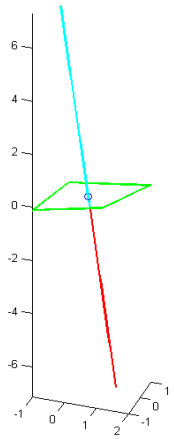

Figure A.9: Quadrilateral element and a line normal to the element, passing through its centroid.

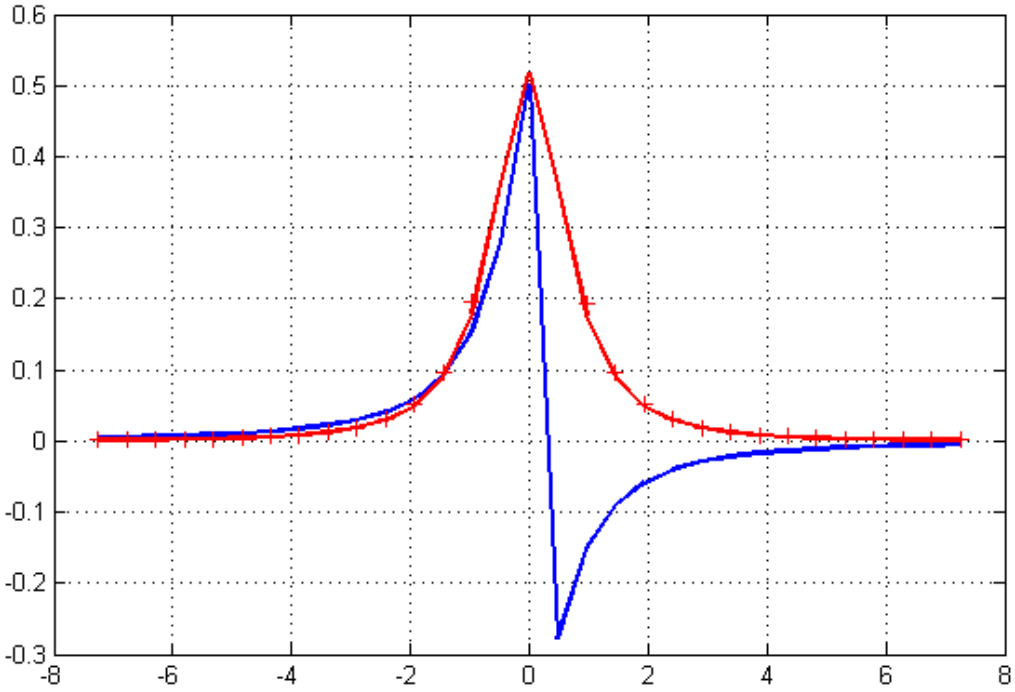

Figure A.10: Comparison between velocity and potential methods.

The blue line represents the potential's value along the line passing through the center of the element parametrized with respect to the physical distance from the center of the quadrilateral element, as calculated using (A.43). As it was expected the potential and the velocity are maximized at the element's center. We clearly observe the jump of the value of the induced potential (from +0.5 to -0.5) as we pass through the center of the element which is a well known property of surface doublet distributions. The red line represents the induced velocity, from Biot-Savart rule applied to the equivalent vortex ring. The differentiated potential along the line calculated by using second-order finite differences is shown by using crosses. We see that the velocity's results are identical, verifying the correctness of our calculations.

As a second example for the same element we consider induced potential and velocity along another line which does not crosses the element and is almost parallel to its surface; see Fig. A.11. In this case we observe that there is no discontibuity of the potential distribution along the line as it ought since it does not cress the element. However the agreement between the velocity obtained by differentiating the induced potential and the calculation based on the vortex ring is again very good verifying the calculation scheme. The potential is maximized again in the nearest to the center field point, but it has lower value.

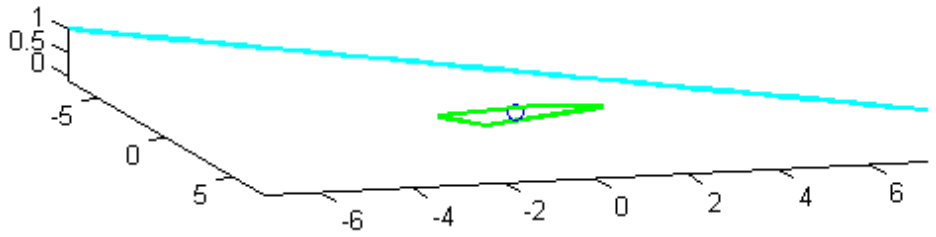

Figure A.11: Quadrilateral element and a line almost parallel to the element.

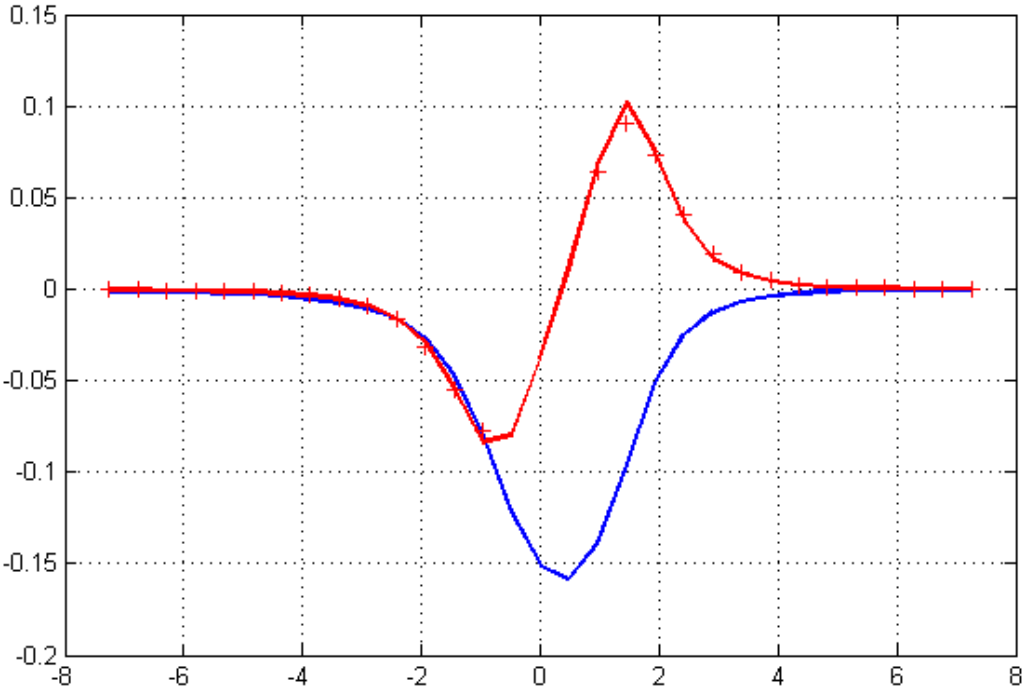

Figure A.12: Comparison between velocity and potential methods.

APPENDIX B

THE COUPLED-MODE MODEL FOR PROPAGATION OF WATER WAVES IN VARIABLE BATHYMETRY REGIONS

In Chapters 3 and 4 of this thesis a 3D hybrid boundary element – absorbing layer method is developed and studied concerning the hydrodynamic analysis of floating bodies in constant-depth and variable bathymetry regions, respectively. In both these cases, for the solution of the diffraction potential and the calculation of the Froude-Krylov and the diffraction forces, it is necessary to calculate the incident-propagating wave potential without the presence of the body. In the case of flat seabed the wave potential is analytically known from the linearized theory (e.g., Dean & Dalrymple 1991), as follows

$$\Phi(x,z;t) = \mathrm{Re}\left(\frac{igH}{2\omega} \varphi(x,z) e^{-i\omega t} \right)$$

where H is the waveheight, ω is the angular frequency, and the complex wave potential is given by

$$\varphi(x,z) = \exp\left(ik_0 x\right) \frac{\cosh\left(k_0 (z+h)\right)}{\cosh\left(k_0 h\right)}$$

where the wavenumber k_0 is obtained from the dispersion relation, Eq.(2.6), formulated at the depth h. However, in the case of variable bottom topography, as the water strip shown in Fig.B.1 joining two subregions of constant, but different depth, the wave potential is not known and must be calculated by suitable numerical method, as the coupled-mode model by Athanassoulis & Belibassakis (1999), which is described below.

Formulation of the problem

The studied marine environment consists of a water layer bounded above by the free surface and below by a rigid bottom as is shown in fig. B.1.

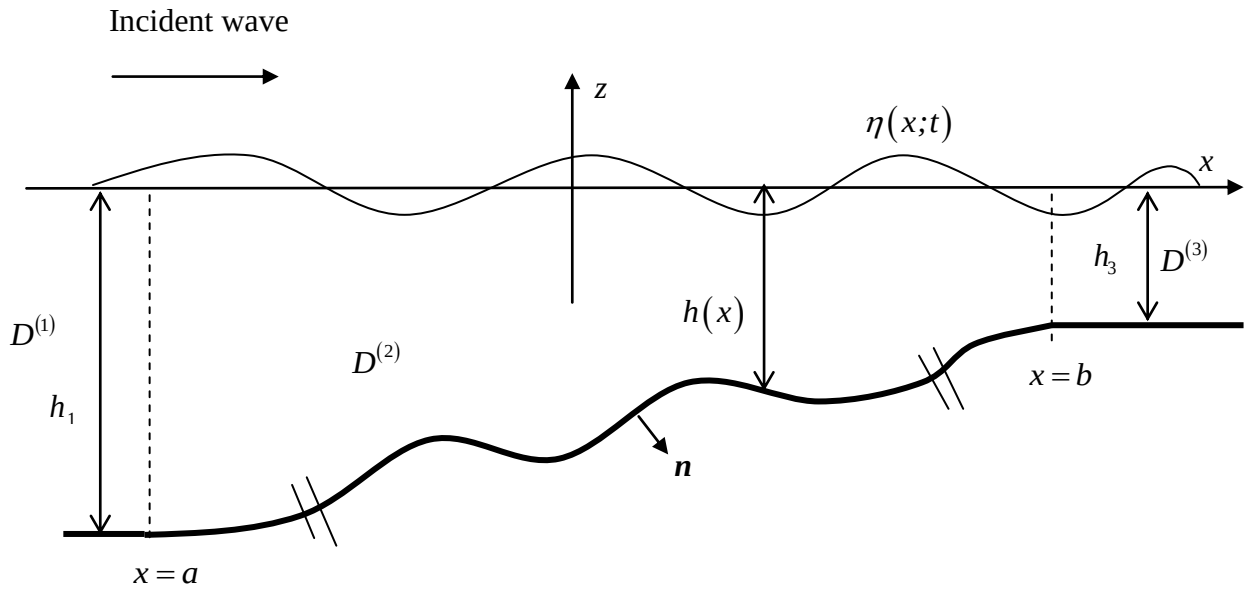

Figure B.1: Domain decomposition and basic notation.

It is assumed that the bottom slope exhibits an arbitrary one dimensional variation in a subdomain of finite length, i.e. the bathymetry is characterised by parallel, straight bottom contours lying between two regions of constant but different depth. Before proceeding to the formulation of the problem we shall introduce some geometrical notation. A Cartesian coordinate system is introduced, with its origin at some point on the mean water level (in the variable bathymetry region), the z-axis pointing upwards and the y-axis being parallel to the bottom contours. The domain D_{3D} is represented by $D_{3D} = D \times R$, where D is the (two-dimensional) intersection of D_{3D} by a vertical plane perpendicular to the bottom contours, and $R = (-\infty, +\infty)$ is a copy of the real line. To make the notation clear we explicitly write the analytical definitions of both the three-dimensional liquid domain D_{3D} and the two-dimensional vertical intersection D:

$$D_{3D} = \left\{(x,y,z):\ (x,y) \in R^2, -h(x) < z < 0\right\}, \qquad D = \left\{(x,z):\ x \in R, -h(x) < z < 0\right\}. \tag{B.1}$$

The liquid domain D_{3D} is decomposed in three subdomains $D_{3D}^{(i)} = D^{(i)} \times R, \quad i = 1,2,3,$ defined as follows: $D_{3D}^{(1)}$ is the constant-depth subdomain characterised by $x < a$, $D_{3D}^{(3)}$ is the constant-depth subdomain characterised by $x > b$, and $D_{3D}^{(2)}$ is the variable bathymetry

subdomain lying between $D_{3D}^{(1)}$ and $D_{3D}^{(3)}$. The analytic definitions of the corresponding two-dimensional subdomains $D^{(i)}$, $i=1,2,3,$ are as follows:

$$D^{(i)}=\left\{(x,z):\quad \begin{bmatrix} x<a, & -h_1<z<0\,, & \text{for } i=1 \\ a<x<b, & -h(x)<z<0, & \text{for } i=2 \\ x>b\,, & -h_3<z<0, & \text{for } i=3 \end{bmatrix}\right\} \tag{B.2}$$

After introducing the geometrical notation we need, we are proceeding to the mathematical formulation of the wave problem. The general representation of the wave potential $\varphi(x,z)$ in the semi-infinite strips $D^{(1)}$ and $D^{(3)}$ (see, e.g., Miles 1967, Mei & Black 1969, Massel 1993):

$$\varphi^{(1)}(x,z)=\left(A_0\exp\left(ik_0^{(1)}x\right)+A_R\exp\left(-ik_0^{(1)}x\right)\right)Z_0^{(1)}(z)+\sum_{n=1}^{\infty}C_n^{(1)}Z_n^{(1)}(z)\exp\left(k_n^{(1)}(x-a)\right)$$

$$(x,z)\in D^{(1)} \tag{B.3}$$

$$\varphi^{(3)}(x,z)=A_T\exp\left(ik_0^{(3)}x\right)Z_0^{(3)}(z)+\sum_{n=1}^{\infty}C_n^{(3)}Z_n^{(3)}(z)\exp\left(k_n^{(3)}(b-x)\right),\quad (x,z)\in D^{(2)}\ , \tag{B.4}$$

The terms $\left(A_0\exp\left(ik_0^{(1)}x\right)+A_R\exp\left(-ik_0^{(1)}x\right)\right)Z_0^{(1)}(z)$ and $A_T\exp\left(ik_0^{(3)}x\right)Z_0^{(3)}(z)$ in the series (B.3) and (B.4), respectively, are the *propagating modes*, while the remaining ones $(n=1,2,\ldots)$ are the *evanescent modes*. In the expansions (B.3) and (B.4) the sets of numbers $\left\{ik_0^{(i)},k_n^{(i)},\ n=1,2,\ldots\right\}$, $i=1,3,$ and the sets of vertical functions $\left\{Z_n^{(i)}(z),\ n=0,1,2,\ldots\right\}$, $i=1,3$, are, respectively, the eigenvalues and the corresponding eigenfunctions of the following regular Sturm-Liouville problems obtained by separation of variables in the half-strips $D^{(i)}$, $i=1,3$. The eigenvalues $\left\{ik_0^{(i)},k_n^{(i)}\right\}$ are obtained as the roots of the dispersion relations

$$\mu h_i=-k^{(i)}h_i\tan\left(k^{(i)}h_i\right),\qquad i=1,3, \tag{B.6}$$

and the eigenfunctions $\left\{Z_n^{(i)}(z),\ n=0,1,2,\ldots\right\}$ are given by

$$Z_0^{(i)}(z)=\frac{\cosh\left(k_0^{(i)}\left(z+h_i\right)\right)}{\cosh\left(k_0^{(i)}h_i\right)},\qquad Z_n^{(i)}(z)=\frac{\cos\left(k_n^{(i)}\left(z+h_i\right)\right)}{\cos\left(k_n^{(i)}h_i\right)},\quad n=1,2,\ldots,\quad i=1,3. \tag{B.7}$$

The following problem can be equivalently reformulated as a transmission boundary value problem in the bounded subdomain $D^{(2)}$ and the function $\varphi^{(2)}(x,z)$, defined in $D^{(2)}$, satisfy the following system of equations, boundary and matching conditions:

$$\nabla^2\varphi^{(2)} = 0, \qquad (x,z) \in D^{(2)}, \tag{B.8a}$$

$$\frac{\partial\varphi^{(2)}}{\partial n^{(2)}} - \mu\varphi^{(2)} = 0, \quad (x,z) \in \partial D_F^{(2)}, \qquad \frac{\partial\varphi^{(2)}}{\partial n^{(2)}} = 0, \quad (x,z) \in \partial D_H^{(2)}, \tag{B.8.b,c}$$

$$\varphi^{(2)} = \varphi^{(1)}, \quad \frac{\partial\varphi^{(2)}}{\partial n^{(2)}} = -\frac{\partial\varphi^{(1)}}{\partial n^{(1)}}, \quad (x,z) \in \partial D_I^{(12)}, \tag{B.8.d,e}$$

$$\varphi^{(2)} = \varphi^{(3)}, \quad \frac{\partial\varphi^{(2)}}{\partial n^{(2)}} = -\frac{\partial\varphi^{(3)}}{\partial n^{(3)}}, \quad (x,z) \in \partial D_I^{(23)}, \tag{B.8.f,g}$$

After admitting a variational formulation in this transmission problem and using an additional mode, the wave potential representation is enhanced. The variational formulation of the problem is stated as follows (see Athanassoulis & Belibassakis 1999):

$$\begin{aligned}
&-\int_{D^{(2)}} \left(\nabla^2\varphi^{(2)}\right)\delta\varphi^{(2)}dV + \int_{\partial D_H^{(2)}} \left(\frac{\partial\varphi^{(2)}}{\partial n^{(2)}}\right)\delta\varphi^{(2)}dS + \int_{\partial D_F^{(2)}} \left(\frac{\partial\varphi^{(2)}}{\partial n^{(2)}} - \mu\varphi^{(2)}\right)\delta\varphi^{(2)}dS + \\
&+\int_{\partial D_I^{(12)}} \left(\frac{\partial\varphi^{(2)}}{\partial n^{(2)}} + \frac{\partial\varphi^{(1)}}{\partial n^{(1)}}\right)\delta\varphi^{(2)}dS + \int_{\partial D_I^{(23)}} \left(\frac{\partial\varphi^{(2)}}{\partial n^{(2)}} + \frac{\partial\varphi^{(3)}}{\partial n^{(3)}}\right)\delta\varphi^{(2)}dS + \\
&+\int_{\partial D_I^{(12)}} \left(\varphi^{(2)} - \varphi^{(1)}\right)\delta\left(\frac{\partial\varphi^{(1)}}{\partial x}\right)dS - \int_{\partial D_I^{(23)}} \left(\varphi^{(2)} - \varphi^{(3)}\right)\delta\left(\frac{\partial\varphi^{(3)}}{\partial x}\right)dS = 0.
\end{aligned} \tag{B.9}$$

Enhanced local-mode representation

The wave potential $\varphi^{(2)}(\mathbf{x},z)$ associated with the propagation of water waves in the variable bathymetry region, without the presence of the scatterer (floating body), can be conveniently calculated by means of the consistent coupled-mode model. This model is based on the following enhanced local-mode representation:

$$\varphi^{(2)}(\mathbf{x},z) = \varphi_{-1}(\mathbf{x})Z_{-1}(z;\mathbf{x}) + \sum_{n=0}^{\infty}\varphi_n(\mathbf{x})Z_n(z;\mathbf{x}). \tag{B.10}$$

In the above expansion, the term $\varphi_0(\mathbf{x})Z_0(z;\mathbf{x})$ denotes the propagating mode of the generalised incident field. The remaining terms $\varphi_n(\mathbf{x})Z_n(z;\mathbf{x})$, $n=1,2,\ldots,$ are the

corresponding evanescent modes, and the additional term $\varphi_{-1}(\mathbf{x})Z_{-1}(z;\mathbf{x})$ is a correction term, called the sloping-bottom mode, which properly accounts for the satisfaction of the Neumann bottom boundary condition on the non-horizontal parts of the bottom. The function $Z_n(z;\mathbf{x})$ represents the vertical structure of the n-th mode. The function $\varphi_n(\mathbf{x})$ describes the horizontal pattern of the n-th mode and is called the complex amplitude of the n-th mode. The functions $Z_n(z;\mathbf{x})$, $n=0,1,2...$, are obtained as the eigenfunctions of local vertical Sturm-Liouville problems formulated in the local vertical intervals $-h(\mathbf{x})\le z\le 0$, and are given by,

$$Z_0(z;\mathbf{x})=\frac{\cosh\left[k_0(\mathbf{x})\left(z+h(\mathbf{x})\right)\right]}{\cosh\left(k_0(\mathbf{x})\,h(\mathbf{x})\right)},\quad Z_n(z;\mathbf{x})=\frac{\cos\left[k_n(\mathbf{x})\left(z+h(\mathbf{x})\right)\right]}{\cos\left(k_n(\mathbf{x})\,h(\mathbf{x})\right)},\quad n=1,2,\ldots \quad \text{(B.12a)}$$

In the above equations the eigenvalues $\left\{ik_0(\mathbf{x}),k_n(\mathbf{x})\right\}$ are obtained as the roots of the local dispersion relations,

$$\mu h(\mathbf{x})=k_0(\mathbf{x})h(\mathbf{x})\tanh\left[k_0(\mathbf{x})h(\mathbf{x})\right],\ \mu h(\mathbf{x})=-k_n(\mathbf{x})h(\mathbf{x})\ \tan\left[k_n(\mathbf{x})h(\mathbf{x})\right].\quad n=1,2,... \quad \text{(B12b)}$$

The function $Z_{-1}(z;\mathbf{x})$ is defined as the vertical structure of the sloping-bottom mode. This term is introduced in the series in order to consistently satisfy the Neumann boundary condition on the non-horizontal parts of the seabed. This satisfaction is important for the problem, ensuring the conservation of energy. In this model the convenient form of $Z_{-1}(z;\mathbf{x})$, being based on the least degree polynomial satisfying conditions, that is chosen is the following:

$$Z_{-1}(z;x)=h(x)\left[\left(\frac{z}{h(x)}\right)^3+\left(\frac{z}{h(x)}\right)^2\right]. \quad \text{(B.12c)}$$

By using the ;local=mode series expansion (B.10) in the variational equation (B.9), the coupled-mode system of horizontal equations for the amplitudes of the incident wave field propagating over the variable bathymetry region is finally obtained,

$$\sum_{n=-1}^{\infty}a_{mn}(x)\varphi_n''(x)+b_{mn}(x)\varphi_n'(x)+c_{mn}(x)\varphi_n(x)=0,\quad a<x<b,\quad m=-1,0,1,..\ , \quad \text{(B.13)}$$

where the coefficients a_{mn}, b_{mn}, c_{mn} of the coupled-mode system are defined in terms of the vertical modes $Z_n(z;\mathbf{x})$. The coefficients are dependent on $\mathbf{x}$ through $h(\mathbf{x})$ and the corresponding expressions can be found in the following table :

	CASE I $m=-1$ $n=-1,0,1,2,\ldots$	**CASE II** $m=0,1,2,\ldots$ $n=-1$	**CASE III** $m=0,1,2,\ldots$ $n=0,1,2,\ldots$
$a_{mn}(x)$	$\langle Z_{-1}, Z_n \rangle$	$\langle Z_m, Z_{-1} \rangle$	$\delta_{nm} \|Z_m\|^2$
$b_{mn}(x)$	$2\langle Z_{-1}, \partial Z_n/\partial x \rangle$	$2\langle Z_m, \partial Z_{-1}/\partial x \rangle$	$2\langle Z_m, \partial Z_n/\partial x \rangle +$ $+h'(x)Z_m(-h)Z_n(-h)$
$c_{mn}(x)$	$\langle Z_{-1}, \Delta Z_n \rangle$	$\langle Z_m, \Delta Z_{-1} \rangle +$ $+\left(1+h'(x)\frac{\partial Z_{-1}(-h)}{\partial x}\right)Z_m(-h)$	$\langle Z_m, \Delta Z_n \rangle +$ $+h'(x)Z_m(-h)\left(\partial Z_n(-h)/\partial x\right)$
NOTES:	$Z_n = Z_n(z;x)$ is parametrically dependent on x through $h(x)$.		
	$\Delta\,\cdot = \frac{\partial^2 \cdot}{\partial z^2} + \frac{\partial^2 \cdot}{\partial x^2}$, $\langle f, g \rangle = \int_{-h(x)}^{0} f(z)g(z)dz$, $\|f\|^2 = \langle f, f \rangle$. For n=0,1,... $\Delta Z_n = \frac{\partial^2 Z_n}{\partial x^2} - (k_n)^2 Z_n$.		

The above coupled-mode system in $a < x < b$, is supplemented by the boundary conditions

$$\varphi_{-1}(a) = \varphi'_{-1}(a) = 0, \quad \varphi_{-1}(b) = \varphi'_{-1}(b) = 0, \tag{B.14}$$

$$\varphi_0(a) + ik_0^{(1)}\varphi_0(a) = 2ik_0^{(1)}A_0 \exp\left(ik_0^{(1)}a\right), \quad \varphi'_n(a) - k_n^{(1)}\varphi_n(a) = 0, \; n = 1,2,.. \;, \tag{B.15}$$

$$\varphi'_0(b) - ik_0^{(3)}\varphi_0(b) = 0, \qquad \varphi'_n(b) + k_n^{(3)}\varphi_n(b) = 0, \qquad n = 1,2,3,\ldots \quad . \tag{B.16}$$

The coefficients $A_R, C_n^{(1)}, A_T, C_n^{(3)}$ are then obtained by the equations:

$$A_R = \left(\varphi_0(a) - A_0 \exp\left(ik_0^{(1)}a\right)\right)\exp\left(ik_0^{(1)}a\right), \quad C_n^{(1)} = \varphi_n(a), \qquad n = 1,2,3,\ldots \tag{B.17}$$

$$A_T = \varphi_0(b)\exp\left(-ik_0^{(3)}b\right), \qquad C_n^{(3)} = \varphi_n(b), \quad n = 1,2,3,\ldots . \tag{B.18}$$

Solving the system and substituting the solution in the above equations, is easy to receive the coefficients for the semi-infinite strips, concluding for the wave field representation outside of the variable bottom topography. The system is supplemented by appropriate boundary conditions specifying the incident waves and treating reflection, transmission and radiation of

waves. It is worth mentioning here that if only the propagating mode (n=0) is retained in the expansion (11) the above CMS reduces to an one-equation model which is exactly the modified mild-slope equation derived by Massel (1993) and Chamberlain & Porter (1995). The obtained coupled-mode system of horizontal equations, being fully equivalent to any other complete linear model, presents a number of advantages as:

- Only a few modes are sufficient to accurately calculate the wave field in the whole liquid domain. Thus, this method effectively treats the nonlocal character of the problem in the propagation space, identifying and retaining the most important couplings.

- The enhanced coupled-mode system can be naturally simplified either to the extended mild-slope equation or to the modified one in subareas where the physical conditions permit it.

- The present method provides high-quality information concerning the pressure and the tangential velocity at the bottom, which is useful for the study of oscillating bottom boundary layer and wave-energy dissipation, as well as for sea-bed movement and sediment transport studies.

- Because of the completeness of the representation of the velocity field, it can be utilised for the construction and the efficient numerical treatment of the corresponding Green's function, which is the main tool for studying wave-body interaction problems in variable bathymetry regions.

Numerical results

For simplicity we consider here the case of a smooth underwater shoaling modeling a nearshore/coastal regions with different depths. This topography was also considered by Massel (1993) in order to demonstrate the effects of bottom slope and curvature on the solution obtained by his modified mild-slope equation. The particular environment is characterised by the following depth function

$$h(x) = h_m(x) = \begin{cases} h_1 = 5\text{m}, x < a = -20, \\ \dfrac{h_1 + h_3}{2} - \dfrac{h_1 - h_3}{2} \tanh(0.05x), a < x < b, \\ h_3 = 2\text{m}, x > b = 20\text{m}, \end{cases} \qquad (6.7)$$

which models a smooth but steep underwater step where the depth varies gradually from 5m to 2m. The maximum slope of the above bottom profile is $s_{\max} = 0.24$ and the mean slope $s_{\text{mean}} = 0.08$. (A sketch of the bottom geometry is shown in the figures below). We first consider a longer wave propagating from deeper to shallower water of angular frequency $\omega = 1.54 rad/s$ $(T = 4s)$, implying that both ratios $h_1/\lambda_1 = 0.22$ and $h_3/\lambda_3 = 0.12$ fall well outside the limits of the deep or the shallow water theory. Results are plotted in Figs. B.2,B.3,B.4,B.5.

A second example in the same environment is presented in Figs. B.6,B.7,B.8,B.9 and concerns shorter waves of angular frequency $\omega = 3.14 rad/s$ $(T = 2s)$, also implying that both ratios $h_1/\lambda_1 = 0.8$ practically corresponding to deep water conditions, and $h_3/\lambda_3 = 0.33$ which corresponds to intermediate depth to deep water.

In these figures the equipotential lines of the wave field (real and imaginary part) in the variable bathymetry subdomain are plotted, together with the calculated free-surface elevation. The results have been obtained by retaining 5 totally modes which is enough for numerical convergence. The patterns shown are quite reasonable and the equipotential lines intersect the bottom profile perpendicularly, as they ought.

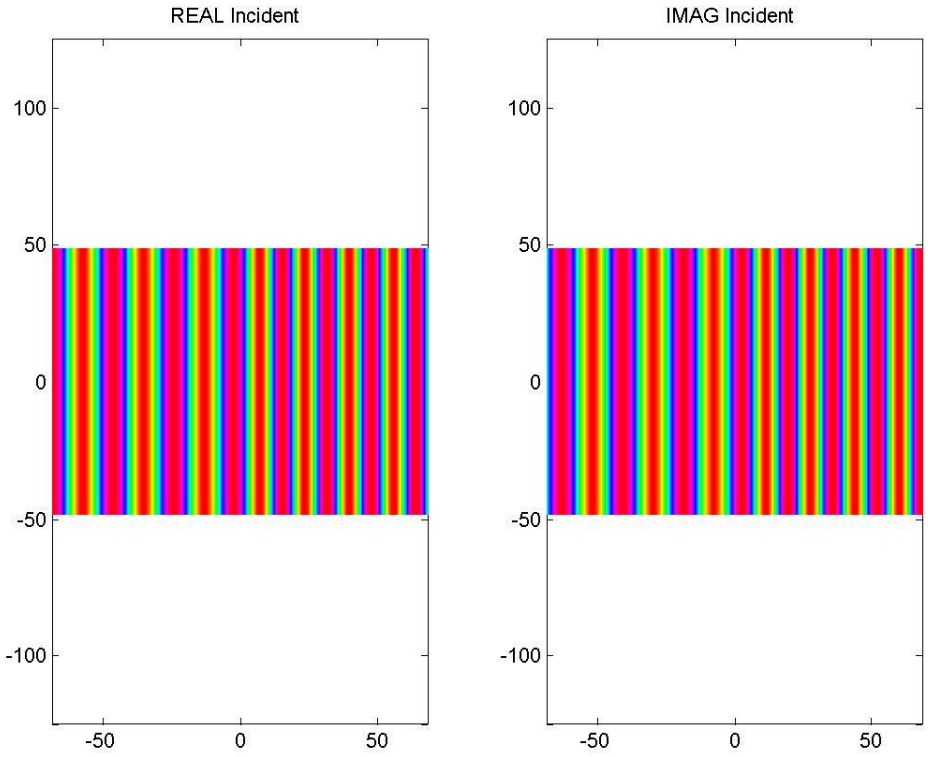

Figure B.2: Incident waves of period T=4sec propagating normally (θ=0deg) to the smooth shoal. Real (left subplot) and imaginary (right subplot) part of the wave potential on the horizontal plane.

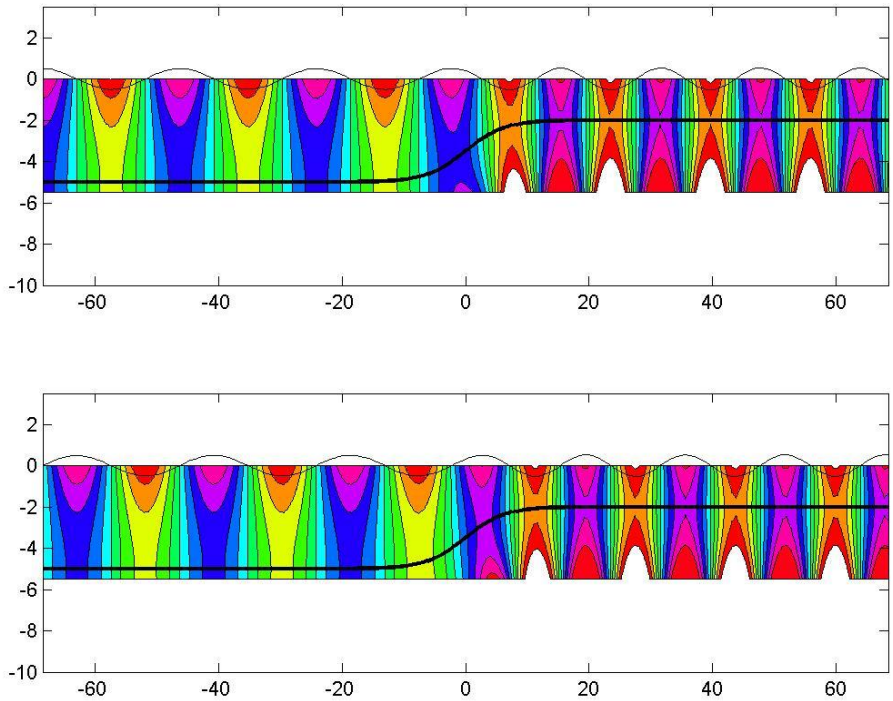

Figure B.3: Incident waves of period *T*=4sec propagating normally (θ=0deg) to the smooth shoal. Real (upper subplot) and imaginary (lower subplot) part of the wave potential on the the vertical plane

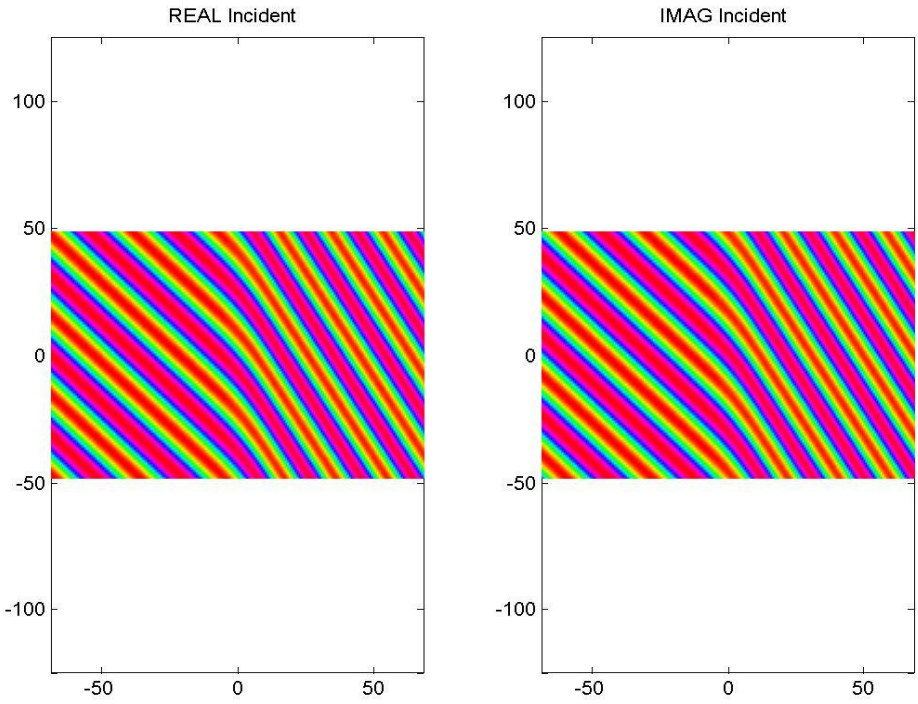

Figure B.4: Incident waves of period T=4sec propagating normally (θ=45deg) to the smooth shoal. Real (left subplot) and imaginary (right subplot) part of the wave potential on the horizontal plane.

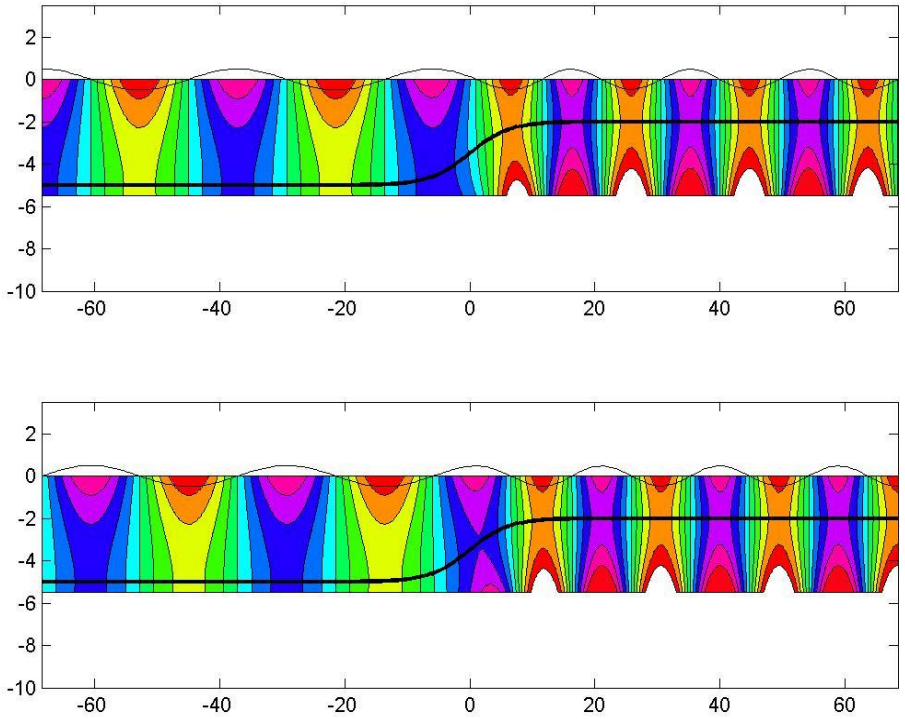

Figure B.5: Incident waves of period T=4sec propagating normally (θ=45deg) to the smooth shoal. Real (left subplot) and imaginary (right subplot) part of the wave potential on the vertical plane

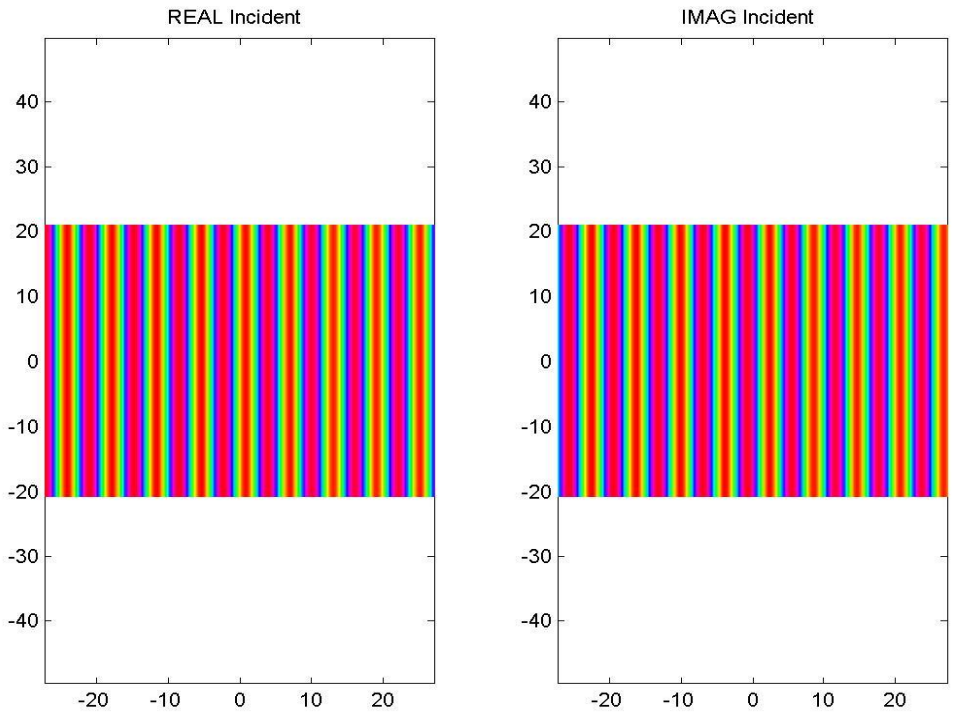

Figure B.6: Incident waves of period T=2sec propagating normally (θ=0deg) to the smooth shoal. Real (left subplot) and imaginary (right subplot) part of the wave potential on the horizontal plane.

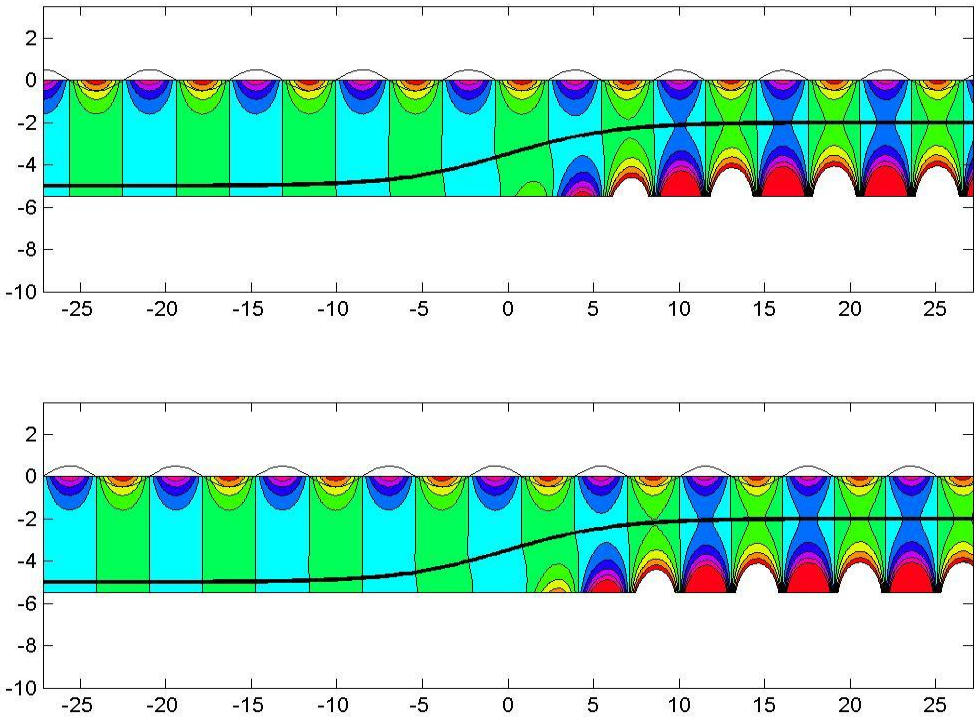

Figure B.7: Incident waves of period T=2sec propagating normally (θ=0deg) to the smooth shoal. Real (left subplot) and imaginary (right subplot) part of the wave potential on the vertical plane.

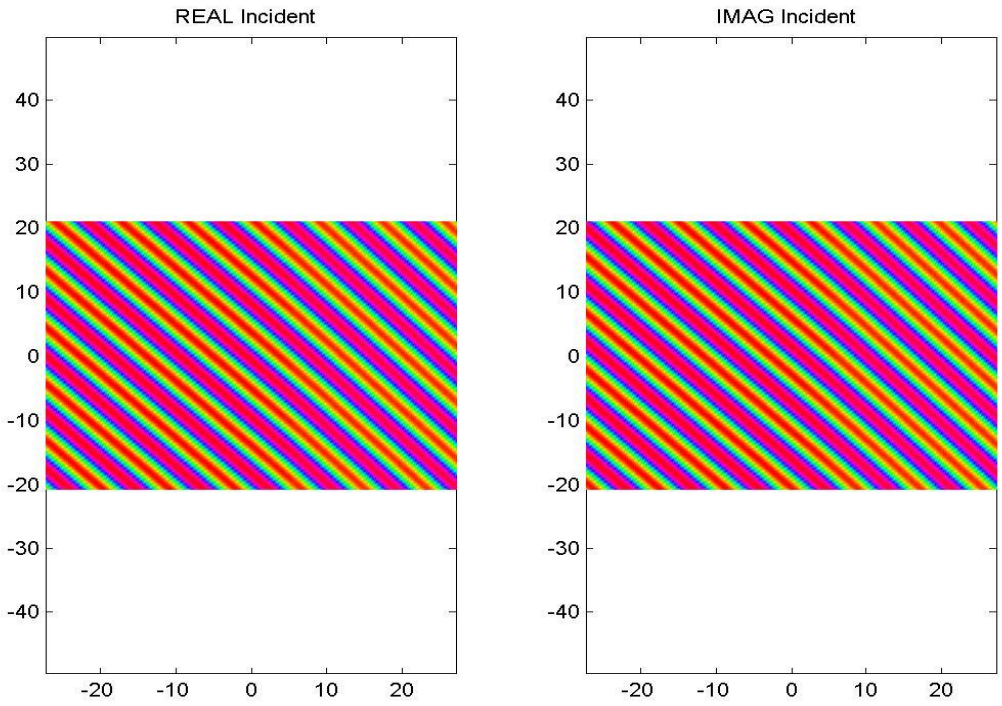

Figure B.8: Incident waves of period T=2sec propagating normally (θ=45deg) to the smooth shoal. Real (left subplot) and imaginary (right subplot) part of the wave potential on the horizontal plane.

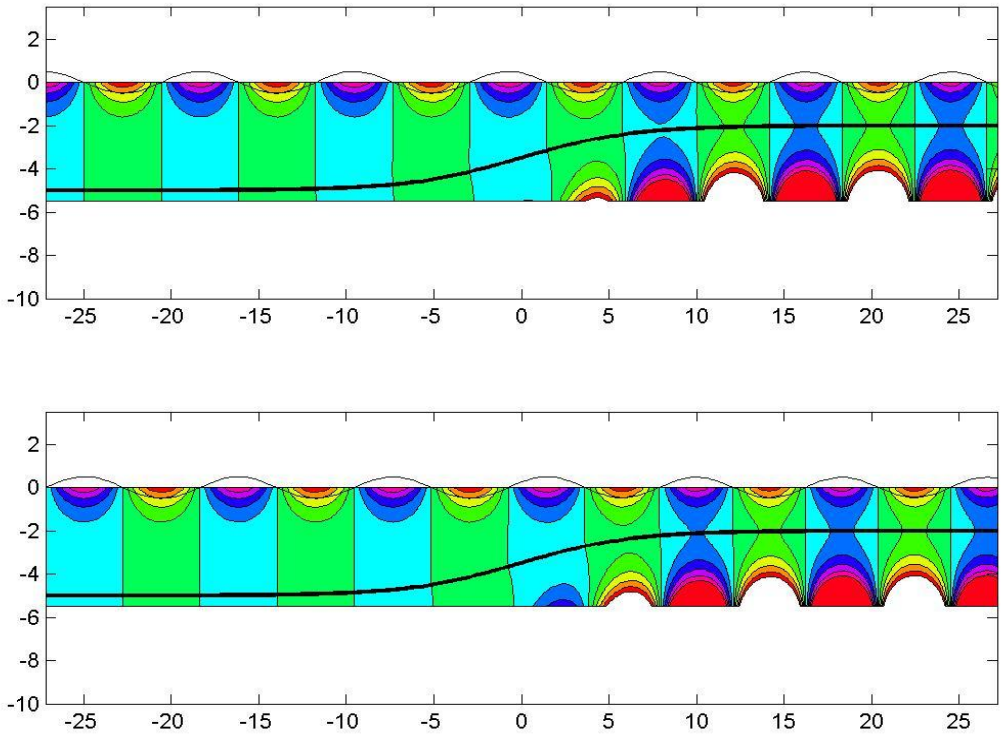

Figure B.9: Incident waves of period T=2sec propagating normally (θ=45deg) to the smooth shoal. Real (left subplot) and imaginary (right subplot) part of the wave potential on the vertical plane.